Studies on the Influence of Magnetic Cloud, Stream Interface and Polar Mesospheric Summer Echoes in the Mesosphere and Lower Thermosphere (MLT) region using model calculations and observations

by

Olakunle Ogunjobi

Submitted in fulfillment of the requirements for the degree of Doctor of Philosophy in the School of Chemistry and Physics, University of KwaZulu-Natal, Durban.

August 2014.

As the candidate's Supervisor I have/have not approved this thesis for submission.

Signed: ..... Name: ..... Date: .....

Abstract

The response of Mesosphere and Lower Thermosphere (MLT) temperature to energetic particle precipitation over the Earth's polar regions is not uniform due to complex phenomena within the MLT environment. Nevertheless, the modification of MLT temperatures may require an event based study to be better observed. Three Geospace events examined in this study are: Magnetic Clouds (MC), solar wind Stream Interfaces (SI) and Polar Mesospheric Summer Echoes (PMSE).

The MC is a transient ejection in the solar wind defined as the region between the preceding half of the z– component of southward interplanetary magnetic field (IMF–Bz) and the trailing half, which contained strong northward peak or vice versa, with an accompanied large density enhancement that strongly compressed the magnetosphere. The varied instrumentation which is located not only in South African National Antarctic Expedition (SANAE) IV, but also at Halley, a same radial distance ($L \sim 4$) location in the Southern hemisphere, and at the vicinity of conjugate location in Northern hemisphere provide an opportunity to test the theories applied to high latitude heating rates on arrival of MC. The Halley riometer is used to monitor coincidences of absorption with arrival of a fortuitous MC that was observed on 8 November 2004. Using Monte Carlo Energy Transport Model (MCETM), the corresponding altitude of electron and proton energy distribution indicates the importance of MC triggered geomagnetic storms on mesospheric dynamics.

At the arrival of SI near the Earth's bow nose, compressional streams propagate into the inner magnetosphere, where they fueled magnetospheric storms. A number of SI events were obtained close in time to the pass of temperature retrieval onboard the Thermosphere Ionosphere Mesosphere Energetic and Dynamics/Sounding of the Atmosphere using Broadband Emission Radiometry (TIMED/SABER) over SANAE IV. The relationship between the ionospheric absorption measured by riometer and the layer of energetic particle precipitation from National Oceanic and Atmospheric Administration/Polar Orbiting Environmental Satellites (NOAA/POES) was examined during these events. Here, a superposed

epoch technique is described and implemented to obtain average temperature profiles during SI–triggered particle precipitation. Prior to SI onset, there is no significant temperature decrease below 100 km, whereas at the onset of the SI–triggered precipitation, we observe an immediate superposed average temperature decrease of about 35 K around 95 km. Results indicate that, cooling effects due to the production of mesospheric odd hydrogen might be major contributors to temperature decrease under compressed solar wind stream.

PMSE, as a one–type Geospace event, exists because the electrically charged–ice particles reduce the mobility of mesospheric free electrons. In this study, first long term observations of PMSE, with Super Dual Auroral Radar Network (SuperDARN) SANAE IV HF radar (hereafter in this thesis referred as SuperDARN–PMSE), is presented. An extraction algorithm is described and implemented to obtain SuperDARN–PMSE during the summer period of years from 1998 to 2007. We examined the SuperDARN–PMSE occurrence rate in relation to geomagnetic activity and flow of mesospheric winds. Furthermore, the temperature changes in relation to SuperDARN–PMSE has been studied. The SuperDARN–PMSE peaks coincide with lower summer mesopause temperature and higher geomagnetic activity. Analysis of neutral wind variations, in relation to SuperDARN–PMSE peaks, indicates the importance of pole to pole mesospheric transport circulations.

In addition, the mid–latitudes thermospheric zonal winds variations from the year 2005 to 2008 and its relevance to magnetospheric activity are examined. These studies could be directed towards achieving a more self–consistent interpretation of how the MLT energy budget is affected by magnetospheric processes.

PREFACE

The experimental work presented in this dissertation was carried out in the School of Chemistry and Physics, University of KwaZulu–Natal, Westville Campus from November 2011 to August 2014, under the supervision of Professor Sivakumar Venkataraman.

These studies represent original work by the author and have not otherwise been submitted in any form for any degree or diploma to any tertiary institution. Where use has been made of the work of others it is duly acknowledged in the text.

DECLARATION 1 - PLAGIARISM

I, ..., declare that

1. The research reported in this thesis, except where otherwise indicated, is my original research.
2. This thesis has not been submitted for any degree or examination at any other university.
3. This thesis does not contain other persons' data, pictures, graphs or other information, unless specifically acknowledged as being sourced from other persons.
4. This thesis does not contain other persons' writing, unless specifically acknowledged as being sourced from other researchers. Where other written sources have been quoted, then:
   (a) Their words have been re–written but the general information attributed to them has been referenced
   (b) Where their exact words have been used, then their writing has been placed in italics and inside quotation marks, and referenced.
5. This thesis does not contain text, graphics or tables copied and pasted from the internet, unless specifically acknowledged, and the source being detailed in the thesis and in the references sections.

Signed: .....

DECLARATION 2 - PUBLICATIONS

Details of contribution to publications that form part and/or include research presented in this thesis (include publications in preparation, submitted, in press and published and give details of the contributions of each author to the experimental work and writing of each publication)

The following contribution to publications form the basis of this thesis:

1. Ogunjobi, O., Sivakumar, V., Mbatha, N., 2014a. A case study of energy deposition and absorption by magnetic cloud electrons and protons over the high latitude stations: effects on the mesosphere and lower thermosphere. *Terrestrial, Atmospheric and Oceanic Sciences* 25, 219-232, doi: 10.3319/TAO.2013.10.14.01(AA).

2. Ogunjobi, O., Sivakumar, V., Sivla, W.T., 2014b. A superposed epoch study of the effects of solar wind stream interface events on the upper mesospheric and lower thermospheric temperature. *Advances in Space Research*, in press, doi: 10.1016/j.asr.2014.07.005.

3. Ogunjobi, O., Sivakumar, V., Stephenson, J. A. E., 2014c. Long term observations of polar mesosphere summer echoes observed by SuperDARN SANAE HF radar in Antarctica. *Advances in Space Research*, in review (Journal Ref. ASR–D–14–00464).

4. Ogunjobi, O., Sivla, W. T., Sivakumar, V., 2014d. The mid–latitude upper thermospheric zonal winds variation during the recent solar minimum. *To be submitted for publication.*

Contributions were also made to other publication and conference proceedings:

- Sivla, W. T., Ogunjobi, O., 2013. Zonal winds in the west african region upper thermosphere during low solar activity period. *Peer reviewed conference proceedings, South African Society for Atmospheric Sciences (SASAS), 29th annual Conference, 26–27th September 2013, Durban*, page 162-165.

- Sivla, W. T., Ogunjobi, O., 2013. The mid–latitudes upper thermosphere during the recent solar minimum. *Peer reviewed conference proceedings, South African Society for Atmospheric Sciences (SASAS), 29th annual Conference, 26–27th September 2013, Durban*, page 125–127.

- Sivla, W. T., Ogunjobi, O., Ochala, I., 2013. Thermosphere wind variation during magnetically quite period. *Advances in Applied Science Research*, 4, 169-175.

Signed: .....

Acknowledgement

I am thankful to a few people who have made this work both possible and interesting: my supervisor, Professor Sivakumar Venkataraman, for his guidance, stimulation and support throughout this study and especially for his very encouraging remarks; Dr Nkanyiso Mbatha for his enthusiastic patronage; Dr Judy Stephenson for her helpful advice and scientific suggestions; the various providers of data for their indispensable data produced and generous practical support; Professor Micheal Kosch for a bit of highly informative discussions on one of the chapters; Dr Sivla Tafon who have motivated me to twenty first century; my parents for their faith in me; Bunmi and 'Koremola for their forbearance, tolerance, stimulation and being the best caching partners; and, finally, to the folks down the corridor, Patrick Itegbeyogene and Zolile Mthumela for being great company.

Chapter 1

Introduction and background theory

The primary focus of this study is to examine possible temperature changes in the Mesosphere (50–100 km) and lower thermosphere (100–180 km) (MLT) region during some specific Geospace events. A great number of variables are involved within the MLT energy balance. Solar radiation, particle precipitation due to geomagnetic storms, tropospheric waves, turbulence, winds, chemical reactions, Joule heating, infrared cooling, photo electrons and heat conduction altogether participate significantly in heating (increase in temperature) and cooling (decrease in temperature) processes. It is as a consequence of this complication that estimating and evaluating the MLT temperature changes is an exigent scientific challenge.

The Mesosphere and Lower–Thermosphere call attention to the need to consider both of the two regions simultaneously, if one desires to obtain a perfect and consistent overview of the energy budget at these heights. The region of the MLT is however, affected in a number of ways. During geomagnetic storms, driven by Geospace events, the atmosphere can experience an increase in energy inputs from particle precipitation. The precipitating particle can affect the atmospheric conformation via excitation, dissociation and ionisation. The atmospheric compositional changes will, in turn, induce infrared cooling rates and/or chemical heating rates, depending on the specific Geospace event that triggered the precipitation. While some of the Geospace events trigger energetic particles of magnetospheric origin and, thus, affect the MLT composition, others may need atmospheric features such as turbulence, gravity

waves and tides to cause any effect. In view of this, it is critical to consider the MLT temperature variations in relation to natural activities. This will help to differentiate them from the perturbations induced by global changes. Since natural activities are not of the same origin, it is more important to discern between the various Geospace events influencing the MLT dynamics. In other words, the MLT effect caused by specific Geospace events can be examined on an individual basis. As noted earlier, some of the specific Geospace phenomena, upon which attention is focused, are Magnetic Cloud (MC), solar wind Stream Interfaces (SI) and Polar Mesosphere Summer Echoes (PMSE).

In addition to the new input of this work to the MLT temperature research, the use of both ionospheric and atmospheric measurements has been included. Traditionally, magnetospheric–ionospheric and lower atmospheric science communities have been somewhat detached, showing different interests in studies of Geospace events. This sort of disconnection is, of course, hollow because the neutral atmosphere and magnetosphere are not separate domains. For this work, using a MCETM, it is natural to assume vantage of both magnetospheric–ionospheric and neutral atmospheric observations, since it permits scope for a thorough understanding of the concatenation of activities emerging from the magnetospheric particle–induced ionisation to MLT temperature modifications.

Different topics presented in this study are, largely, dependent on the availability of the data thus, some of the specific subjects are outlined at the beginning of each chapter. This thesis consists of prelusive parts and the latter parts of the thesis are devoted to the data analysis and results obtained within the context of this study. The remainder of this introduction provides a brief description of how the Sun and Earth environments are coupled through radiative, dynamic and magnetic processes. Between the Sun and the Earth is the neighbourhood, defined as interplanetary space. Contrary to popular belief, this space is not a vacuity, but instead is populated by a low density, variable medium. This medium, and the manner through which the sun influences it, affects the entire system of the Earth. The aim of the subsequent sections is to summarise the regions of the solar–terrestrial environment,

dwelling especially on the basic concepts of solar and magnetospheric physics, in order to provide background knowledge in the settings of this work. It also includes the discourse on the Sun's interaction with the Earth, via specific Geospace events and how these events drive different phenomena on Earth.

1.1 The Sun

The Sun emits electromagnetic radiation and matter consisting, mainly, of protons and electrons, as a consequence of the nuclear fusion process within its interior (Rees, 1964). The emission is accompanied by a small percentage of alpha particles and some heavier nuclei into interplanetary space. The solar activities reflect the unevenness of the Sun's processes. For instance, the daily solar activity is estimated by counting the number of individual and groups of spots on the Sun's surface, which are known as Sunspots. A good illustration of Sunspots is depicted in Figure 1.1. Sunspots are dark areas along the airfoil of the Sun, which represent large concentrations of intense magnetic flux associated with UltraViolet (UV) radiation. The existence of sunspots has been recognised since around the Fourth Century B.C. They can be as big as 20 Mm in diameter, each consisting of a central dark umbra at a temperature of 4100 K and a field strength up to 1 T (Jursa, 1985). The number of sunspots vary, with a 27 day corotation or with an 11 year frequency. Even so, the cycle amplitude varies and there have been periods of low Sunspot number. There are great numbers of Sunspots during solar maximum and fewer Sunspots during solar minimum. Due to Sun spot variation, several solar activities have come forward, providing more insight into interplanetary space. Some of these activities include solar flares, as seen in Figure 1.1, Corona Mass Ejections (CME) and Corotating Interaction Regions (CIR), which will be discussed, subsequently.

1.2 The Solar wind

Interplanetary space is filled with flowing plasma known as the outer solar atmosphere, expanding radially through the solar system. The solar wind, depicted in Figure 1.1, is predominantly comprised of protons and electrons that are energetic enough to escape the solar gravity. At one astronomical unit (AU), these energetic particles can have velocities in the range of 300 to 700 km/s. Although, during periods of extreme solar activity, the solar wind can be as high as 1000 km/s (Jursa, 1985; Kivelson and Russell, 1995). Typical particle densities as measured at the Sun–Earth distance show protons at 6.6 cm^{-3} and electrons at 7.1 cm^{-3}, although the solar wind is extremely dynamic, with large variations in both flow speed and density (Kivelson and Russell, 1995; Pudovkin, 1996). Phenomena occurring at the Sun, as noted earlier, can dramatically affect the solar wind parameters. For example, coronal holes are regions where fast solar plasmas stream out into interplanetary space at high velocities, creating regions in the solar wind, known as High Speed Solar Wind Streams (HSSWS) (e.g, Jursa, 1985; Denton et al., 2009).

The HSSWS is created by the Coronal holes of large size, nearby the Sun–Earth connection line. The interaction of the HSSWS with the slower stream in interplanetary space forms CIR (e.g, Jursa, 1985; Tsurutani and Lakhina, 1997; Borovsky and Denton, 2006; Denton et al., 2009). Measurements downstream often show an increase streaming of precipitous solar wind speed as it co–rotates with the Sun, mostly during the minimum solar activity. This is because Coronal activities vary in durability and are more active at the sunspot minimum, every 11 years. At the minimum activity, the corona becomes flattened in shape by the solar magnetic field, due to its streamer composition. Nonetheless, the solar wind speed has a bimodal structure, that is, it has two basic flow type: HSSW and Slow Solar Wind Streams (SSWs). High Speed Solar Wind Streams (HSSWS), as fast streams, recurs with the Sun's equatorial rotation period, characterised by density enhancements at their leading edge with a velocity of over 500 km/s (Denton et al., 2009). Whereas, SSWs emanates, perhaps, from the vicinity of the streamer belt with a velocity of approximately 300 km/s.

Another demonstration of influence of the Sun's activity on interplanetary space are solar flares (see Figure 1.1) as noted earlier. These are explosions from the sun that occur when magnetic energy is suddenly discharged, resulting in the forcing out of very energetic charged particles (Bothmer and Schwenn, 1995). Flares occasionally occur with CME (an explosive expulsion of a large amount of solar matter from the solar atmosphere into interplanetary space which often characterise the period of solar maximum activities (Borovsky and Denton, 2006)). The CME are vast clouds of plasma (∼1013 kg) that split out from the sun and expand at speeds as high as 2000 km/s. When attendant CME collides with the Earth, they often excite geomagnetic storms, as do the CIR, which will be discussed later.

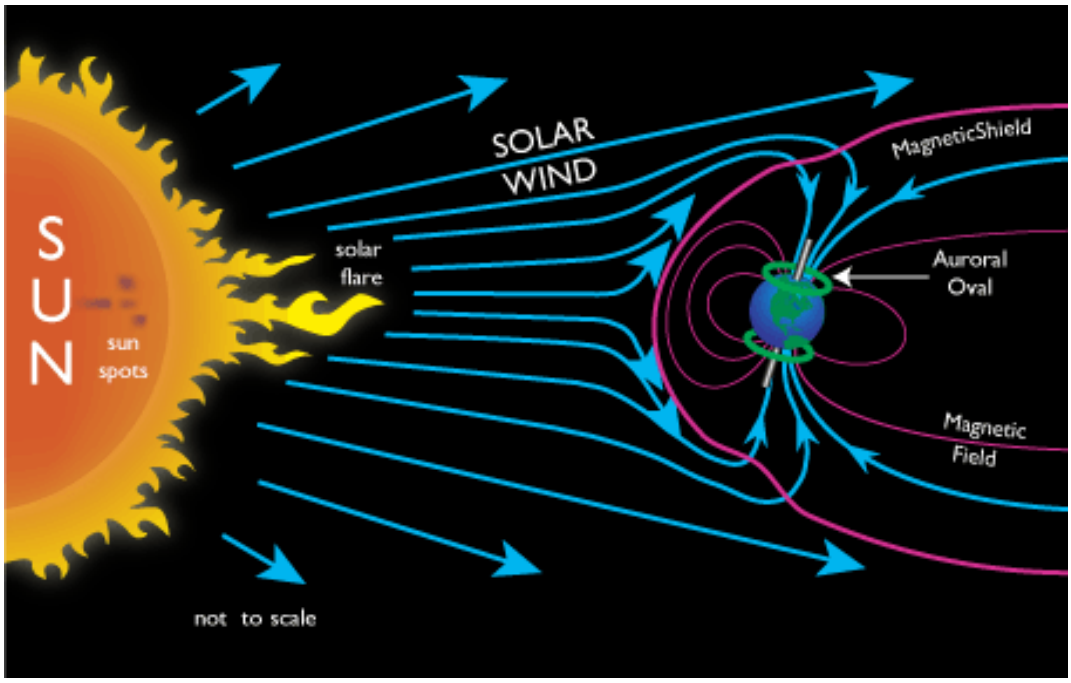

Figure 1.1: An artistic impression of how the Sun's solar wind spirals towards the Earth's lines. Figure adopted from TheWathchers (2013).

1.3 The interplanetary magnetic field

An elongation of the solar magnetic field that is frozen in the solar wind is known as the Interplanetary Magnetic Field (IMF) (Dungey, 1961). Since the IMF is embedded in the plasma of solar wind, a parcel of plasma will drag the field lines radially away from the sun.

The source region of the field line rotates with the Sun, resulting in a spiral effect in the IMF known as the Parker Spiral (Jursa, 1985). The Parker Spiral is an idealised case. In reality, the magnetic field of the sun is extremely complex. The spiralling action can either be in Archimedean (arithmetic) spiral or logarithmic spiral, as shown in Figure 1.2. Nonetheless, the Parker Spiral case, generally, serves as a good estimate of solar wind energies emanating from the Sun's activity. The IMF varies, significantly, over the path of a solar cycle. At sunspot/solar minimum, the field is ordered with a disc–like current sheet separating the inward and outward orientated magnetic field lines, as shown in Figure 1.3. In contrast, towards solar maximum, the current sheet becomes curly with a disordered magnetic field, resulting in a blustery solar wind. On average, this happens every 11 years. Ideally, a cycle lasts for a period of 22 years, as a result of the changing orientation of the IMF over each 11 year cycle. Notwithstanding, most solar wind particles are deflected past planet Earth, but a few can gain access into the Earth's magnetosphere, where they become trapped by Earth's magnetic field (left side of Figure 1.1). The various phenomena, such as magnetic shield, auroral oval and Earth's magnetic field will be expanded and discussed in following sections.

1.4 The magnetosphere

The term magnetosphere identifies near–Earth space, that is enclosed within the Earth's magnetic field. This subsection describes general topology of this field, including descriptions of some of the distinct regions (Earth's radiation belt and the plasmasphere) that make up the magnetosphere. The magnetosphere, generally, describes the Earth's space environments. The description is, mainly, based on the behaviour and number of charged particles, as shown in Figure 1.4.

In tracing the interactions along the solar wind emanating from the Sun and the Earth's magnetosphere, two coordinate systems are used. These systems are: geocentric solar magnetospheric (GSM) coordinates and geocentric solar-ecliptic (GSE) coordinates (Kivelson

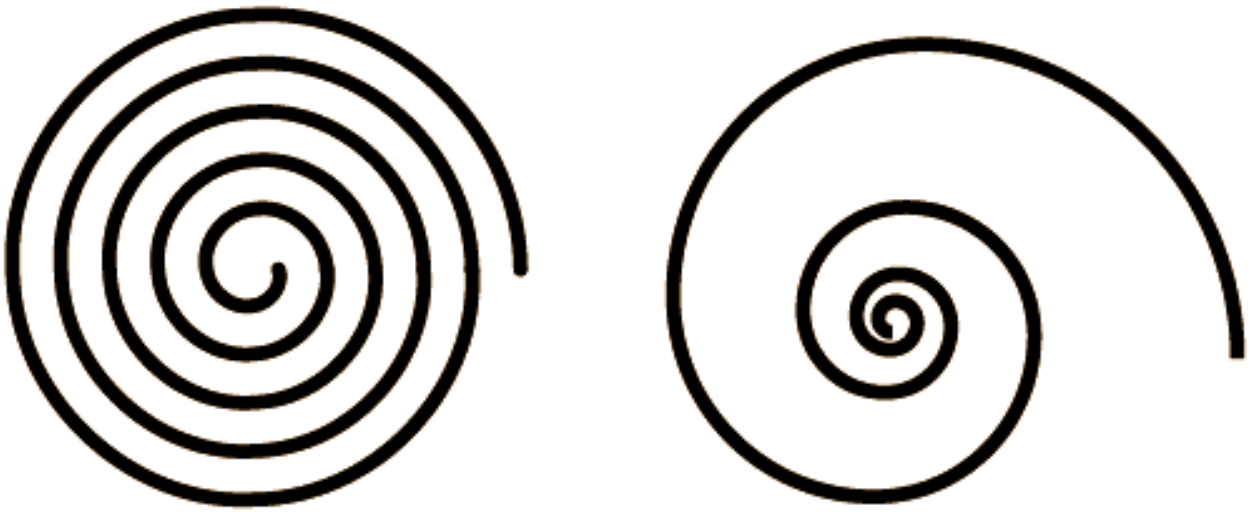

Figure 1.2: A schematic illustration of Archimedean spiral (left) and logarithmic spiral (right). Figure adopted from Kivelson and Russell (1995).

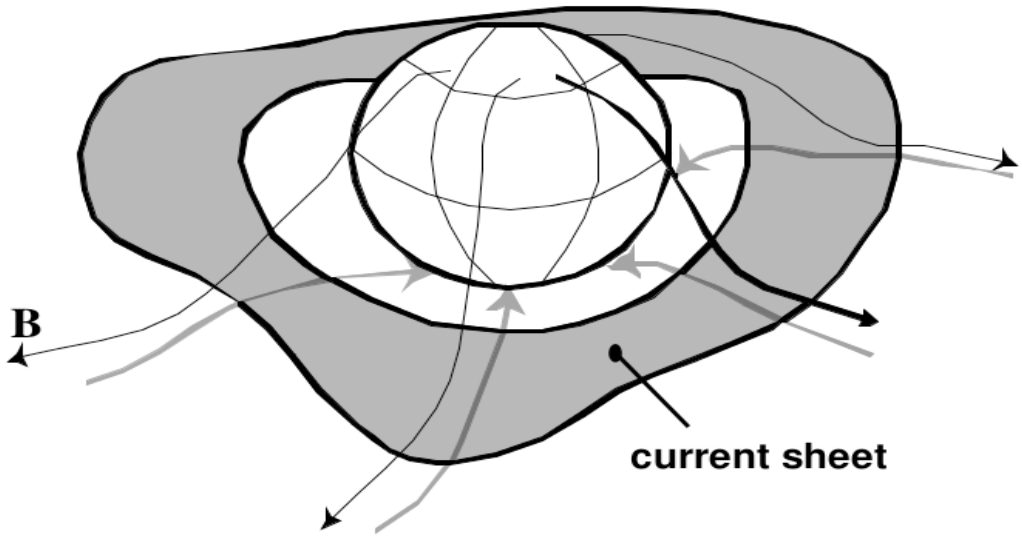

Figure 1.3: Ballerina Skirt model of IMF with current sheet separating the oppositely orientated field, B. Figure obtained from Andrew (2002).

.

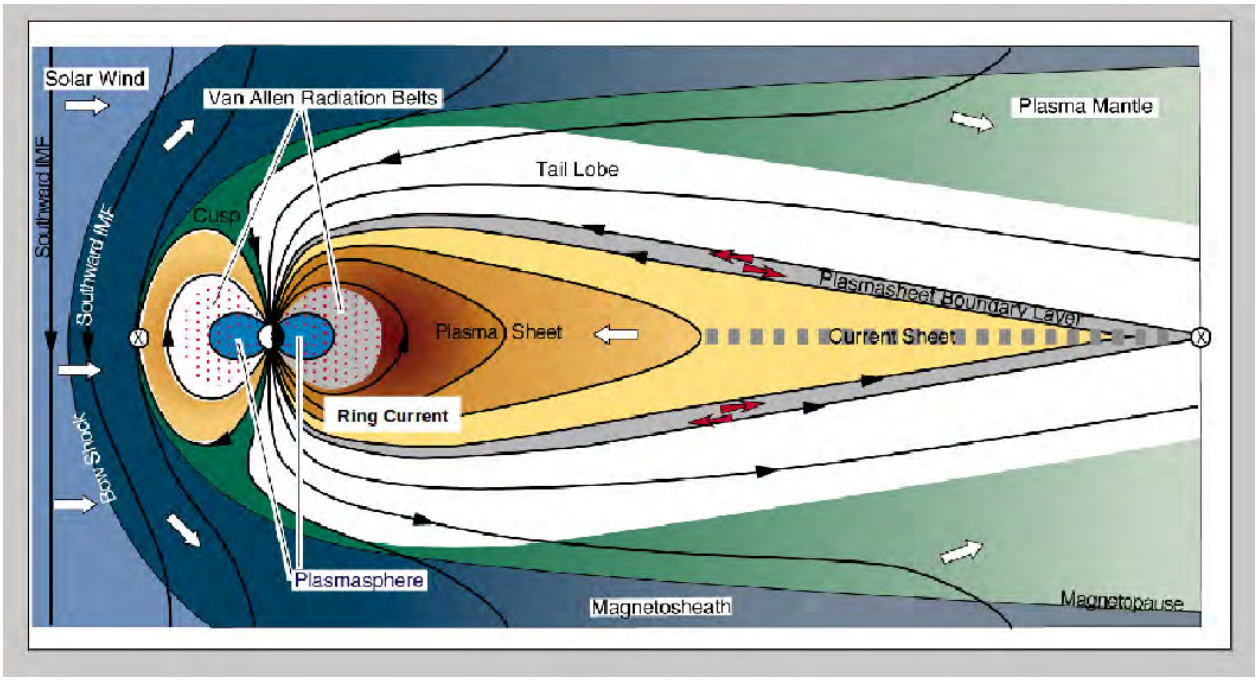

Figure 1.4: An illustration of the Solar wind and magnetosphere interactions. Figure adopted from Hill and Dessler (1991).

and Russell, 1995). Both geophysical coordinate systems originate at the Earth's core, with the X-axis towards the Sun. For GSE coordinates, the Z–axis is normal to the ecliptic plane, while the Y completes the right hand system and is positive toward the dusk. In the GSM coordinate, the Z–axis is coplanar with the Earth's magnetic centre line and the X–axis, while Y is perpendicular to the magnetic dipole to the dusk side.

1.4.1 Magnetic field topology

The Earth has a magnetic field which is dipolar at small distances. The field is, possibly, generated from a dynamo process associated with the circulation of liquid metal in the Earth's core and the internal heat forcing (Kivelson and Russell, 1995). Nevertheless, the Earth's magnetic field constitutes a barrier to the solar wind, resulting in a magnetic cavity in the IMF. The condition of Earth's magnetosphere is, mainly, described by the malformation of the IMF and solar wind plasma. However, the Earth's magnetic field can be significantly disrupted by the impact of the solar wind emanating from the Sun. Rather than being a

simple dipole after impact, the Earth's magnetic field is squeezed by the solar wind flow on the position facing the Sun. The compressed magnetic field is then extended away on the opposite side, termed the magnetotail (see Figure 1.4), which extends for tens of Earth radii (R_E).

Dungey (1961) had earlier suggested that the IMF and magnetosphere could converge under certain conditions. Typically, this condition is expected to involve a strong southward IMF in the GSM component, leading to an open magnetosphere. During this process, the uppermost layer of the magnetosphere can strip off, a process which describes the phenomenon known as 'magnetopause shadowing'. Dungey's (1961) theory of magnetic reconnection explains the activity by which magnetic field lines diffuse across a current sheet and join with the antipodal aligned field. This coupled system involves conveyance of energetic particles in the solar wind into the magnetosphere. Reconnection on the dayside causes an increased magnetic flux near the pole, termed polar cap region. From this region, the field lines will trail back into space and, ultimately, will connect back to the IMF. In reality, the magnetospheres is, broadly, thought to be often open. Figure 1.5 depicts open and closed magnetosphere which arise from the effect of IMF BZ orientation. However, observations suggest that reconnection can occur in a steady–state form, as anticipated by Dungey (1961), but also in a pulsed manner. The freshly opened magnetic field lines convect past the polar cap, attaching to the flux of open field lines. Ultimately, these open field lines will, once again, join with the closed field in the tail.

Dipole magnetic field component

The Earth's magnetic field lines, to the lowest order, are often approximated using the L–value (dipole magnetic field coordinate) parameter (Roeder, 1970). Details of the procedure in obtaining L parameter are given in Appendix A. The Earth's magnetic field lines, passing over the equator at a specific number of R_E is equivalent to the L–value. Therefore, a field line at 4 R_E, from the Earth's core will be at $L \sim 4$. This parameter L is related to the invariant magnetic latitude by the expression:

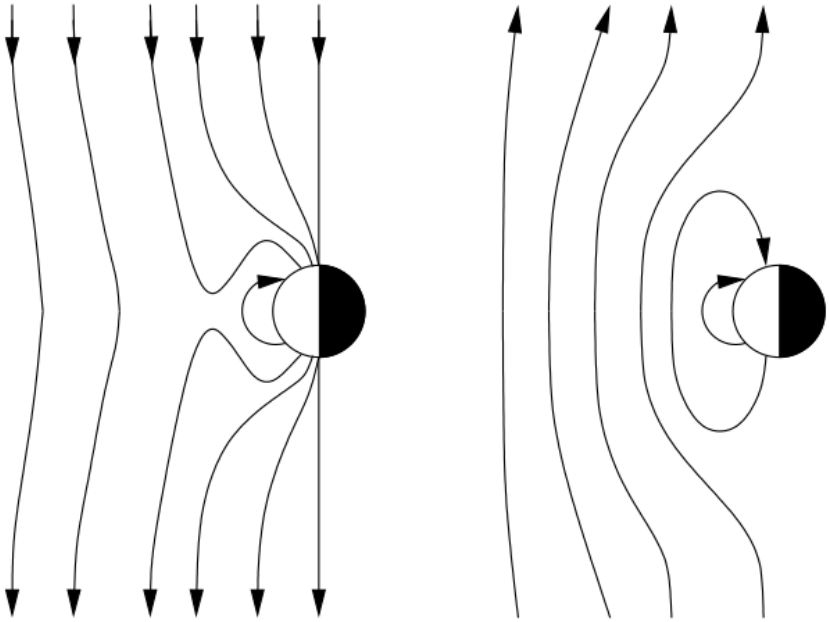

Figure 1.5: An illustration of open (left) and close (right) magnetospheres due to IMF Z–component (adopted from A. B. Collier, private communication, 2010).

$$\lambda = \cos^{-1}(\frac{1}{L})^{\frac{1}{2}} \tag{1.1}$$

Apart from using the L–value to formally define the Earth's true instantaneous magnetic field, it can also be used to understand magnetic phenomena near the Earth space environment. For instance, the spatial location of a satellite measurement at a specific period can be estimated by using the L–value parameter. The dipole model (i.e. L parameter) is a first order true estimation of the Earth's magnetic field in a complex state (Varotsou et al., 2008; Morley et al., 2010; Ogunjobi et al., 2014a). This complex condition can be attributed to the IMF effects and the solar wind at the Earth's magnetic sphere. Such complexity may result in inaccurate values at lower L.

1.4.2 Trapped radiation belt

Within the magnetosphere, there is a region of trapped energetic particles, known as the Van Allen belt or Radiation belt (Van Allen, 1959), herein, referred to as Earth's radiation belt.

The belt extends from a few hundred km above the Earth to about 7 R_E. The radiation belt prevents most of the charged particles carried by the solar wind from entering to the surface of Earth. Due to the forces from the magnetic field, as noted above, highly energetic particles become trapped within the Earth's radiation belt zone. Two regions that make up the belt are shown in Figure 1.6. For over 5 decades, it was broadly thought that the Earth's radiation belt comprised of the inner belt and outer belt separated by a region of low density called slot region (usually, between L ∼2.5 and L ∼3) as shown in Figure 1.6 (A). Depending on the Earth's magnetic field lines, the inner radiation belt was earlier thought to occupy between L ∼1.2 and L ∼2.5 away from the Earth's core with relatively stable proton populations. The evolution of the inner belt is due to the influence of losses due to 'Coulomb scattering '(see, Ganushkina et al., 2011) while the outer radiation belt was previously conceived to be within a space between L ∼3 and L ∼7 with highly dynamic electron populations. It was also thought that electrons carried by the solar wind, as well as the few electrons from the ionosphere, serve as sources of the outer radiation belt particles. Nonetheless, recent observations by Baker et al. (2013) show that the earlier acceptable two–region radiation belt may not, necessarily, be so. The recent in–situ and radiation belt probe spacecraft observations by Baker et al. (2013) revealed an isolated belt (within L ∼3.0 to L ∼3.5) separated by another slot region (Figure 1.6 B). This isolated toroidal region was found to comprise electron energy of over 2 MeV which remained for 4 weeks before it was predominantly annihilated by a strong interplanetary shock (consult Baker et al. (2013) for recent updates on radiation belts). Particles in the Earth's magnetosphere, or more exactly in the trapped belt can undergo three types of motions (gyration, bounce and drift motion) from interactions with the Earth's magnetic field. These types of motion are shown in Figure 1.7.

With reference to the Lorentz force (F)

$$\vec{F} = q(\vec{E} + \vec{V} \times \vec{B}),$$

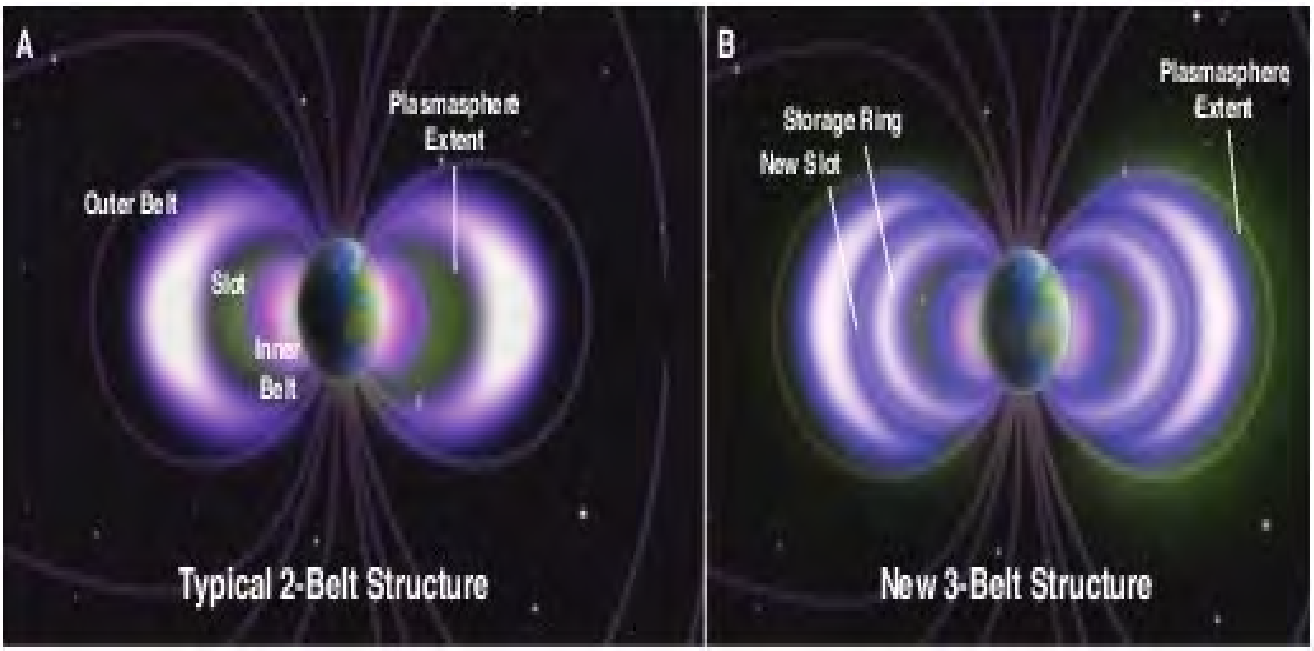

Figure 1.6: The Earth's radiation belts structure. (A) shows the outer belt and inner belt, and the usual plasmasphere location. (B) same as (A), but for a recent (year 2012) more extremely bloated plasmasphere and unanticipated third radiation belts. Figure obtained from Baker et al. (2013).

a charged particle (q) with a perpendicular component of velocity ($\vec{V}$) will gyrate around the magnetic field ($\vec{B}$) line due to the electric field ($\vec{E}$). This motion makes electrons spiral around the magnetic field lines. The second particle motion, bounce motion, is regulated by the gradient force

$$\vec{F} = -(\mu \nabla)\vec{B},$$

where μ is the magnetic moment. The first adiabatic invariant is the magnetic moment, which implies that the perpendicular energetic particle is proportional to the magnetic field intensity. In other words, as the particle travels into regions where the magnetic field is stronger, the perpendicular velocity increases. The velocity increase is more evident towards the pole. The increase in perpendicular velocity results in a diminution in the parallel velocity. This goes on until the gradient force bounces the particle back along the field line and proceeds towards the opposite pole. The point at which the particle is forced back along the field line is called the mirror point. The bounce motion associated with

the second adiabatic invariant, guides the energetic particles closer to the Earth's surface as they move north or south. This occurs based on the magnetic field line curvature. The third motion (third adiabatic invariant) that govern the radiation belt particles is the drift motion. In this situation, particles drift around the Earth's radiation belt slowly. This is due to both curvature and gradient of the magnetic field. A particle of this nature can remain trapped in the magnetosphere provided all the aforementioned adiabatic invariants (gyro, bounce and drift motions) are preserved. This can only be possible with slow changes in the Earth's magnetic field. Nevertheless, one or more of the invariants can be violated during geomagnetic storms which will be discussed later.

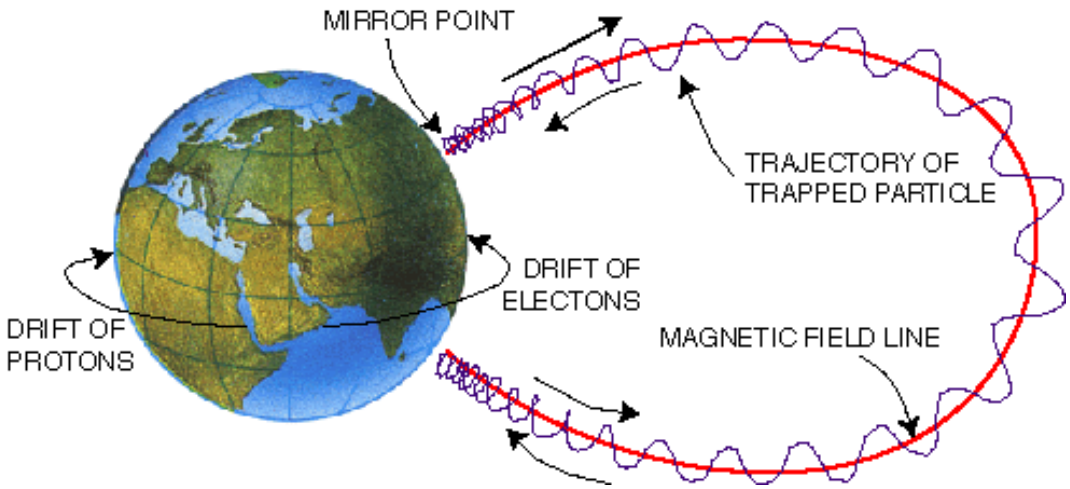

Figure 1.7: A simplified depiction of charged particle motion within the radiation belt, inluding the location of mirror point. Figure adopted from Baumjohann and Treumann (1996).

Apart from the trapped radiation belt region, the inner magnetosphere also consists of the plasmasphere region. Though these regions are sometimes collocated and draw two different energy regimes; the plasmasphere is cold, whereas, the Earth's radiation belts are composed of the most energetic particles in the magnetosphere. The plasmasphere is made of high densities ($\sim$10 m^{-3}) of cold ($\sim$ 1 eV) plasma (Olasen et al., 1987). The plasmasphere has an outer edge called the plasmapause where the dense, cold plasma is, usually terminated. Unlike the Earth's radiation belts, the innermost portion of the plasmasphere does not depend, strongly and systematically, on geomagnetic activity.

1.5 Geomagnetic storms

The Earth's magnetic field exhibits both regular daily variants and irregular disturbances, known as geomagnetic storms. The disturbances are prompted by the solar wind interacting with the Earth's magnetic field. These irregular magnetic disturbances can manifest different patterns in their occurrence frequency. The major pattern is often correlated with certain irregular magnetic storms. These magnetic storms are, commonly, characterised by the sporadic CME events and the 27–day CIR events. Major effects of these storms occur in the high latitude region, but with certain disparity in geophysical properties [see, Chapters 3 and 4].

The geomagnetic storms can trigger particle precipitation, which serves as source to the magnetospheric cusp and aurora. If the particle enters the high latitude atmosphere, it can initiate substantial ionisation within the MLT, causing composition changes. Enhanced magnetospheric convection (electric–field maps down along magnetic–field lines) and enhanced conductivity can ensue during magnetospheric disturbed time (Gold, 1959; Baker, 2001; Yue et al., 2011; Ogunjobi et al., 2014a). Furthermore, energetic particle inputs resulting from the geomagnetic storms, can alter the lower thermospheric composition and neutral winds (Price and Jacka, 1991). Also, the geomagnetic storms can be driven to near Earth by either an attendant of CIR, SI (see Friedel et al., 2002) or driven to Earth by the attendant of CME, MC (see Wang et al., 2003). In the following subsections, the phenomena resulting in occurrence of MC and SI are discussed.

1.5.1 Magnetic cloud event

The first transient decreases in the intensity of cosmic rays was explained by Morrison et al. (1954). They observed the reduction on the arrival of magnetised plasma clouds from the dynamic areas on the Sun. Cocconi et al. (1958) noted that an extended loop is formed by the magnetic field lines in such a cloud, which is anchored at both ends in the Sun. Galactic cosmic rays are diverged by the smooth and strong field lines in the loop. Gold (1962) also

suggests that these field lines might reconnect to produce a magnetic spume, completely detached from the Sun. Using spaceborne observations, Burlaga et al. (1982) analysed a magnetic loop behind a fortuitous interplanetary shock, and found organised magnetic field rotation. This whirling (loop) was alluded to as a magnetic cloud (MC). The MC from the twirling of solar wind can be traced to the Suns' corona [see Figure 1.8] and therefore, differs from the turbulence within the Interplanetary Coronal Mass Ejection (ICME).

Also, Burlaga et al. (1982) proposed that the highest geomagnetic storms are prevalent when the Earth is impacted by the MC tied to CME occurrence. MC is a short–lived discharge in the solar wind specified by a smooth turning of the magnetic field orientation, fairly strong fields, a low proton temperature and a low ratio of magnetic pressure to plasma pressure (Burlaga, 1988). MC is also characterised, by Lepping et al. (1990, 1997), as the boundary that distinguishes the foremost half of the southward tuning of the IMF (in z–component) and the trailing half of the strong northward turning, or vice versa. This IMF (i.e. IMF, B_z) is usually accompanied by a substantial density peak capable of compressing the magnetosphere (Ogunjobi et al., 2014a). Evidence for these characteristics is presented in Figure 1.9. The MLT response to a MC that eventuated on 8 November 2004 has been studied in this thesis (Chapter 3).

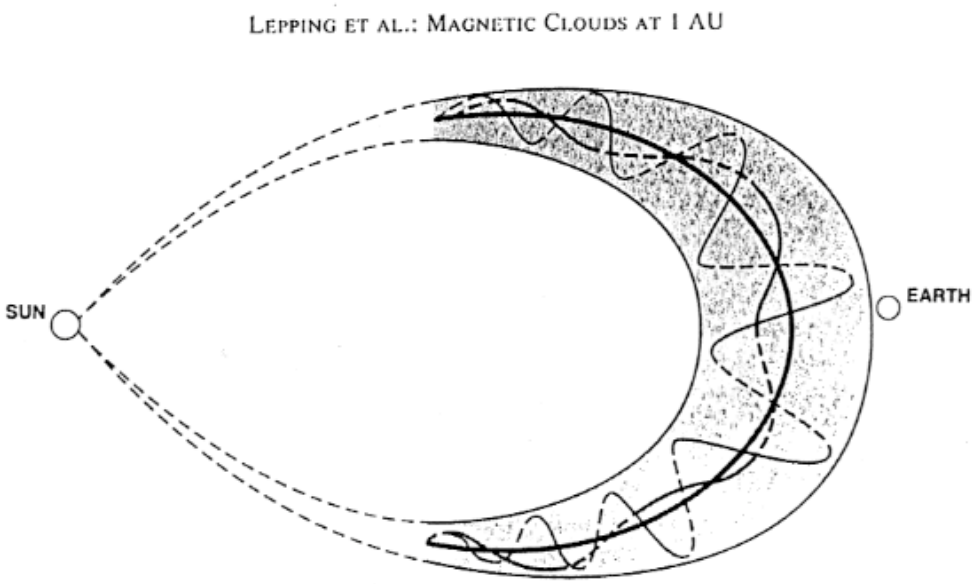

Figure 1.8: A schematic illustration of MC. Figure obtained from Lepping et al. (1990).

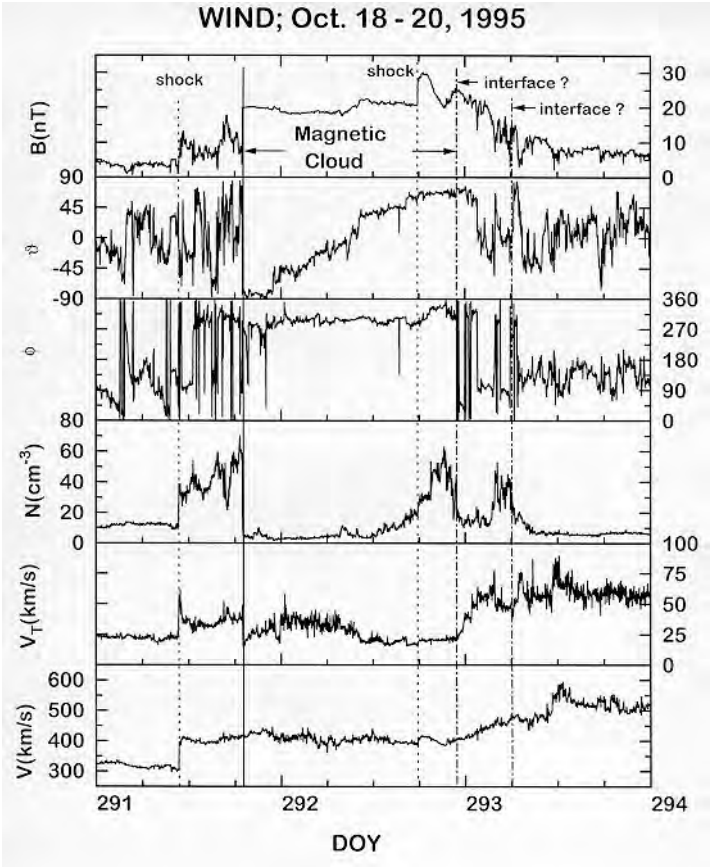

Figure 1.9: Magnetic and Solar wind Parameters showing conditions for MC occurrence. From (top to bottom) the magnetic field strength (B), the elevation (θ) and azimuth (ϕ) of the magnetic field direction, the proton density (N), the proton thermal speed (V_T) and the bulk velocity (V). Figure obtained from Lepping et al. (1997).

1.5.2 Stream interface event

The solar wind stream is generally found not to be uniform. The bimodal structure of the solar wind stream provides the mechanism for solar wind Stream Interface (SI) occurrence (Burlaga, 1974). The SI can be explained on the basis of this non–uniformity in solar wind streams, as shown in Figure 1.10. The SSWS from the vicinity of the streamer belt is continually at the leading side of the passing HSSWS which is emitted from the coronal holes. The HSSWS catches up with SSWS and, consequently, results in a compressed interface, when it is within the interplanetary medium. This compressed interface at the interplanetary environment is referred to as the stream interaction region. As previously noted, it is the recurring interface with the Sun that is refered to as the CIR. Note that, both SSWS and HSSWS can not mingle, due to the presence of the frozen magnetic field. Hence, the region that delineates these dense (i.e. slow–moving plasma) from the fast (i.e. less dense plasma) regions is the SI. This plasma flow driven by SI event toward Earth is characterised by a sudden drop in solar wind number density with a possible temperature change and a peak in velocity (Gosling et al., 1978). SI is a one–type storm driven event (Friedel et al., 2002; Dal Lago et al., 2002) which can trigger particle precipitation and then causes significant alteration in magnetic indices if it interacts with the upper atmosphere (Ogunjobi et al., 2014). SI as a CIR attendant does recur (Heber et al., 1999; Borovsky and Denton, 2008, 2009; Morley et al., 2010).

Due to this recurrence nature, according to Borovsky and Denton (2009), SI is particularly amenable to superposed epoch analysis (SEA). The SEA is a technique, useful in composition of time series data (see Section 2.3). The selected 27 SI–driven storms that occurred during period from 2002 to 2007 has been used in this thesis to examine the MLT temperature response (reader can see Chapter 4).

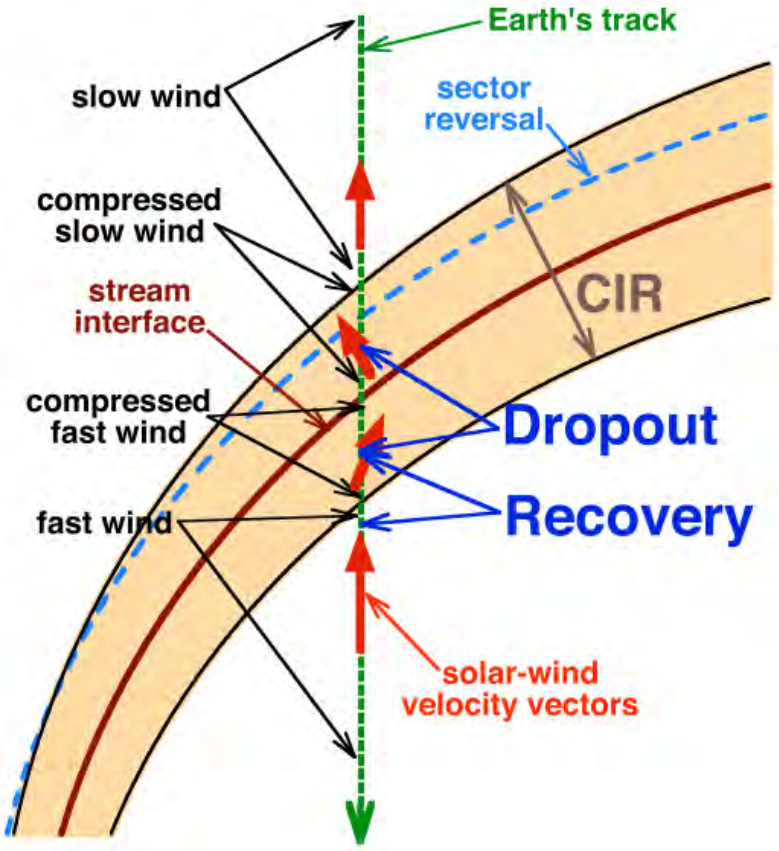

Figure 1.10: Schematic illustration of SI occurrence. The portion shaded with tan colour indicates CIR while the green dashed line is the Earth's track through the CIR. With respect to the GSE frame of reference, the movement of the Earth is downward with time. The direction of the solar wind flow is denoted with the arrows (red). The solar wind flows deflects to the left as it enters the CIR (compressed SSWS). The dark red line depicts SI. When the Earth crosses the SI, it leaves the region of compressed SSWS and moves into the region of compressed HSSWS. The flow deflection reverses from left to right (blue dotted line). The locations of the Earth along its track where the trapped energetic particle drop out (lost) as well as the recovery from dropout occur are denoted by dark blue arrows. Figure adopted from Borovsky and Denton (2010).

1.6 The high–latitude phenomena

At high–latitudes, the plasma drifts can be huge as a result of the forcing of magnetospheric origin. Hence, the ion drag term in the momentum equation will be significant for the neutral atmospheric dynamics. The ion drag force emerges from the $\vec{J} \times \vec{B}$ Lorentz force in the momentum equation for the neutral gas expressed as:

$$\vec{J} = \sigma(E + u \times \vec{B}) \times \vec{B} \tag{1.2}$$

where E is external electric field.

The plasma over the high–latitude region ionosphere (see Subsection 1.6.1) is mainly controlled by the electric field, ranging from the magnetosphere through the magnetic field lines. Note that, this is where solar wind–driven electric field begins. When the IMF rotates southward, it reconnects to the Earth's magnetic field lines. This will create open field lines that map into the high–latitude or, more precisely, polar atmosphere. Though the solar wind plasma is collisionless, it creates a dynamo effect when crossing magnetic field lines (B_{sw}), causing electric fields $E_{sw} = -V_{sw} \times B_{sw}$. The Earth's magnetic field lines are, generally, viewed as equivalent–potentials. Hence, the electric potential across the connected magnetic field lines will be mapped down to the polar cap. Consequently, this dawn–to–dusk electric field propels the plasma away from the Sun near the polar cap regions. The feedback flow is, perhaps, at the lower latitudes forming a two–cell convectional pattern. In contrast, when the IMF is northward, the plasma flow pattern becomes more complicated, often with more than two convection cells. For this thesis, various disturbed times were examined over high–latitudes with specific attention on Southern hemisphere high–latitude MLT and ionospheric region. The discussion on the high latitude MLT–Ionosphere interaction is more explicit in the following subsection.

1.6.1 High latitudes MLT and ionosphere

The ionosphere is known to be the ionised upper atmospheric layer of the Earth. It stretches between approximately 50 km and 1000 km of Earth's atmosphere. Ionising particles do not only come from the magnetosphere, but also from the ionosphere itself, provided a process for local electron acceleration is operating. However, the ionosphere can be described by energetic particle effects on radiowave propagation. This phenomena is a consequence of the presence and variation in the concentration of free electrons in the atmosphere. It should be noted that the UV radiation emanating from the Sun can heat the layer of neutral atmosphere and ionise it. The ionosphere can, generally, be viewed as a series of horizontal layers. The ionosphere, however, does not invariably conform to this simple description, especially over high–latitudes. Contrary to the mid–latitudes which are comparatively easier to study, the high–latitudes ionospheres are subject to a wider range of unexpected behaviour.

The ionosphere can be, mainly, sorted out based on its ionising layers, as depicted (with thermal variabilities) in Figure 1.11. These layers are called the D region (60–90 km), E region (90–150 km) and F region (150–1500 km) layers as shown in Figure 1.11 (right panel) while the corresponding vertical temperature at these layers is shown in Figure 1.11 (left panel). The altitude above the F layer is the magnetosphere, which has been previously discussed.

Such division is important, because of varying behaviour of terrestrial altitudes within the ionospheres. For instance, the altitudinal bands of the mesosphere (i.e, 50–100 km) and the lower thermosphere (i.e, 100–180 km), herein referred to as MLT, are embedded in the lower ionosphere. The energy balance of the high latitudes MLT remains an arduous scientific task. This is as a result of several complex phenomena that are involved in the MLT energy predictions. These complex situations range from the Earth's hemispherical disparities to the multiple external and internal activities capable of inducing concurrent heating and cooling. Roble (1995), noted that the MLT heating and cooling is primarily dependent on the effective conditions present per time. Intuitively, the mesosphere, for example, is characterised by

cooling as the altitude increases. However, particles can lose some of their energy to the MLT molecules, bringing about such effects as excitation, ionisation, dissociation and subsequent discharge of radiation and heating. This means that the MLT energy balance research can be advanced based on the arrival of varying Geospace events (see, Chapters 3, 4 and 5).

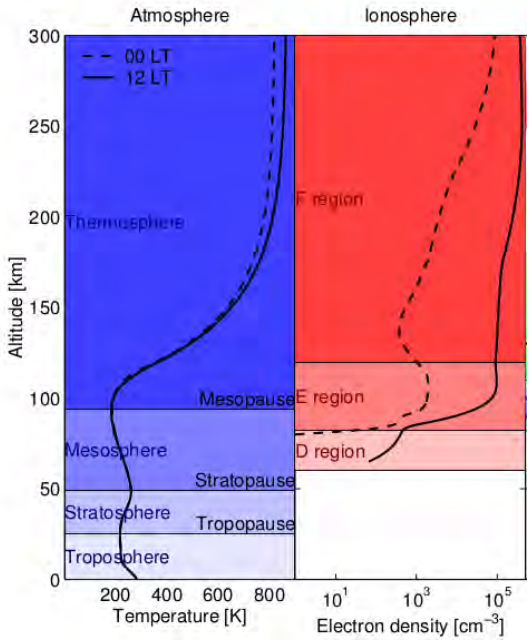

Figure 1.11: MSIS modelled thermal and magneto–ionic structure of the ionosphere. On the left is the neural temperature as a function of altitude over the vicinity of SANAE on 21 December 2005 at 00 hr and 12 hr local time and the resulting atmospheric layers. On the right are Modelled ionospheric electron density and the ionospheric layers. Figure plotted using MSIS Model, 2013.

The structure and variability of the ionosphere are not only affected by the solar radiation, but also by other solar dynamics (Callis et al., 1991), such as the solar wind and its embedded IMF, as well as in the Earth's magnetic field. The solar wind and its constituents can be driven towards the Earth by SI and MC, because of their capbility to arrive near the sub–solar point (or Earth bow shock nose). During any of these events, one or more adiabatic invariants can be broken, a phenomena that defines a geomagnetic storm. If this is the case, the energetic particles with drift motion in trapped radiation belts can become lost or dropped out. This is more likely to happen near the mirror points in the high latitudes (polar regions) where the trapped particles are at their closest approach to the surface of the

Earth. Nevertheless, energy dissipated by the lost particles can transport to the terrestrial atmosphere via precipitation. The particle energy could also, relatively, reach the upper atmosphere via electromagnetic radiation. As aforementioned, this sort of energy input into the atmosphere will result in ionisation of atmospheric neutral constituents.

Again, during this solar dynamical processes, high–energy particles ($>$ keV) can precipitate from the magnetospheric plasma sheet at high latitudes. The mechanisms responsible for acceleration of these particles to high energies are not yet fully understood, but upon getting into the high latitude atmosphere they can excite neutral species, emit photons and produce the optical aurora (Roble and Dickinson, 1970).

The aurora is a phenomenon that characterises the precipitating particle interactions with the Earth's magnetic field lines at the upper atmosphere (Roble and Dickinson, 1970; Hviuzova and Leontyev, 2001). In other words, solar wind can energise the radiation belt particles with enough energy to spiral into the atmosphere and produce an aurora. This aurora precipitation is confined to a zone known as the auroral oval. The bounds of the oval extend to lower latitudes on the nightside, rather than the dayside (Dungey, 1961; Sivjee and Shen, 1997; Zhang et al., 2013). There are two wide classes of aurora, namely, diffuse and discrete. The discrete aurora is structured and vivid, whereas, the diffuse aurora appears as a glimmer in the sky. Though they both take in similar overall intensities, nonetheless, the discrete form is easier to observe, due to the low intensity per unit area of the diffuse form. Notwithstanding, particle precipitation participates significantly in the coupling of the magnetosphere and ionosphere. Associated with the aurora precipitation is auroral radio absorption. This is brought about by the more energetic particles that penetrate to the lower layers of the ionosphere, or more precisely, the MLT in this context. The enhanced particle concentration leads to absorption of radio waves of cosmic origin in the mesopause. Energetic particles accompanied by a range of eV to several thousand keV energies, can penetrate down to lower thermosphere and mesosphere. These phenomena are pertinent at high latitudes during the intense geomagnetic storms. The intensity of a geomagnetic

storms, however, is best predicted with the specific Geospace event that drives the storms to the near Earth environment.

1.6.2 Particle precipitation effect on MLT energy balance

Precipitation pertains to the transport of energy within the Earth's magnetosphere into the high latitude upper atmosphere. The major origin of increased ionisation in the lower thermosphere is the result of upshot of the precipitating energetic particles depositing their energy. Particles can be dispersed via very large angles when there are collisions with the atmospheric neutral particles. If the resulting divergence increases the particle pitch angle, it can further impinge on the atmosphere. This will initiate collision and, ultimately, result in the loss of more energy. Conversely, if the divergence decreases the particle pitch angle, the particle is backscattered and may further penetrate on the other end of its bounce trajectory (Ogunjobi et al., 2014a).

Precipitation can also be in the shape of a relativistic burst. The relativistic (> 1 MeV) microburst is a short–duration burst of precipitating relativistic particles. The burst has a duration of approximately 100 ms, characterised by a sudden increase and slower decaying peak; and, occasionally, with a sawtooth–like structure of precipitation (O'Brien et al., 2004). This pattern indicates depleted particles from the bounce lost cone, as previously noted. Both MC and SI driven storms can trigger particle precipitation into the high latitude MLT. The induce changes in the Earth's magnetic field, resulting from the impact of either the MC or the SI structure seems to differ, as noted in Chapters 3 and 4.

Mesospheric cooling

Precipitated charged particles in the MLT lose their energy by ionising, dissociating and exciting the atmospheric atoms and molecules. Furthermore, energy is lost via radiating bremsstrahlung (electromagnetic radiation produced by the deceleration of a charged particle when deflected by another charged particle) in the aspect of acceleration in the Coloumb

field of the atomic nuclei. This initiates a number of different interdependent and synergistic processes, affecting the MLT energy budget. An instance of such a process is the likely effect of cooling, as shown in Figure 1.12, which could be originated by the direct particle impact on the mesosphere producing HOx (odd hydrogen). The HOx, though being minor constituents, could partly serve as catalyst in the destruction of ozone, resulting in mesospheric cooling. Likewise, increased ionisation due to particle precipitation can substantially influence the Pedersen conductivity and, thereby, Joule heating. In contrast, ionisation and dissociation can affect the composition and the associated chemical heating rates and infrared cooling rates. The modified temperature gradients, as well as the increased neutral–plasma interaction (ion drag), modify the neutral wind field. This constitutes a type of chain reaction which may again determine the temperature changes.

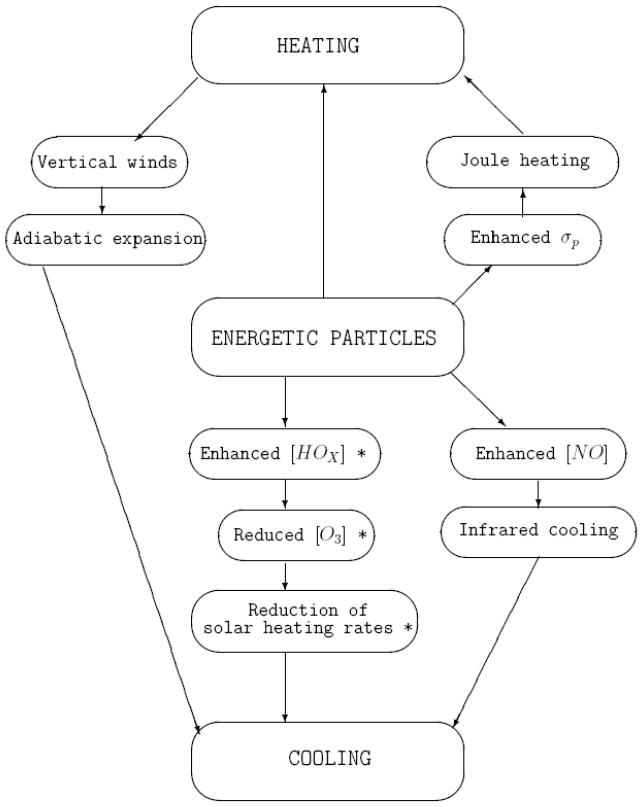

Figure 1.12: Schematic illustration of main energetic particle effects on the MLT. The boxes marked with * represent significant processes in the mesosphere.

Joule and particle heating

With reference to the multi–fluid theory, where neutrals and charged particles behave as isolated fluids interacting through collisions, mathematical expressions for the ionospheric current density, j, can be inferred. The definition of electric current density can be expressed as:

$$j = N_e e(v_i - v_e) \tag{1.3}$$

where N_e is number density of the electrons, e being the elementary charge, v_i is the velocity of the ions and v_e is the velocity of electrons. Assuming the reference frame of neutral gas (Rees, 1989), the results of the above expressions for the velocities, perpendicular to the field, become:

$$v_i \perp = \frac{\nu_{in} W_i E_\perp^{'} - W_i^{2b} X E_\perp^{'}}{B(\nu_{in}^2 + W_i^2)} \tag{1.4}$$

$$v_e \perp = \frac{-\nu_{en} \perp W_e E_\perp^{'} - W_e^{2b} X E_\perp^{'}}{B(\nu_{en}^2 + W_e^2)} \tag{1.5}$$

and parallel to the magnetic field:

$$v_e \parallel = \frac{eE_\parallel^{'}}{m_e(\nu_{en\parallel} + \nu_{in\parallel}}) \tag{1.6}$$

where the collisional frequency is given as ν, me as the electron mass, E' as effective electric field

$$(E' = E + v_n \times B),$$

where

^{b} is a unit vector along the magnetic field line, B, and W is the angular gyrofrequency. The electrons, ions and neutrals are denoted by e, i and n, respectively. While $\perp$ (perpendicular) and $\parallel$ (parallel) denote the direction of the variable with respect to B.

Based on this understanding, one can obtain the Joule dissipation rate, Q, arising from E and j as:

$$Q = j.E' \tag{1.7}$$

where the component of j parallel to E is called the Pedersen current.

Banks (1977) had earlier suggested that the energy deposited by the particle precipitation and Joule heating in the neutral atmosphere within the locality of the auroral oval are often comparable in magnitude. This scenario is depicted in Figure 1.13. The overall global Joule heating rate is, normally, larger than the sum of the global energy deposited by particle precipitation during high geomagnetic disturbances. Nevertheless, findings by Sinnhuber et al. (2012) specify that energy contribution from the precipitating particles is highly significant in the MLT budget.

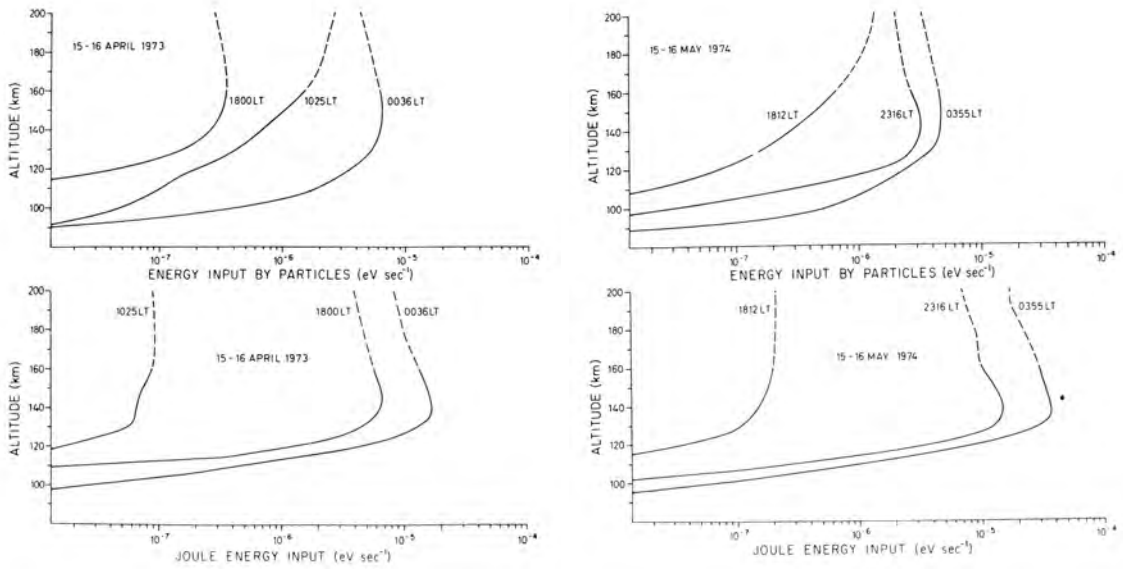

Figure 1.13: Profile of precipitating particle and Joule heating rate per neutral gas. From left to right are selected periods of 15–16 April 1973 and 15–16 May 1974. Figure adopted from Banks (1977).

Neutral heating

Precipitating energetic particles can be described as being extremely variable, both in time and intensity level. It can be considered as a localised inhomogeneous phenomenon. Since charged particle motion in the magnetosphere is governed by the geomagnetic field, the precipitation structures are aligned as ovals around the geomagnetic poles – a phenomena that describes aurora oval. The aurora particles, inclusive of electrons and protons population, can precipitate into the atmosphere. The empirical evidence indicates that the initial energy distribution of the particles gaining access into the atmosphere may be expressed as an exponential functions, $j_{exp}(E)$, and/or Maxwellian, $j_M(E)$, often with multiple terms. A single exponential and Maxwellian spectrum can be represented in the form of Equations 1.8 and 1.9 respectively, where A_0 is the particle flux, and E and E_0 are energy and its characteristics, respectively:

$$j_{exp}(E) = A_0 exp\frac{-E}{E_0} \tag{1.8}$$

$$j_M(E) = A_0 E exp\frac{-E}{E_0} \tag{1.9}$$

Particles precipitating in the atmosphere may go through charge exchange in collisions with the neutral gas if it is accelerated to relativistic energy. Relativistic particle precipitation can be initiated by geomagnetic storms driven by MC or SI. Within these structures, energy deposited by particles can be more homogeneous and outspread, depending on the geophysical conditions that followed the event. The outspread and the extents of homogeneity depends on the particle population. A critique of the estimated penetration deepness for various proton and electron energies population is presented in Figure 1.14. Although the value presented in the figure should be regarded as an average height where, most of the particle's energy have been absorbed by inelastic collisions (Maehlum, 1973). Electrons and protons ranging from over 1 keV and 50 keV, respectively, can deposit most of their energy in the MLT region. The physical activity connected with particulate heating are, predomi-

nantly, similar to those that governs solar heating of the atmosphere (Rees, 1964; Roble and Dickinson, 1970; Rees et al., 1983; Rees, 1989). Figure 1.14 depicts the efficient processes most momentous to neutral heating. The average loss of energy per unit pathlength from collisions with orbital electrons, can be appraised according to the Rohrlich and Carlson (1954) formulation:

$$L(E) = \frac{0.1536}{\beta}\{\Sigma_i w_i \frac{Z_i}{A_i}\}\{log[\frac{\tau^2(\tau+2)}{2(I/mc^2)^2}] + 1 - \beta^2 + [\frac{\tau^2}{8} - (2\tau+1)log_2]/(\tau+1)^2\}. \quad (1.10)$$

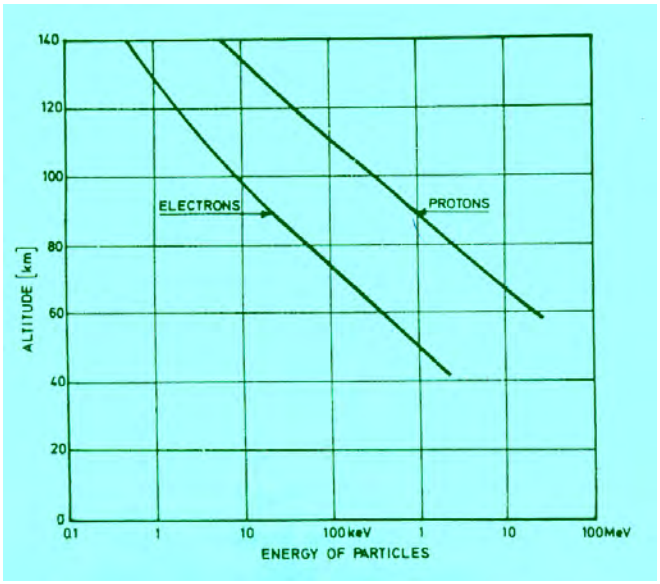

Figure 1.14: Vertical penetration depth of incident particles onto the atmosphere. Figure adopted from Maehlum (1973).

where, the loss of energy per unit pathlength is given as $L(E)$ in the unit of $(MeVcm^2g^{-1})$; E is kinetic energy of electrons in the unit of (MeV); $mc^2(= 0.511MeV)$ is rest mass of electron;

$$\tau = \frac{E}{mc^2};$$

$$\beta = \frac{\nu}{c},$$

where ν is velocity of the electron and the velocity of light is denoted by c; A_i, Z_i and w_i are the atomic weight, atomic number and weight fraction of the medium i'th constituent

respectively and, i is the medium (atmosphere in this case) mean excitation energy.

The flow chart in Figure 1.15 shows that ionisation, dissociation, as well as chemical processes can, consequently, result in electronically excited levels. This can be, collisionally, deactivated using the stopping power provided by Equation 1.10. O and N_2 are the only neutral species that have ample concentration and radiative lifetimes to participate, appreciably, in neutral heating through quenching. Additionally, the flow chart demonstrates that the collisions between electrons, ions and other neutral species contribute to neutral heating, as the overall ion and electron temperature are more than the neutral temperature.

The sum of the particle energy that contribute to neutral heating, and the time scale that the heating occurs are essential when considering temperature response to particle precipitation. The efficiency of neutral heating can be described as the local rate at which the neutral gas is heated. Model calculations indicate that, the heating efficiency is roughly independent of both the overall fluxes of energy and the energy characteristics of the Maxwellian spectrum. This heating efficiency is found to be over 50% complete at wide altitude interval, but drops at about 200 km as a result of the synthesis of transport effects, decreasing collisional deactivation, and alterations in compositions (Berger et al., 1970). Nonetheless, the heating efficiency is not completely free of inaccuracies. All neutral and ionic chemicals reactions have time factors that are functions of temperature, height composition and density. Computation of the temporal development of the neutral gas heating efficiency, carried out by Berger et al. (1970); Rees et al. (1983) and Rees (1989) indicate that the efficiency reach a fairly constant value in just few minutes after the aurora. This implies that the heating rate is also a time varying quantity which depends on the specific condition per time. The majority of the recombination and ion–atom exchange reactions have unchanging temporal factors, whereas the responses pertaining to NO_x (odd nitrogen) species may have a fairly longer time constant.

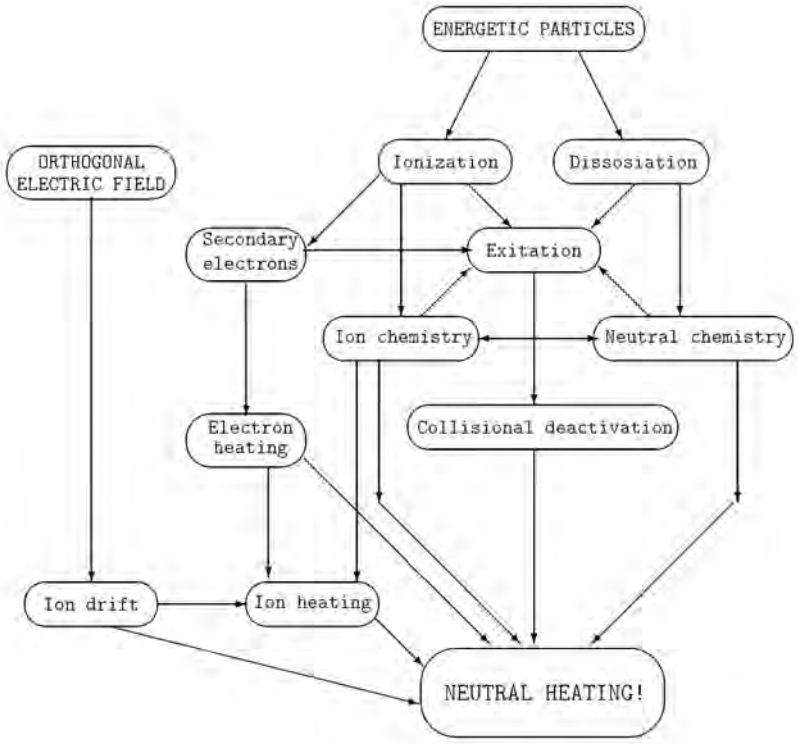

Figure 1.15: A flow chart of processes resulting to neutral heating. Figure adopted from Rees et al. (1983).

1.7 Dynamics and thermal state of the high latitude MLT

In Subsection 1.6.1, it was mentioned that, the Earth's atmosphere can be divided according to the vertical structure of the temperature field. With reference to this structure, the Earth's atmosphere consists of four layers namely: the troposphere, the stratosphere, the mesosphere and the thermosphere.

A number of fascinating Geospace events take place in the high latitude (polar) mesosphere. Most meteors (a falling rocky object that produces streak of light through the Earth's atmosphere), for instance, happen and glow up there. Meteors can be spotted by the naked eye, between altitudes of 65 km and 120 km, above the Earth's surface. Another interesting visual phenomenon in the mesosphere is, noctilucent clouds (NLC) which occur in the high latitude regions during summer. This event (NLC), and some others (e.g PMSE), occurring at the high latitude mesosphere have been suggested to be dependent on

temperature modifications (e.g, Rapp and Lübken, 2004; Hervig et al., 2009).

1.7.1 PMSE event

The mean mesospheric temperature field at different altitudes is in roughly radiative equilibrium (Andrews et al., 1987). Nonetheless, near the high latitude (Polar) mesopause (about 90–100 km altitudes), eddy motions (waves) can cause remarkable local departures from equilibrium. In consequence, the Polar mesosphere is much cooler than radiative equilibrium in summer and warmer in the winter. The zonal wind is in balance with the latitudinal temperature gradient, as illustrated by the thermal wind equation:

$$\frac{\delta u}{\delta z} = -\frac{r}{fHR}\frac{\delta T}{\delta \phi}, \tag{1.11}$$

where u is taken as the zonal wind velocity, z as the vertical coordinate, f as the Coriolis parameter, r as the gas constant for air, R as the radius of the Earth, H as the scale height and T as latitudinal temperatures.

The highest temperature in the troposphere is usually found at the equator and it lessens as it approaches the polar regions. This circulation of temperature gradient, might result in increased eastward zonal wind with altitude. In the summer hemisphere stratosphere, temperature rises to the maximum values. This enables dominance of westward flows during the summer stratosphere and eastward wind flows during the stratosphere winter periods. Typical latitude–height of the solstice mean zonal wind fields, averaged over all longitudes, is illustrated in Figure 1.16. Gravity waves propagate from sources in the troposphere to the mesospheric heights and, interact with the zonal flow. This interaction causes the eastward propagating gravity waves to arrive at the summer mesosphere, where they break. Contrarily, in winter, the westward propagating gravity waves reach the mesospheric heights. The momentum flux and energy deposited by the gravity waves breaking may slow down the zonal wind flow (Lindzen, 1981; Offermann, 1985) and, by thermal wind balances, modifies the temperature field. This causes a rise in meridional circulation, which is typified by the air mass upwelling during summer and downwelling during winter (Andrews et al., 1987). With

this characteristics, the zonal–mean meridional flow circulates from the summer hemisphere to the winter hemisphere mainly at mesopause heights as shown in Figure 1.17. When the air mass is uplifted from its equilibrium state, the volume expands adiabatically on the expense of internal energy of the parcel, resulting in decrease in temperature. Hence, during summer time in the Southern hemisphere, an equatorward (negative flow) wind is linked with the cold air transport while the transport of warm air in winter is linked with the poleward wind (Andrews et al., 1987). This pole to pole circulation is, perhaps, the cause of increased water vapour during summer than winter. The cross section of the seasonal mean temperature, averaged over longitudes, for solstice season is depicted in Figure 1.18.

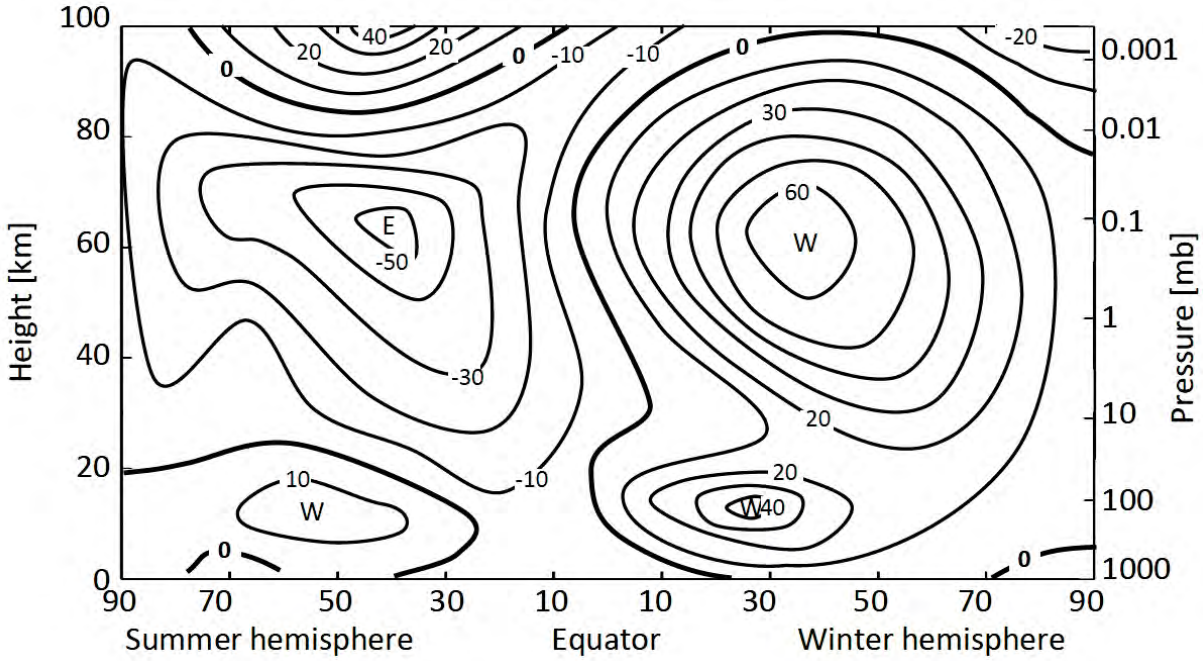

Figure 1.16: Schematic contours of latitude–height section of a typical zonal mean wind speeds. W and E denote centers of westerly and easterly winds, respectively. Negative values denote winds from the east. Figure adopted from Andrews et al. (1987).

As a result of meridional circulations induced by gravity waves, lower temperatures can be reached at Polar mesopause during summer. For instance, from November to February in the Southern hemisphere polar region, lower temperatures (< 130 K, Lübken et al., 2004) are usually found which enable ice particles to form from water vapor at the mesopause. These

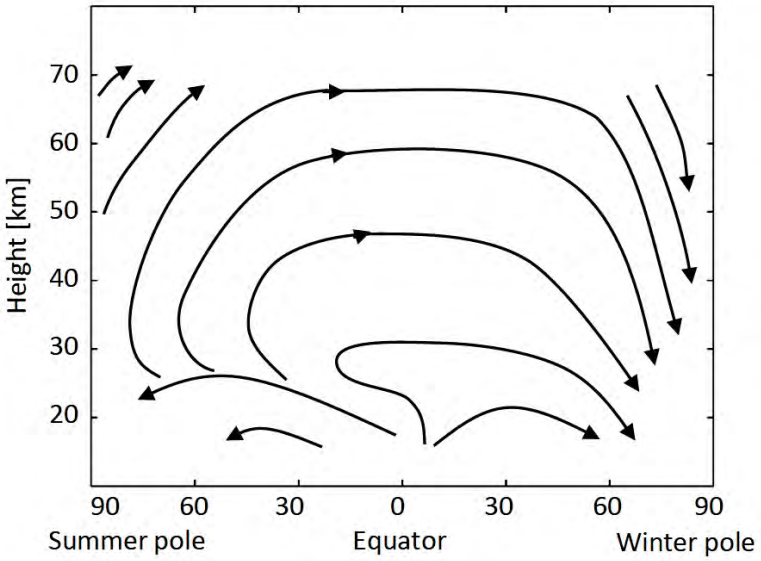

Figure 1.17: Schematic contours of streamlines of the solstice adiabatic circulation in the MLT. Figure adopted from Andrews et al. (1987).

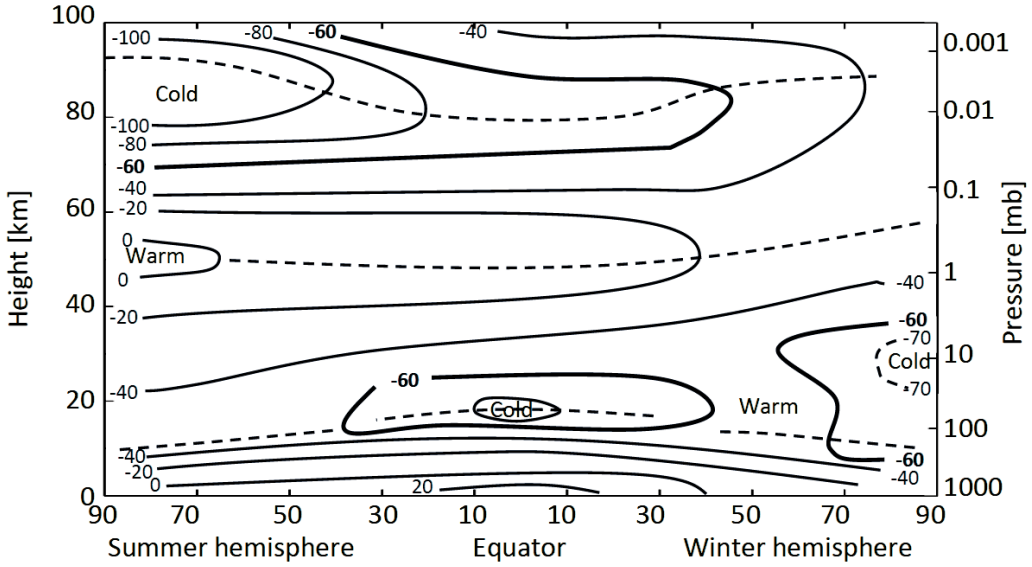

Figure 1.18: Schematic contours of latitude–height section of zonal mean temperature during solstice conditions. Figure adopted from Andrews et al. (1987).

ice particles are immersed in the D–region plasma, where free electrons are firmly stuck to their surfaces (For example, Huaman and B., 1999; Smiley et al., 2003), forming charged–ice particles. Also, gravity waves break at the same altitudes, producing turbulence. Turbulence in turn, causes disproportionate distribution of charged–ice particles and irregular spatial distribution of electron number density. The interactions of the charged–ice particle and mesospheric air turbulence, initiated by propagating gravity waves, results in strong radar backscatter echoes (bragg's scattering) in the Polar summer mesosphere. The resulting irregularities in the radar refractive index, termed PMSE, was first noted by Ecklund and Balsley (1981).

In the past few years, the PMSE has been closely linked to visible ice particles below 90 km altitude, known as NLC (Leslie, 1885; Cho, 1997; Rapp and Lübken, 2004). The NLC comprise of the largest charged–ice particles (over $\sim$20 nm), which can be visually observed from the ground as a silver–grey pattern (see Figure 1.19).

The NLC and PMSE phenomena arise from the formation of ice particles in the low temperatures of the polar summer mesopause. NLC in particular has been suspected to be, perhaps, a good index of global change in the middle atmosphere (For example, Thomas and Olivero, 2001). It has been suggested, nevertheless, that NLC and PMSE are comparatively different in their manifestations. NLC indicate only the presence of thin water–ice particles, formed at a low summer mesopause temperature, between 120 to 150 K (Hervig et al., 2009), while PMSE exists because the electrically charged–ice particles (on the scale of Bragg's wavelength) reduce the mobility of free electrons (see, Röttger, 1994; Rapp and Lübken, 2004). Thus, the phenomena of PMSE formation can be ascribed to both ionospheric plasma conditions and the thermal variations in the mesosphere, as depicted in Figure 1.20. Also, PMSE observations with radar have the advantage of being continuous, unlike NLC which depends on the observer and weather conditions (in the case of 'lidar 'usage). Thus, in an alternative to NLC, PMSE observations might contribute to the understanding of Polar mesospheric temperature changes (Huaman and B., 1999; Lübken et al., 2004).

Figure 1.19: Photograph of Noctilucent Clouds observed over Southern hemisphere polar region on 30 January 2010. Figure adopted from N.A.S.A. (2010).

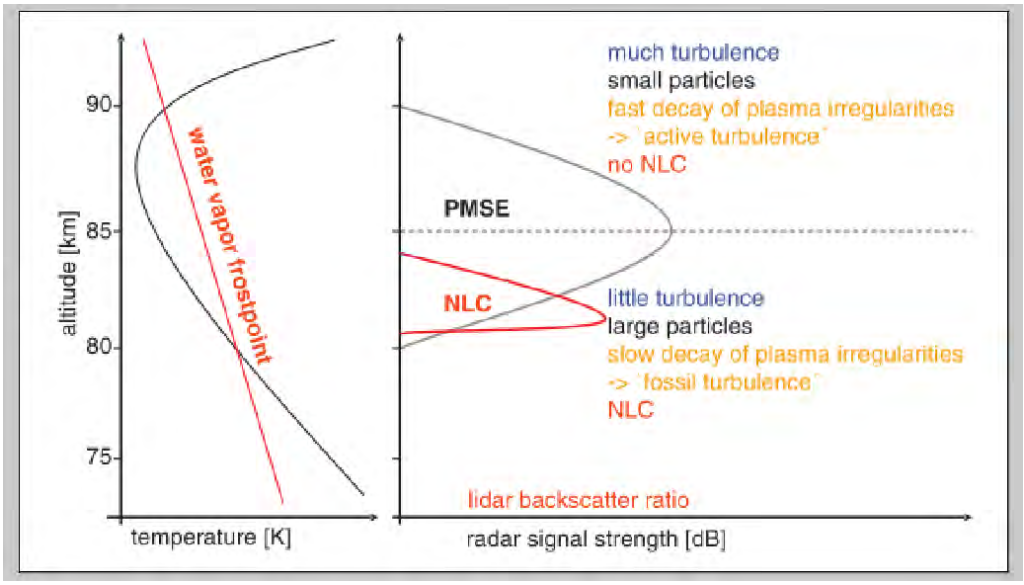

Figure 1.20: Schematic illustration of the altitude distribution of PMSE (black line, grey shading), NLC (red line) and the relevant physical mechanisms at different altitudes. Figure adopted from Rapp and Lübken (2004).

1.8 Geospace events as indicators of MLT temperature changes

One of the efforts to examine the energy budget of the MLT–region in totality was made in the atmospheric energy budget campaign in Northern Europe in 1980 (Offermann, 1985). However, their campaign was focused on winter night time conditions at high latitudes. Table 1.1 shows the energy budget at 90 km for two rocket salvoes, launched from Andøya in the Northern hemisphere high latitude, during different geomagnetic activity levels. The Joule heating shows no substantial contribution at mesospheric altitude. Under disturbed conditions, the particle heating rates was seen to be more than doubled. However, the heating rates were dominated by the variations of other energy sources and sinks which were unconnected to the geomagnetic activity. A lesser stratospheric warming occurred simultaneously with the quiet conditions, effectuating mesospheric cooling.

The infrared cooling rates by CO_2 15 μ m were very contingent on the local temperature, cutting it to half of the value that one would have anticipated for normal winter conditions. The turbulence as the largest energy sink, was proposed to be the most likely factor responsible for -10 K/d. Similarly it acted upon the atomic oxygen density profile, which lessen the chemicals heating rates from the reactions (Offermann, 1985). Nevertheless, it was not resolved whether, or not, there was a direct relationship between the energy input during specific Geospace event and the turbulent state of the high latitude mesosphere.

Table 1.1: The heating and cooling, per one day, at 90 km altitude. Salvo C represents quiet geomagnetic conditions and salvo A2 represents fairly disturbed geomagnetic conditions, according to (Offermann, 1985).

Energy source/sink	salvo C (10/11 Nov. 1980)	salvo A2 (30 Nov./1. Dec 1980)
Particle precipitation	$\leq$ 1 K	$\leq$ 2.5 K
IR cooling (15 μm)	-4 K	-7.5 K
Atomic Oxygen recombination	16 K	5 K
Solar irradiation	5 K	5 K
Wave dissipation	$<$ 1 K	1 K
Turbulent cooling	0 K	-10 K
Sum	+19 K	-4 K

Various attempts to model the temperature response to induced particle precipitation have been made. In essence, models which can describe the vertical coupling processes in varying

altitudes of the atmosphere (for instance Berger et al., 1970), are suitable to study MLT temperature responses. A concurrent lower thermosphere cooling of approximately 10 K was obtained by Zadorozhny et al. (1994) in a model that was combined with the meteorological M–100B rockets data in October 1989. Similarly, Jackman et al. (2007) employed proton flux measurements from the GOES (Geostationary Operational Environmental Satellites) as an input in the TIME–GCM (Thermosphere Ionosphere Mesosphere Electrodynamics General Circulation Model) for the SPE (Solar Proton Event) that occurred in October–November 2003. Figure 1.21 shows results using the model estimation for 30 October 2003, close to the time of maximum solar proton fluxes. Nonetheless, the overall zonal average Joule heating in the upper mesosphere (Figure 1.21 a) was minimal. The highest Joule heating rates eventuate at about 70 km. If the model had added energetic electron fluxes, the Joule heating would, perhaps, be comparatively larger in the upper mesosphere. Modifications in the solar and chemical heating rates appear to be more obvious in Figure 1.21 b. The reduced ozone lead to smaller temperature increases in the sunlit atmosphere below 77 km. The vertical wind was forced downward in the Southern hemisphere, causing rise in atomic oxygen. In combination with the storms triggered particle precipitation, initiating HO_x constituents, the atomic oxygen enhancement can result in increase in exothermic reactions, thereby cooling.

Additionally, the increase in atomic oxygen can lead to further O–CO_2 reactions, thereby excitation of CO_2 molecules, and consequently more cooling. The amplified downward winds also created adiabatic heating above 75 km in the high latitude of the Southern hemisphere. Figure 1.21 c shows the overall zonal temperature modifications. The estimated temperature modifications are concentrated in the sunlit Southern hemisphere, with extreme cooling of -2.6 K near 65 km. The maximum heating of 2.5 K was found close to 90 km, whereas the temperature changes in the Northern hemisphere was very little.

The contradictions in both observations and modelled results could partly be due to unaccounted inputs from Geospace events. Some models do not take into account, the localised

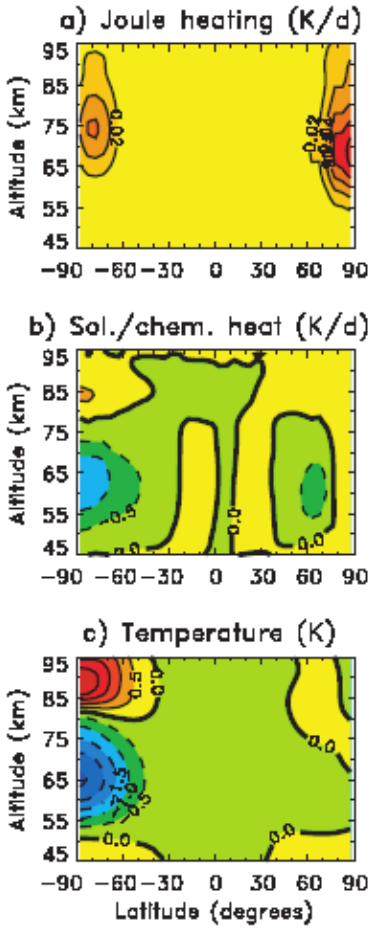

Figure 1.21: Modelled joule heating (a), solar heating and the chemical heating (b) and the temperature modifications (c) due to energetic particle precipitation on 30 October 2003. Figure adopted from Jackman et al. (2007).

structures that could be observed in some specific Geospace event. In addition, some models used only proton fluxes as input, and did not account for potentially large electron fluxes which also could affect the MLT. As seen from the aforementioned expansive energy budget campaign (Offermann, 1985), atmospheric variations independent of the geomagnetic disturbances may dominate and conceal probable effect from precipitating particles. So, the complicated energy budget encourage us to proceed, with care, in verifying the effect of Geospace events on the MLT energy balance. Furthermore, observation of temperature response to Geospace events remain sparse in the Southern hemisphere Polar regions, which are the regions of interest in this study.

Layered phenomena

In reference to previous studies on the influence of triggered precipitation on MLT budget, it is apparent that ionisation and radiative processes cannot fully explain the curious seasonal variation of temperatures with extremely low values at the summer mesopause and, in contrast, large values in winter (some 50–70° warmer compared to summer) (Stroud et al., 1959; Theon et al., 1967). It was earlier suggested by Murgatroyd and Singleton (1961) that, dynamical ageostrophic processes drive the upper atmosphere away from the radiative balance and initiate upwelling in summer and downwelling in winter. Some theoretical works suggested that gravity waves initiate the momentum required to cause such ageostrophic motions (Lindzen, 1981). Since the tropospheric topography play a significant role in the generation of gravity waves, it is anticipated that the Antarctic mesosphere is less controlled by dynamical processes compared to the Arctic; since there is less orographic terrain in the Southern hemisphere Polar latitudes. This idea triggered an initiative to examine temperatures in the summer mesosphere at polar latitudes by means of layered phenomena, such as PMSE event.

For over three decades, just few attempts have been made to obtain convincing correlations between PMSE and mesospheric temperature. Therefore, PMSE aspects, revealed by

various instruments, are still expected in this field. However, the first direct simultaneous observation of temperature and of PMSE was demonstrated by Kirkwood et al. (2002) with SkiYMET (All–Sky Interferometric Meteor) radar and ESRAD radar (Esrange Radar) near Kiruna in Sweden. Kirkwood et al. (2002) examined the response of PMSE to temperature fluctuations associated with 5–day planetary waves and found that the temperature was the most significant parameter affecting PMSE occurrence. Some previous work (e.g, Morris et al., 2009) observed minor linkage between PMSE and temperatures with satellite observation. Smirnova et al. (2010) also suggested that, pole to pole circulation would result in an extremely low temperature around summer solstice to enable charged ice–particle formation, hence high PMSE production. For the first time, this study reports various characteristics of PMSE observed by SuperDAN SANAE IV HF radar (Chapter 5). Furthermore, the mesospheric temperature changes in relation to SuperDARN–PMSE occurrence rate has been studied.

1.9 Thesis outline

The latter parts of this thesis are concerned with the observations of Geospace events, particularly MC, SI and PMSE events. Chapter 2 describes various instruments and techniques that are useful in observing perturbations initiated by these Geospace events, with a particular focus on the measurements and models used in this study. Chapter 3 discusses the MLT effects in response to a propitious MC–driven geomagnetic storm, which eventuated on 08 November, 2004. In Chapter 4, some selected SI driven storms are discussed, a description of wave–particle interactions is given and the particle precipitation which results in a temperature modifications over SANAE IV are outlined. Chapter 5 discusses, for the first time, various characteristics of SuperDARN–PMSE and its relationship with mesospheric temperature over SANAE IV. The content of Chapter 6 does not strictly conform to the theme of this thesis: it considers mid–latitude thermospheric zonal winds variation which are driven by a pressure gradient rather than induced particle precipitation, and thus has no

specific connection to Geospace events. It is, nonetheless, still relevant as it pertains to the magnetosphere and neutral atmosphere below and thus provides useful information which applies to the magnetosphere–MLT coupling processes. The concluding remarks and future perspectives are given in Chapter 7.

References

Andrew, J.K., 2002. Energy deposition in the lower auroral ionosphere through energetic particle precipitation. Ph.D. thesis. Department of Communication Systems, Lancaster University Lancaster, UK.

Andrews, D., Holton, J., Leovy, C., 1987. Middle Atmospheric Dynamics. Academic Press, New York and London.

Baker, D., 2001. Coupling between the solar wind, magnetosphere, ionosphere, and neutral atmosphere, in: Murdin, P. (Ed.), Encyclopedia of Astronomy and Astrophysics. Institute of Physics Publishing, Bristol, UK, pp. 2911–2914.

Baker, D.N., Kaneka, S.G., Hoxie, V.C., et al., 2013. A long-lived relativistic electron storage ring embedded in earth's outer Van Allen belt . Science 340, 186. doi:10.1126/science.1233518.

Banks, P.M., 1977. Observation of Joule and particle heating in the auroral zone. Journal of Solar-Terrestrial Physics 39, 179–193.

Baumjohann, W., Treumann, R.A., 1996. Basic Space Plasma Physics. Imperial College Press.

Berger, M.J., Seltzer, S.M., Maeda, K., 1970. Energy deposition by auroral electrons in the atmosphere. Journal of Atmospheric and Terrestrial Physics 32, 1015–1045.

Borovsky, J.E., Denton, M.H., 2006. Differences between CME-driven storms and CIR-driven storms. Journal of Geophysical Research 111, A07S08. doi:10.1029/2005JA011447.

Borovsky, J.E., Denton, M.H., 2008. A statistical look at plasmapheric drainage plume. Journal of Geophysical Research 113, A09221. doi:10.1029/2007JA012994.

Borovsky, J.E., Denton, M.H., 2009. Relativistic-electron dropouts and recovery: a superposed epoch study of the magnetosphere and the solar wind. Journal of Geophysical Research 114, A02201. doi:10.1029/2008JA013128.

Borovsky, J.E., Denton, M.H., 2010. Solar wind turbulence and shear: A superposed-epoch analysis of corotating interaction regions at 1 AU. Journal of Geophysical Research 115, A10101. doi:10.1029/2009JA014966.

Bothmer, V., Schwenn, R., 1995. The Interplanetary and Solar Causes of Major Geomagnetic Storms. Journal of Geomagnetism and Geoelectricity 47, 1127–1132.

Burlaga, L.F., 1974. Interplanetary stream interfaces. Journal of Geophysical Research 79, 3717–3725. doi:10.1029/JA679i025P03717.

Burlaga, L.F., 1988. Magnetic clouds: constant alpha force-free configurations. Journal of Geophysical Research 93, 7217.

Burlaga, L.F., Kein, L.F., Sheeley, L., Michels, N.R., Howard, D.J., Koomen, R.A., Schwenm, M.J., Rosenbauer, H., 1982. A magnetic cloud and a coronal mass ejection. Geophysical Research Letters 9, 1317–1320.

Callis, L.B., Boughner, R.E., Baker, D.N., Blake, J.B., Lambeth, J.D., 1991. Precipitation relativistic electrons - Their long-term effect on stratospheric odd nitrogen levels. Journal of Geophysical Research 96, 2939–2976.

Cho, J.Y.N., 1997. An updated review of polar mesosphere summer echoes' observation, theory, and their relationship. Journal of Geophysical Research 102 (D2), 2001–2020.

Cocconi, G., Gold, T., Greisen, K., Hayakawa, S., Morrison, J.P., 1958. The cosmic ray flare effect. Nuovo Climento 8, 161.

Dal Lago, A., Gonzalez, W.D., Gonzalez, A.L.C., Vieira, L.E.A., 2002. Stream-interacting magnetic clouds causing very intense geomagnetic storms. Advances in Space Research 30, 2225–2229. doi:10.1016/S0273-1177(02)80230-7.

Denton, M.H., Borovsky, J.E., Horne, R.B., McPherron, R.L., Morley, S.K., Tsurutani, B.T., 2009. Introduction to special issue on high speed solar wind streams and geospace interactions (HSS-GI). Journal of Atmospheric and Solar-Terrestrial Physics 71, 1011–1013. doi:10.1016/j.jastp.2008.

Dungey, J.W., 1961. Interplanetary Magnetic Field and the Auroral Zones. Physical Review Letters 6, 47–48.

Ecklund, W., Balsley, B., 1981. Long–term observations of the Arctic mesosphere with the MST radar at Poker Flat, Alaska. Journal of Geophysical Research 86, 7777–7780.

Friedel, R.H.W., Reeves, G., Obara, T., 2002. Relativistic electron dynamics in the inner magnetophere—A review. Journal of Atmospheric and Solar-Terrestrial Physics 64, 265.

Ganushkina, N.Y., Dandouras, I., Shprits, Y.Y., Cao, J., 2011. Locations of boundaries of outer and inner radiation belts as observed by Cluster and Double Star. Journal of Geophysical Research 116, A09234. doi:10.1029/2010JA016376.

Gold, T., 1959. Motions in the Magnetosphere of the Earth. Journal of Geophysical Research 64, 1219.

Gold, T., 1962. Magnetic Storms. Space Science Reviews 1, 100–114. doi:10.1007/BF00174637.

Gosling, J.T., Asbridge, J., Bame, S., Feldman, W., 1978. Solar wind stream interfaces. Journal of Geophysical Research 83, 1401.

Heber, B., Sanderson, T.R., Zhang, M., 1999. Corotating interaction regions. Advances in Space Research 23, 567–579. doi:10.1016/S0273-1177(99)80013-1.

Hervig, M.E., Gordley, L.L., Russell III, J.M., Bailey, S.M., 2009. SOFIE PMC observations during the northern summer of 2007. Journal of Solar–Terestrial Physics 71, 331–339. doi:10.1016/j.jastp.2008.08.010.

Hill, T.W., Dessler, A.J., 1991. Plasma motions in planetary magnetospheres. Science 252, 410.

Huaman, M.M., B., B.B., 1999. Differences in near–mesopause summer winds, temperatures, and water vapour at northern and southern latitudes as possible causal factors for inter–hemispheric PMSE differences. Geophysical Research Letters 26, 1529–1532.

Hviuzova, T., Leontyev, S., 2001. Characteristics of aurora spectra connected with non-stationary solar wind streams. Geomagnetism and Aeronomy 41, 337–341.

Jackman, C.H., Roble, R.G., Fleming, E.L., 2007. Mesospheric dynamical changes induces by the solar proton events in October-November 2003. Geophysical Research Letters 34. doi:10.1029/2006GL028328.

Jursa, A.S., 1985. Handbook of geophysics and the space environment. 4th edtion ed., Air Force Geophysics Laboratory.

Kirkwood, S., Barabash, V., Brandstrom, B., Hocking, W., Mostrom, A., Mitchell, N., Stebel, K., 2002. Noctilucent clouds, PMSE and 5-day planetary waves: a case study. Geophysical Research Letters 29, 50.1–50.4.

Kivelson, M.G., Russell, C.T., 1995. Introduction to Space Physics. Cambridge University Press. pp. 3–16.

Lepping, R.P., Burlaga, L.F., Szabo, A., Ogilvie, K., Mish, W., Vassiliadis, D., Lazarus, A., Steinberg, J.T., Farrugia, C., Janoo, L., Mariani, F., 1997. The Wind magnetic cloud and events of October 18-20, 1995: Interplanetary properties and as triggers for geomagnetic activity. Journal of Geophysical Research 102, 14049–14064. doi:10.1029/97JA00272.

Lepping, R.P., Jones, J.A., Burlaga, L.F., 1990. Magnetic field structure of interplanetary magnetic clouds at 1 AU. Journal of Geophysical Research 95, 11957.

Leslie, R.C., 1885. Sky Glows. Nature 32, 245. doi:10.1038/032245a0.

Lindzen, R.S., 1981. Turbulence and stress owing to gravity wave and tidal breakdown. Journal of Geophysical Research 86, 9707–9714. doi:10.1029/JC086iC10p09707.

Lübken, F.J., Mullemann, A., Jarvis, M.J., 2004. Temperatures and horizontal winds in the Antarctic summer mesosphere. Journal of Geophysical Research 109, D24112. doi:10.1029/2004JD005133.

Maehlum, B.N., 1973. Particle precipitation: Scattering and absorption. in Cosmical Geophysics, Universitetsforlaget. pp. 211–219.

Morley, S.K., Friedel, R.H.W., Spanswick, E.L., Reeves, G.D., Steinberg, J.T., Koller, J., Cayton, T., Noveroske, E., 2010. Dropouts of the outer electron radiation belt in response to solar wind stream interfaces: global positioning system observations. Proceedings of Royal Society 466, 3329–3350.

Morris, R., Holdsworth, D., Klekociuk, A., Latteck, R., Murphy, D., Singer, W., 2009. Inner-hemispheric asymmetry in polar mesosphere summer echoes and temperature 69 latitude. Journal of Atmospheric and Solar-Terrestrial Physics 71, 464–469.

Morrison, P., Olbert, S., Rossi, B., 1954. The origin of cosmic rays. Physical Review 94, 440.

Murgatroyd, R.J., Singleton, F., 1961. Possible meridional circulations in the stratosphere and mesosphere. Q. J. R. Meteorological Society 87, 125–135.

N.A.S.A., 2010. Polar mesospheric clouds, southern hemisphere. URL: http://visibleearth.nasa.gov.

O'Brien, T., Looper, M., Blake, J., 2004. Quantification of relativistic electron microburst loss during the GEM storms. Journal of Geophysical Research Letter 31, L04802.

Offermann, D., 1985. The Energy Budget Campaign 1980 - Introductory review. Journal of Atmospheric and Terrestrial Physics 47, 1–26.

Ogunjobi, O., Sivakumar, V., Mbatha, N., 2014a. A case study of energy deposition and absorption by magnetic cloud electrons and protons over the high latitude stations: effects on the mesosphere and lower thermosphere. Terrestrial, Atmospheric and Oceanic Sciences 25, 219–232. doi:10.3319/TAO.2013.10.14.01(AA).

Ogunjobi, O., Sivakumar, V., Sivla, W.T., 2014b. A superposed epoch study of the effects of solar wind stream interface events on the upper mesospheric and lower thermospheric temperature. Advances in Space Research , in press,doi:10.1016/j.asr.2014.07.005.

Olasen, R.C., Shawhan, S., Galagher, D.L., Green, J.L., Chappell, C.R., Anderson, R.R., 1987. Plasma observations at the earth's magnetic equator. Journal of Geophysical Research 92, 2385–407.

Price, G., Jacka, F., 1991. The influence of geomagnetic activity on the upper mesosphere/lower thermosphere in the auroral zone. I. vertical winds,. Journal of Atmospheric and Solar-Terrestrial Physics 53, 909–922.

Pudovkin, M.I., 1996. Solar wind. Soros Educational Journal 12, 87–94.

Rapp, M., Lübken, F.J., 2004. Polar mesosphere summer echoes (PMSE): review of observations and current understanding. Atmospheric Chemistry and Physics Discussions 4, 4777–4876.

Rees, M.H., 1964. Note on the penetration of energetic electrons into the earth's atmosphere. Planet Space Science 12, 722.

Rees, M.H., 1989. Physics and chemistry of the upper atmosphere. Cambridge University Press, Cambridge.

Rees, M.H., Emery, B.A., Roble, R.G., Stamnes, K., 1983. Neutral and ion gas heating by auroral electron precipitation . Journal of Geophysical Research 88, 6289–6300. doi:10.1029/JA088iA08p06289.

Roble, R.G., 1995. Energetics of the mesosphere and thermosphere, in The Upper Mesosphere and Lower Thermosphere: A Review of Experiment and Theory. AGU, Washington D.C.. volume 87. pp. 1–21.

Roble, R.G., Dickinson, R.E., 1970. Atmospheric response to heating within a stable auroral red arc. Planet Space Science 18, 1489–1498.

Roeder, J., 1970. Dynamics of geomagnetically trapped radiation. New York, NY: Springer.

Rohrlich, F., Carlson, B.C., 1954. Positron-Electron Differences in Energy Loss and Multiple Scattering. Physical Review 93, 38–44. doi:10.1103/PhysRev.93.38.

Röttger, J., 1994. Polar mesosphere summer echoes: Dynamics and aeronomy of the mesosphere. Advances in Space Research 14, (9)123–(9)137.

Sinnhuber, M., Nieder, H., Wieters, N., 2012. Energetic Particle Precipitation and the Chemistry of the Mesosphere/Lower Thermosphere. Survey in Geophysics 33, 1281–1334. doi:10.1007/s10712-012-9201-3.

Sivjee, G., Shen, D., 1997. Auroral optical emissions during the solar magnetic cloud event of October 1995. Journal of Geophysical Research 102, 7431–7437.

Smiley, B., Robertson, S., Horányi, M., Blix, T., Rapp, M., Latteck, R., Gumbel, J., 2003. Measurement of negatively and positively charged particles inside PMSE during MIDAS SOLSTICE 2001 . volume 108. doi:10.1029/2002JD002425.

Smirnova, M., Belova, E., Kirkwood, S., Mitchell, N., 2010. Polar mesosphere summer echoes with ESRAD, Kiruna, Sweden: Variations and trends over 1997–2008. Journal of Atmospheric and Solar-Terrestrial Physics 72, 435–447. doi:10.1016/j.jastp.2009.12.014.

Stroud, W.G., Nordberg, W., Bandeen, W., Bartman, F.L., Titus, P., 1959. Rocket-grenade observation of atmospheric heating in the Arctic. Journal of Geophysical Research 64, 1342–1343.

Theon, J., Nordberg, W., Katchen, L., Horvath, J., 1967. Some observations on the thermal behavior of the mesosphere . Journal of Atmospheric Science 24, 428–438.

TheWathchers, 2013. Researchers discovered source of solar wind energy.

Thomas, G.E., Olivero, J., 2001. Noctilucent clouds as possible indicators of global change in the mesosphere. Advances in Space Research 28, 937–946.

Tsurutani, B.T., Lakhina, G.S., 1997. Some Basic Concepts of Wave-Particle Interactions in Collisionless Plasmas. Reviews of Geophysics 35, 491–502.

Van Allen, J.A., 1959. Radiation belts around the earth. Scientific American 200, 39.

Varotsou, A., Friedel, R., Reeves, G., Lavraud, B., Skoug, R., Cayton, T., Bourdarie, S., 2008. Characterization of relativistic electron flux rise times during the recovery phase of geomagnetic storms as measured by the NS41 GPS satellite. Journal of Atmospheric and Solar-Terrestrial Physics 70, 1745–1759.

Wang, Y.M., Ye, P.Z., Wang, S., 2003. Multiple magnetic clouds: Several examples during March – April 2001. Journal of Geophysical Research 108, 1370.

Yue, C., Zong, Q., Wang, Y., Vogiatzis, I.I., Pu, Z., Fu, S., Shi, Q., 2011. Inner magnetosphere plasma characteristics in response to interplanetary shock impacts. Journal of Geophysical Research 116, A11206. doi:10.1029/2011JA016736.

Zadorozhny, A.M., Kikhtenko, V.N., Kokin, G.A., Tuchkov, G.A., Tyutin, A.A., Chizhov, A.F., Shtirkov, O.V., 1994. Middle Atmosphere response to the solar proton events of October 1989 using the results of rocket measurements. Journal of Geophysical Research 99, 21,059–21,069.

Zhang, Y., Paxton, L.J., Kil, H., 2013. Multi-periodic auroral and thermospheric variations in 2006. Terrestrial, Atmospheric and Oceanic Sciences 24, 207–212. doi:10.3319/TAO.20.

Chapter 2

Data and model descriptions

In this study, both ground based data, satellite data and model computations are applied, in order to study the MLT temperature modifications in relation to the aforementioned events. The Super Dual Auroral Radar Network (SuperDARN) radar located at South African National Antarctica Expedition (SANAE) IV in Antarctica provide continuous detection of direct backscattered processes within the MLT range, useful in studying PMSE events in relation to mesospheric neutral temperature and wind. The radiometer Thermosphere Ionosphere Mesosphere Energetics and Dynamics/Sounding of the Atmosphere using Broadband Emission Radiometry (TIMED/SABER) satellite provides large measurements of temperatures, permitting us to consider possible temperature effects, statistically. The National Oceanic and Atmospheric Administration/Polar Orbiting Environmental Satellite (NOAA/POES) instruments and ground–based imaging riometer has been utilised to monitor the particle precipitation and absorption, respectively, during these events. Some other significant component of this study has been the use of a Monte Carlo Energy Transport Model (MCETM) in an actual atmospheric situations and those atmospheric situations estimated by simplified calculations. In this study, the MCETM is adopted as a basis for the expansion work, with the aim of modelling the deposition of energetic particles and the potential heating and cooling effects in the upper atmosphere during MC and SI events, employing the recent understanding of ion and neutral chemical processes.

The first part of this chapter outlines various instruments, useful in measurements of both ionospheric and neutral atmospheric quantities in relation to Geospace events. This is followed by the description of techniques, filtering and analysing of signals from a large data set, and model calculations in the context of this study.

2.1 Satellite observations

2.1.1 NOAA/POES satellite

National Oceanic and Atmospheric Administration/Polar Orbiting Environmental Satellites (NOAA/POES) is a polar-orbiting, Sun-synchronous, low-altitude (850 km) satellite with a duration of approximately 100 minutes. The POES has, onboard, the medium energy proton and electron detector (MEPED) and total energy detector (TED) that detects the magnitudes of the charged particle radiation at higher energies. Each group has a proton and an electron detector. At aurora latitudes the first group that looks, approximately, along the field lines, are known as the vertical sensor. There are four POES in orbit (see Figure 2.1) during the events under study. The satellites are labelled chronologically, based on the launch date. POES 15 was launched in May 1998, POES 16 was launched in September 2000, POES 17 was launched in 2002 and POES 18 was launched in 2005. The recently launched POES–N, does not cover for the period under study and is not included here. Two of the satellites cover the morning orbit while the other two cover the noon orbit. The satellites provide full global coverage for four times daily, which means multiple data points at any given location. Measurements from the four POES satellites can be combined, using interpolation techniques (Fang et al., 2007).

The POES pass over the poles, hence, they observe a wider range of L values. As noted above, the TED on each satellite provides measurements of proton and electron fluxes. Four detectors (two electron and two proton detectors) are mounted in two groups, where one group is viewing radially outward from the Earth and the other group viewing at 30°.

Similarly, the MEPED on each satellite gives directional (0° telescopes for precipitating and 90° for trapped) measurements of energetic particles. Even so, the electron channel have been found to be proton contaminated (Rodger et al., 2010). A first order correction might be a good scientific assertion in reducing proton contamination from MEPED (Lam et al., 2010). Details of the procedure used in implementing the first order correction are given in Appendix B.

In this study, first order correction,

$$\propto +15^{\circ} < \propto_{LC} \tag{2.1}$$

was employed. Here, $\propto$ and $\propto_{Lc}$ are the local particle pitch angle at the satellite and edge of the lost, cone respectively, and the opening angle of the detector is 15°. Assuming conservation of the first adiabatic invariant, the local pitch angle at the satellite, equivalent to the edge of the loss cone, was determined by

$$\propto_{Lc} = \sqrt{\frac{B_{sat}}{B_{120}}}. \tag{2.2}$$

Both the ambient magnetic field at the spacecraft B_{sat} and the ambient magnetic field at the foot of the field line which intersects $\sim$ 120 km above the Earth (B_{120}), are obtained from the International Geomagnetic Reference Field (IGRF) model. Furthermore, the counts from 0° telescope were inspected to ensure that counts in the $E > 100$ keV channel are less or equal to the counts in the $E > 30$ keV channels; since the precipitating electron counts, normally, decrease with increasing energy. With POES satellites, temporal variation can be obtained across all the magnetic local time. This is possible because at any given time, one of the POES satellites will offer coverage. Detailed information on POES satellite data can be obtained from Rodger et al. (2010). The POES measurements were employed in Chapters 3 and 4.

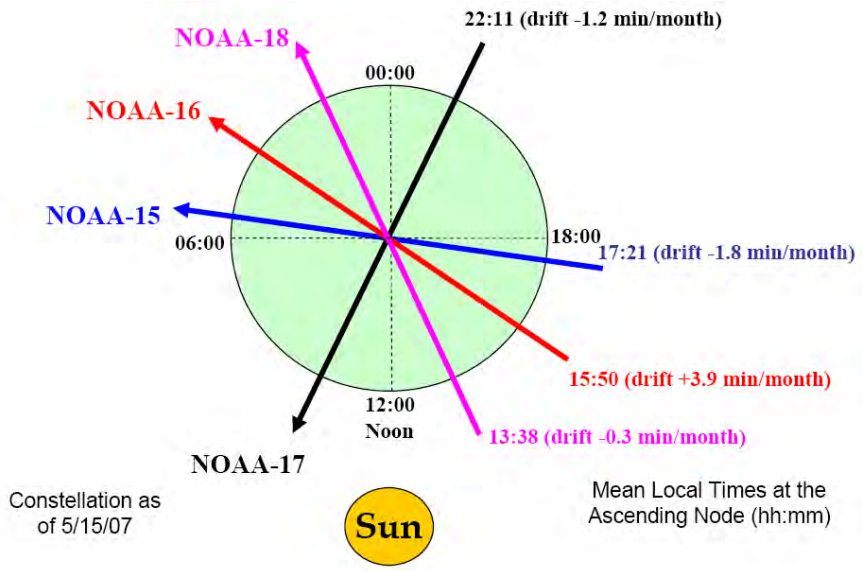

Figure 2.1: Schematic illustration of NOAA satellites passing the equator. Figure obtained from Chen-Po (2010).

2.1.2 TIMED/SABER satellite

The Thermosphere Ionosphere Mesosphere Energetic and Dynamics (TIMED) satellite was launched on 7 December 2001. It hovers in a nadir–pointing orientation of its 625 km circular polar orbit at 74.1° inclination and has a period of 102 minutes. By step scanning the atmosphere limb, SABER (Sounding of the Atmosphere using Broadband Emission Radiometry), which is one of the four instruments on–board the TIMED satellite (see Figure 2.2), measures the height profile of neutral temperature. In this study, the vertical temperature profiles in relation to SI and PMSE events were retrieved. SABER is measuring CO_2 15μm limb emission, which can be used to estimate the neutral temperatures up to, approximately, 130 km. In order to maintain a certain temperature in the instrument, SABER obtains profiles from 83°S to 52°N during its south–looking mode and at every 60 days the look direction switches to an analogous North–looking mode. In this study, temperature measurements were obtained when SABER was at its south–looking mode. TIMED/SABER has been found to be useful and contributes toward validation of assimilative atmospheric models, such as the International Reference Ionosphere (IRI) (Bilitza et al., 2014). Measurements from TIMED/SABER satellite were used in Chapters 4 and 5.

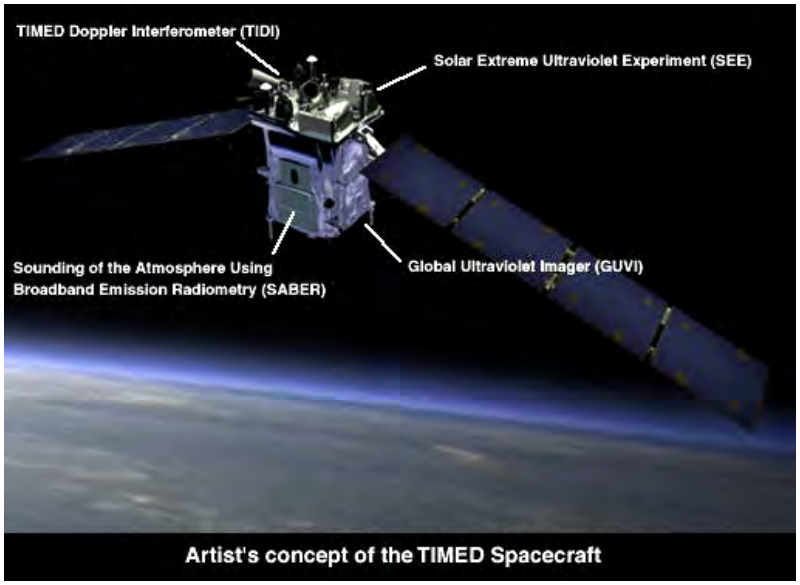

Figure 2.2: Artistic illustration of TIMED satellite. The four instruments onboard include SABER, Global ultraviolet imager (GUVI), Timed doppler interferometer (TIDI) and Solar extreme ultraviolet experiment (SEE). Figure adopted from EoPortal (2013b).

2.1.3 CHAMP satellite

Mesospheric and thermospheric neutral winds can be measured by satellite–carried instruments, such as CHAMP (Challenging Mini–Satellite Payload). The CHAMP was launched in a near polar orbit in July 2000. CHAMP is in a near–circular, polar orbit (87.30° inclinations) with a precession rate of ∼1.50 hr per day; it gives coverage of all local times and latitudes every 130 days (Liu et al., 2006). With 15 orbits per day, the CHAMP satellite passes any mid–latitude band 15 times during its upward motion and 15 times during its downward motion. CHAMP provides pole–to–pole latitudinal coverage. The coverage takes place at different longitudes, due to the Earth's revolution. From its initial altitude at 456 km, the CHAMP orbit depreciated to approximately 350 km during the first five years of operation. In this study, CHAMP has been used to study thermospheric neutral winds. Although CHAMP is not, specifically, meant for thermospheric wind studies, information of the accelerometer on board has been treated, in order to engender cross–track wind speeds and neutral density. Figure 2.3 shows the position of the accelerometer inside the spacecraft at the center of mass. With definitive and continuous measurements from the accelerometer, it has been possible to generate wind and density data from the non–gravitational accelerations (Liu et al., 2006; Sutton et al., 2007; Doornbos et al., 2010). The iterative algorithm, developed by Doornbos et al. (2010), has proved extremely useful in extracting the neutral wind data from CHAMP measurements, which works independently of the orientation of the instrument in space.

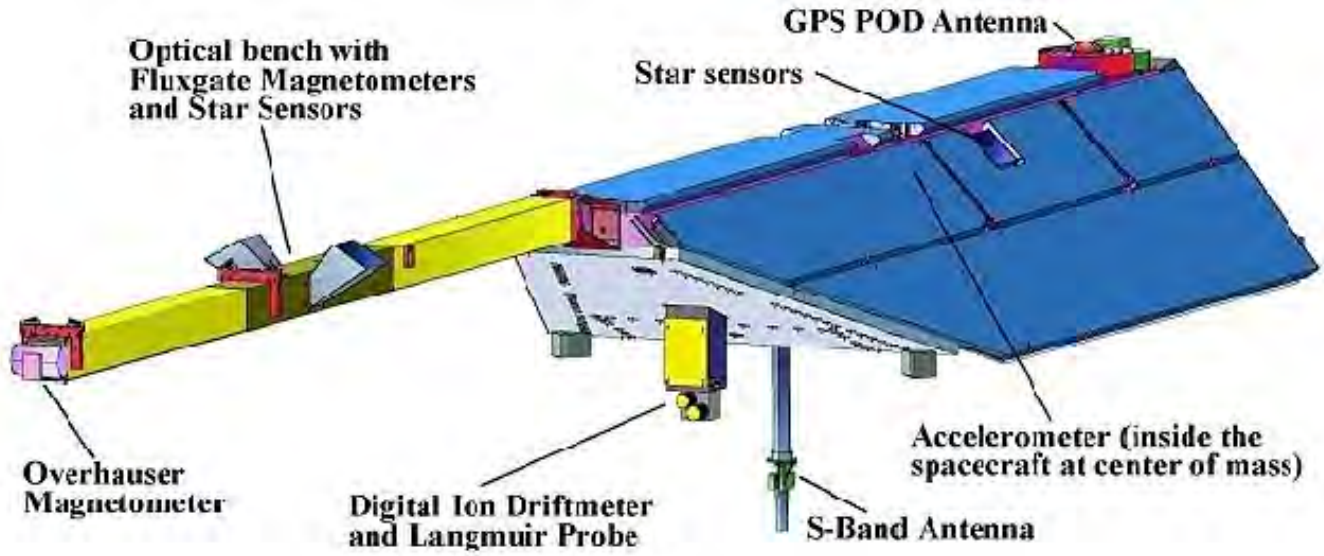

Figure 2.3: Structural (Front) view of the CHAMP satellite. Figure obtained from EoPortal (2013a).

2.1.4 OMNIWeb data

The OMNIWeb (see, King and Papitashvili, 2005) data sets comprises of measurements of near–Earth solar wind, magnetic field and, plasma parameters. To better understand the solar wind–magnetosphere coupling, a time–shifted magnetic field and plasma data from their location of observation, which may be at some hour upstream of the magnetosphere, to a point nearer is needed (Farris and Russell, 1994; King and Papitashvili, 2005). The OMNIWeb data sets have been time–shifted closer to the Earth's bow shock nose, which is at a distance of approximately 15–17 R_E from the Earth. The basic principle of the time–shifting is the use of the phase front normal (PFN) directions, which are determined individually for each input of magnetic field observation and its near neighbours. The bow shock location, to which the data are shifted, is included in the OMNIWeb output data for several geophysical parameters. The Assumption upon which the time–shifting is based is that, solar wind and magnetic field values at a specific time and location lie on a planar surface. Some of the important spacecrafts that are providing data, which are being timed–shifted, include an advanced composition explorer (ACE), Wind, IMP 8, and Geotail spacecraft, which are part of the international solar–terrestrial physics (ISTP) project.

From close to 51 different parameters available at OMNIWeb, only those that are relevant to this study were obtained. Among the parameters used in this study, are the Interplanetary Magnetic Field (IMF) B_z, proton number density (n_{sw}), solar wind azimuthal velocity (GSE–V_y), solarwind radial velocity (GSE–V_x), solar wind pressure (nPa) and Alfvén Mach number (M_A). The speed with which plasma waves can propagate is called the Alfvén speed. The typical Alfvén speed is usually 40 km/s. In a case of HSSW moving at supersonic speed of 400 km/s, the Alfvén speed in it is 10 times as large; known as the M_A. Notwithstanding, the solar wind parameters are geomagnetic activity proxies. These include, quasi–logarithmic index (Kp index), Disturb storm time (Dst) indices and the solar flux proxy, F10.7 index. The Kp index and Dst indices have contributed to OMNIWeb data sets from different magnetometer stations across the globe. The OMNI measurements were employed in Chapters 3, 4, 5 and

6.

2.2 Ground–based observations

2.2.1 SuperDARN radar

Data from the Super Dual Auroral Radar Network (SuperDARN) SANAE IV radar (71.68°S, 2.85°W) are employed in this study. The radar uses the frequency band between 8 and 20 MHz (Greenwald et al., 1995). The antenna array consists of 16 antennae, which are operated as a phased array having 170° bore–site (Figure 2.4). SANAE IV radar is technically and operationally similar to 31 other SuperDARN radars located in both the Northern and Southern hemispheres (Figure 2.5). The SuperDARN radars at different locations use the same scanning parameters for 50% of the entire instrument operational time (Greenwald et al., 1995; Hosokawa et al., 2005). In common time operation, the SuperDARN radar beam is, sequentially, scanned from beam 0 to beam 15 across its 75 range gates, with a step in azimuth of 3.33°, a scan repeat time at every 2 minutes, a range resolution of 45 km, and a peak power of about 10 kW. The beams are made to have maximum sensitivity at elevation angles of 15°–35°, to allow backscatter echo detection. The return echoes for each beam are integrated over 7 s. The field of view (FOV) of SANAE IV radar in geographic and geomagnetic coordinates is presented in Figure 2.6. The FOV shows that the SuperDARN SANAE IV radar is located at the sub–auroral oval zone, suitable for observations of HF backscatters within the Antarctic region. The direct backscatter processes, such as the meteor trails, sporadic E region backscatter echoes and PMSE, fall into the category of coherent backscatters. The oblique sounding technique of SuperDARN is such that, it can detect these backscatters, simultaneously, within the near range gates.

The backscatter delays at the nearest range gate (0 gate) is set to 1200 μs pulse length, which is equivalent to 180 km. The subsequent pulse length is set to 300 μs, equivalent to a gate length of 45 km. Backscatter information from these pulses are sampled and then processed, giving multi–lag–auto–correlation functions (ACFs). Details on how the ACF

is calculated can be found in Walker (2002). The ACFs are, thereafter, used to deduce backscatter power, mean Doppler velocity and the width of the Doppler power spectrum for each range with significant returns. The pulse sequence is about 40 ms in duration, and pulse sequences are separated by periods of 60 ms, resulting in 60 ACF in each 7 transmitting seconds, which are averaged for each measurements. Figure 2.7, for instance, illustrates the backscatter power, mean Doppler velocity and the spectral width from beam number twelve on 21 December 2005, as detected by the SuperDARN SANAE IV radar.

The SuperDARN radars are optimum instruments used, primarily, to monitor the plasma convection pattern in the high–latitude–ionosphere. However, it has contributed greatly to the understanding of the dynamics of the MLT region. At mesospheric altitude, the backscatter comes from the electron density fluctuations and shows a sensitive dependence on the frequency. SuperDARN observation of meteor trails at 94 km is associated with drift in neutral wind velocities which is useful in studying the trends of meridional and zonal circulations. Although SuperDARN radar, as previously described, is not specifically planned for wind observation, but it could also be used to track neutral wind variation at mesopause altitude, since meteors can only be found within this region. A detailed description of tracking neutral winds using SuperDARN radar can be found elsewhere (Hussey et al., 2000). It should be noted, however, that winds are altitude dependent and, thus, meteor radar observation of neutral winds can only be relative and not highly accurate (Yukimatu and Tsutumi, 2002, 2003). Recent updates on SuperDARN operations can also be found in Lester (2013). As mentioned in the previous chapter, the mesospheric energy budget is difficult to analyse, since jet planes and hydrogen–filled balloons cannot hover high enough to fully cover this region. However, rockets can access this region, providing intermittent and costly in–situ measurements. In this situation, continuous remote sensing via ground–based instruments, such as SuperDARN radar, play an important role in mesospheric studies. Measurements from SuperDARN SANAE IV radar are further discussed in Chapter 5.

Figure 2.4: Pictorial view of SuperDAN SANAE IV radar antenna. Photo taken on 25 January 2010 by Ogunjobi Olakunle (UKZN/HMO Amingo, 2010 take over Antarctic expedition).

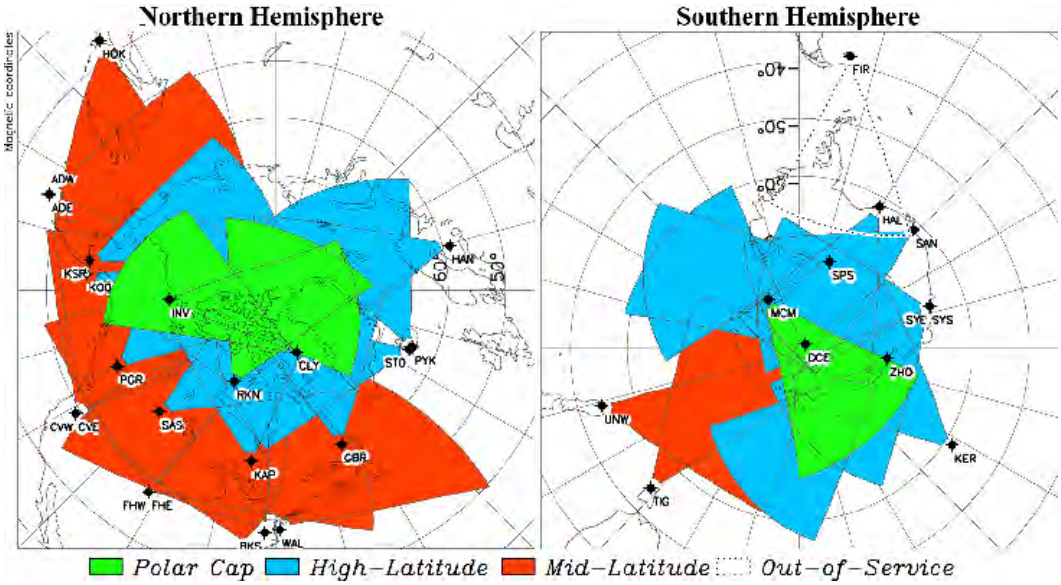

Figure 2.5: Magnetic coordinates of SuperDARN radars showing all field of view in Northern (Left panel) and Southern (Right panel) Hemispheres. Figure obtained from VirginiaTech (2014).

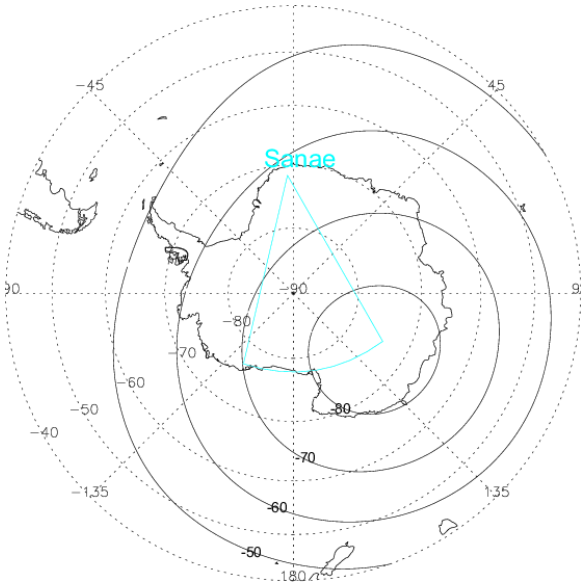

Figure 2.6: Map showing the SANAE radar fields of view (blue line) projected on a geographic (dash lines) and geomagnetic (solid lines) coordinates. Figure replotted in Chapter 5.

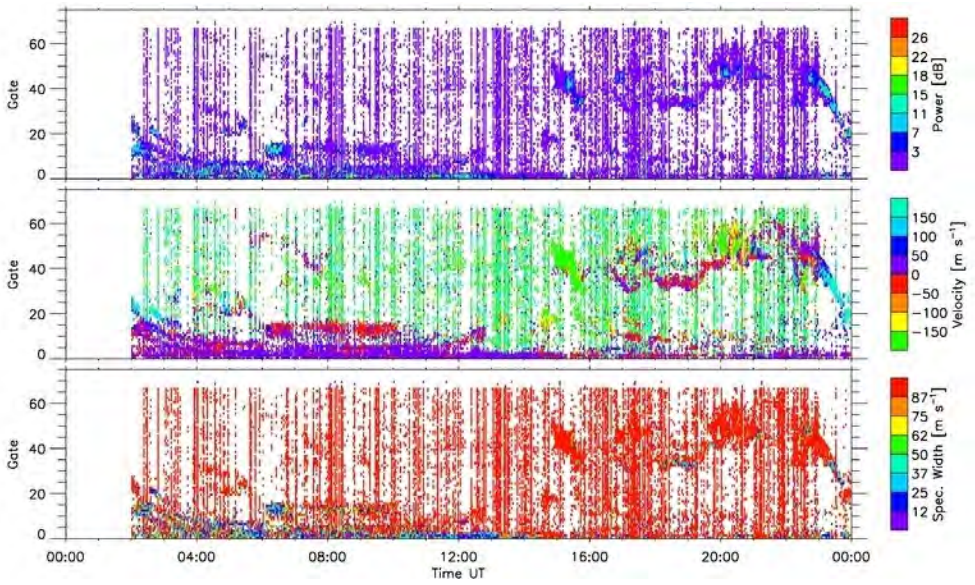

Figure 2.7: SuperDARN SANAE IV scatter plot of backscatter power, spectral width and Doppler velocity on beam 12 from 00:00 hr UT to 23:00 hr UT on 21 December 2005. Figure adopted from Figure obtained from VirginiaTech (2014).

2.2.2 Riometer

Remote sensing (RS) of electromagnetic waves of cosmic origin is a technique used to study the state and structure of the ionosphere (Hargreaves, 1979). Riometers provide RS means of detecting magnetospheric particle precipitation into the ionosphere. Riometers respond to the integrated absorption of cosmic ray noise through the ionosphere (see, Clilverd et al., 2010) at heights where the electron motion is collision dominated. When a radio wave passes through the ionosphere, it causes charged particles to vibrate with a frequency ν. If these charged particles collide with heavier neutrals, then energy is lost, which results in a loss of energy from the radio wave. The rate of absorption depends on the number of collisions ($\sim \nu$) per wave oscillation, or on ν/ω. The absorption encountered by a radio wave passing through the ionosphere is, usually, expressed in decibels (dB) and is derived from the expression:

$$A(dB) = 10log(\frac{P}{P0}) \tag{2.3}$$

Where $P0$ is the non–attenuated cosmic noise power (CNP), and P is the CNP attenuated by atmospheric absorption. Both the $P0$ and P are measured at the same sidereal time (that is, the same view angle, with respect to the sky).

Riometers are mostly widebeam, typically 30 MHz, and sensitive to any incident particle population capable of reaching the ionosphere in the range of 70–100 km, empirically determined to be greater than 30 keV electrons or Mev protons (Clilverd et al., 2010). Generally, riometers cannot resolve the individual particle populations detected, but the use of the presence (or absence) of riometer absorption during an event is employed as a robust indicator of precipitation of high energy electrons (Morley et al., 2010).

The amount of the background cosmic radio noise disrupting the ionosphere is known to be a constant for a particular location and given (sidereal) time of day. In order to identify extraordinary absorption, a reference of Quiet Day Curve (QDC) is an important parameter to be considered. Any deviations from this expected value must then be due to absorption in the ionosphere. Having a QDC in place, the absorption at any particular

time was determined by subtracting the QDC from the measured attenuation. The basic assumption in establishing the QDC is that, for any given sidereal time, there is a certain part of the year in which the absorption becomes negligible. Consequently, the QDC is, usually, produced from a plot of individual readings of the output level as a function of sidereal time, for a period during which there is no changes in the equipment parameters. An example of QDC absorption intensity is shown in Figure 2.8. Absorption peaks at all Finnish riometers were between 7–10 UT on 10 January 1997. Any significant correlations between these ionospheric absorption peaks and the particle precipitation are a good indicator of likely effects on mesopause. The systematic approach towards constructing a QDC for SANAE IV riometer has been documented by Wilson (2000), and Wilson and Stoker (2002). The riometer measurements were also employed in Chapters 3, 4 and 5.

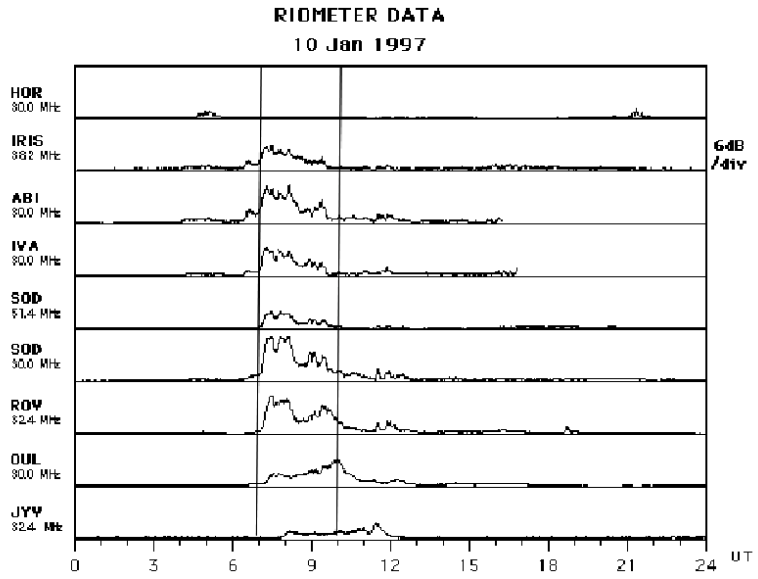

Figure 2.8: A typical sample of riometer absorption from Finish chain of riometers.

2.3 Model and techniques

2.3.1 SEA techniques

One method for composition of time series data is the Superposed Epoch Analysis (SEA) technique. This technique is applied, in order to reveal consistent responses, relative to some repeatable phenomenon, in noisy data (Chree, 1908). It allows separation of data into categories (key events) and comparing means for different categories. The technique is such that, data are averaged in relation to the key event. The consistent event signal will remain and the random influences will tend to average out. However, SEA makes no assumption of linearity, and its use in this study is justified as a good technique at separating signals from noise from a large data set. The reference time as zero time of SEA allows one to examine the onset of interplanetary sources and the initial part of the event.

Because of the recurrence nature of SI as a storm driver, it is particularly amenable to SEA. The choice of reference (zero) time for SEA is important and substantially influences the results (Borovsky and Denton, 2009; Morley et al., 2010). In this study, time series of the variables under investigation are extracted from a window around the epoch and all data at a given time, relative to the given epoch, form the sample of events at that lag. The data at each time lag are then averaged so that inconsistent fluctuations about the epoch will cancel. For instance, the SI onset is determined by the deflection of solar wind azimuthal velocity (that is, reversal of GSE–V_y), as shown in Figure 2.9. The negative days are days prior to the arrival of SI, the zero day is the onset of the event and the positive days are for after the event.

It is very important to have some believable hypotheses for why the event should affect the SEA variables, otherwise, there will be a risk of finding a statistical coincidence with no physical connotation. Thus, a statistical significant test was performed by determining the probability that the signal obtained from the SEA arose by chance using the first and third quartiles.

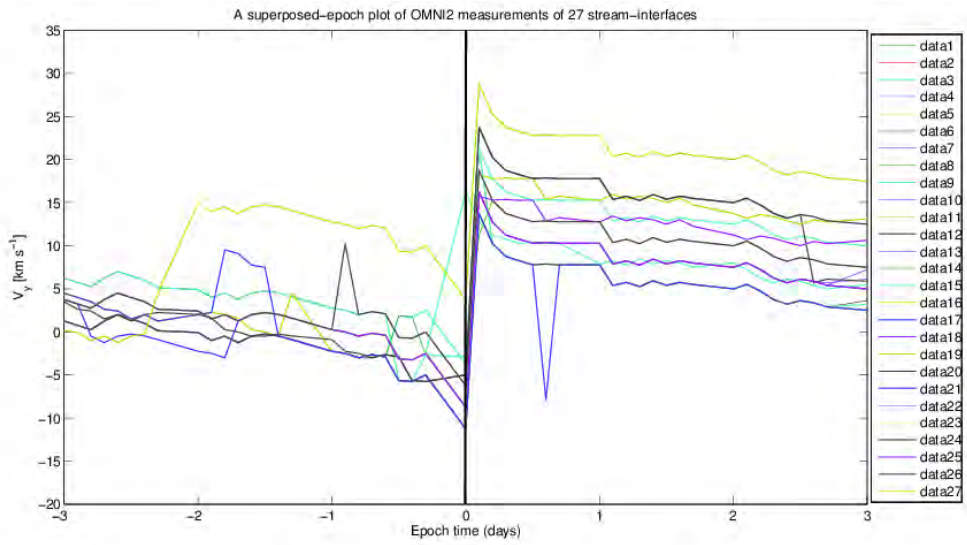

Figure 2.9: SEA of solar wind azimuthal velocity, V_y–GSE coordinate depicting the onset of SI events. The traces for many of the 27 events are overlaid by the other events; hence only a smaller number of traces are visible. Figure adopted from Ogunjobi et al. (2014).

2.3.2 MCETM calculations

Based on Berger et al. (1970), the energy deposition by the energetic particles can be calculated using the Monte Carlo method, herein, referred to as Monte Carlo Energy Transport Model (MCETM):

$$s_{mb} = \frac{z_m(h_b) - z_{m.n}}{Cos\theta_n}; \tag{2.4}$$

where,

$$z_m(h_b) = \int_h^{h_o} D(h_b')dh'$$

is the atmospheric depth, used as an input for the model with $D(h_b')$ as the density, supposing that the electron passes through a particular 'scoring boundary 'h_b between the $n'th$ and $n+1'$ st collisions, and $z_m(h_b)$ being the mass thickness at each corresponding height. The distance, s_m, travelled by electrons within the boundary b is given as:

$$s_m = \int_{E_{n+1}}^{E_n} \frac{dE}{L(E)} = r_o(E_n) - r_o(E_{n+1)} \tag{2.5}$$

which is obtained by interpolating the atmospheric mean range, r_o against acquired electrons' energy E, using stopping power L. The pathlength from the $n'th$ collision point to the boundary results to s_{mb} as given in Equation 2.4. Details of MCETM calculations are given in Appendix C.

Berger et al. (1970) noted the applicability of this program to problems in actually observed atmospheric phenomena and those predicted by the simplified calculations. In this case, rather than theoretical assumption of characteristic energy, the electron ($>$ 30 keV, $>$ 100 keV and $>$ 300 keV) energies from the MEPED detector was first combined into energy ranges of 30–100 keV and 100–300 keV, these integral fluxes are then combined with those retrieved from TED in the ranges of 2116–3075 eV and 6503–9167 eV, in order to obtain differential fluxes. That is, the four differential energy channels are fitted into a double exponential spectrum:

$$j(E) = A_1.e^{-\frac{E}{E_1}} + A_2.e^{-\frac{E}{E_2}}. \tag{2.6}$$

The characteristic energies, E_1 and E_2, and the factors A_1 and A_2, are then determined. At every pathlength, one can obtain energy deposited at various heights of interest per time. Similar to Rees (1989), the energy expended by the primary precipitation for each ion-electron pair production is taken to be 35 eV.

Maehlum (1973) provided a three exponential technique, useful for obtaining information about the deposition of proton energy as a function of altitude:

$$\frac{dE}{dz} = 236E^{-0.78}, \tag{2.7}$$

given that the energy loss, $\frac{dE}{dz}$, is in $MeVcm^2g^{-1}$ units. By using three exponential functions, one can obtain the spectra used in MCETM for proton energy deposition. Both electrons and protons are vertically incident. In all, the aforementioned atmospheric composition and densities are estimated, based on the Mass Spectrometer Incoherent Scatter Extended (MSIS) model, of which, details have been provided by Hedin (1991). The MCETM calculations

were used in Chapters 3 and 4.

2.3.3 Electron number density model calculations

Electron number density from an absorption of radio waves by the ionosphere was, usually, calculated using the Appleton–Hartree magnetoionic theory (Majumdar, 1972). Using classical equations (Hargreaves, 1992) and approximations (Wang et al., 1994), the expression for the absorption $A(dB)$ was reduced to the following formula:

$$A(dB) = \frac{4.58 \times 10^{-5}}{\omega^2} \int N_e(h)\nu(h)ds \tag{2.8}$$

where $N_e(h)$ gives the electron number density at any height h, $\nu(h)$ which is $\sim \rho(h)$ (Hargreaves and Friedrich, 2003) and obtained as the property of the atmosphere (i.e. proportional to pressure, $\rho(h)$), ω is the radio wave angular frequency, and ds is the path element. The electron number density calculations were used in Chapter 3.

References

Berger, M.J., Seltzer, S.M., Maeda, K., 1970. Energy deposition by auroral electrons in the atmosphere. Journal of Atmospheric and Terrestrial Physics 32, 1015–1045.

Bilitza, D., Altadill, D., Zhang, Y., et al., 2014. The International Reference Ionosphere 2012–a model of international collaboration . Journal of Space Weather and Space Climaate 4, A07. doi:10.1051/swsc.

Borovsky, J.E., Denton, M.H., 2009. Relativistic-electron dropouts and recovery: a superposed epoch study of the magnetosphere and the solar wind. Journal of Geophysical Research 114, A02201. doi:10.1029/2008JA013128.

Chen-Po, K., 2010. Investigation of the Equatorial F-region Ionospheric Irregularities using COSMIC/FORMOSAT-3. Ph.D. thesis. Institute of Space Science, National Central University, Taiwan.

Chree, C., 1908. Magnetic declination at Kew Observatory, 1890-1900. Philosophical Transactions of the Royal Society of London A, 205–246. doi:10.1098/rsta.1908.0018.

Clilverd, M.A., Rodger, C.J., Gamble, R.J., Ulich, T., Raita, A., Seppälä, A., Green, J.C., Thomson, N.R., Sauvaud, J.A., Parrot, M., 2010. Ground-based estimates of outer radiation belt energetic electron precipitation fluxes into the atmosphere. Journal of Geophysical Research 115, A12304. doi:10.1029/2010JA015638.

Doornbos, E., Van den Ijssel, J., Lühr, H., Forster, M., Koppenwallner, G., 2010. Neutral

density and crosswind determination from arbitrarily oriented multi-axis accelerometers on satellites. Journal of Spacecraft and Rockets 47, 580–589.

EoPortal, 2013a. CHAMP (Challenging Minipayload Satellite) URL: https://directory.eoportal.org.

EoPortal, 2013b. TIMED (Thermosphere, Ionosphere, Mesosphere, Energetics and Dynamics). URL: https://directory.eportal.org.

Fang, X., Liemohn, M.W., Kozyra, J.U., Evans, D.S., DeJong, A.D., Emery, B.A., 2007. Global 30-240 keV proton precipitation in the 17-18 April 2002 geomagnetic storms: 1. Patterns. Journal of Geophysical Research 112, A05301.

Farris, M., Russell, C.T., 1994. Determining the standoff distance of the bow shock: Mach number dependence and use of models. Journal of Geophysical Research 99, 17681–17689.

Greenwald, R.A., Baker, K.B., Dudeney, J.R., Pinnock, M., Jones, T.B., Thomas, E.C., Villain, J.P., Cerister, J., Senior, C., Hanuise, C., et al., 1995. DARN/SuperDARN. Space Science Review 71, 761–796.

Hargreaves, J.K., 1979. The Upper Atmosphere and SolarTerrestrial Relations. Van Nostrand Reinhold, New York .

Hargreaves, J.K., 1992. The solar-terrestrial environment. Cambridge Atmospheric and Space Science Series, Cambridge University Press, Cambridge, UK.

Hargreaves, J.K., Friedrich, M., 2003. The estimation of D-region electron densities from riometer data. Annales Geophysicae 21, 603.

Hedin, A.E., 1991. Extension of the MSIS thermosphere model into the middle and lower atmosphere. Journal of Geophysical Research 96, 1159–1172. doi:10.1029/90JA02125.

Hosokawa, K.T., Ogawa, N.F., Arnold, M., Lester, N.S., and, A.S.Y., 2005. Extraction of polar mesosphere summer echoes from SuperDARN data. Geophysical Research Letters 32, L12801. doi:10.1029/2005GL022788.

Hussey, G.C., Meek, C.E., André, D., Manson, A.H., Sofko, G.J., 2000. A comparison of Northern Hemisphere winds using SuperDARN meteor trail and MF radar wind measurement . Journal of Geophysical Research 105, 18053–18066. doi:10.1029/2000JD900272.

King, J., Papitashvili, N., 2005. Solar wind spatial scales in and comparisons of hourly Wind and ACE plasma and Magnetic field data. Journal of Geophysical Research 110, A02209. doi:10.1029/2004JA010804.

Lam, M.M., Horne, R.B., Meredith, N.P., Glauert, S., Moffat-Griffin, T., Green, J.C., 2010. Origin of energetic electron precipitation >30 keV into the atmosphere. Journal of Geophysical Research 115, A00F08. doi:10.1029/2009JA014619.

Lester, M., 2013. The Super Dual Auroral Radar Network (SuperDARN): An overview of its development and science. Advances in polar science 24, 1–11. doi:10.3724/SP.J.1085.2013.00001.

Liu, H., Lühr, H., Watanabe, S., Kohler, W., Henize, V., Viseer, P., 2006. Zonal Winds in the equatorial upper atmosphere. Journal of Geophysical Research III, A07307. doi:10.1029/2005.

Maehlum, B.N., 1973. Particle precipitation: Scattering and absorption. in Cosmical Geophysics, Universitetsforlaget. pp. 211–219.

Majumdar, R.C., 1972. Generalization of Appleton-Hartree equation of theories of collision frequency. Indian Journal of Radio and Space Physics 1, 31–37.

Morley, S.K., Friedel, R.H.W., Spanswick, E.L., Reeves, G.D., Steinberg, J.T., Koller, J., Cayton, T., Noveroske, E., 2010. Dropouts of the outer electron radiation belt in response to solar wind stream interfaces: global positioning system observations. Proceedings of Royal Society 466, 3329–3350.

Ogunjobi, O., Sivakumar, V., Sivla, W.T., 2014. A superposed epoch study of the effects of solar wind stream interface events on the upper mesospheric and lower thermospheric temperature. Advances in Space Research , in press,doi:10.1016/j.asr.2014.07.005.

Rees, M.H., 1989. Physics and chemistry of the upper atmosphere. Cambridge University Press, Cambridge.

Rodger, C.J., Clilverd, M.A., Green, J.C., Lam, M.M., 2010. Use of POES SEM-2 observations to examine radiation belt dynamics and energetic electron precipitation into the atmosphere. Journal of Geophysical Research 115, A04202. doi:10.1029/2008JA014023.

Sutton, E.K., Nerem, R.S., Forbes, J.M., 2007. Atmospheric density and wind measurements deduced from accelerometer data. Journal of Spacecraft and Rockets 44. doi:10.2514/1.28641.

VirginiaTech, 2014. SuperDarN URL: http://www.vt.superdarn.org.

Walker, A., 2002. The SHARE Radar at SANAE, Antarctica. South African Journal of Science 98, 257–268.

Wang, Z., Rosenberg, T.J., Stauning, P., Basu, S., Crowley, G., 1994. Calculations of riometer absorption associated with F region plasma structures based on Sondre Stromfjord incoherent scatter radar observations. Radio Science 29, 209–215.

Wilson, A., 2000. Imaging riometer observations on energetic electron precipitation at SANAE IV, Antarctica. Ph.D. thesis. Potchefsroomse Universiteit vir Christelike Hoër Onderwys.

Wilson, A., Stoker, P., 2002. Imaging riometer observations on energetic electron precipitation at SANAE IV, Antarctica. Journal of Geophysical Research 107, 1268.

Yukimatu, A.S., Tsutumi, M., 2002. A superDARN meteor wind measurement: Raw time series analysis method and its application to mesopause region dynamics. Geophysical Research Letters 29, 1981. doi:10.1029/2002GL01510.

Yukimatu, A.S., Tsutumi, M., 2003. Correction to "A new SuperDARN meteor wind measurement: Raw time series analysis method and its application to mesopause region dynamics" by Akira Sessai Yukimatu and Masaki Tsutsumi. Geophysical Research Letters 30, 1026. doi:10.1029/2002GL016560.

Chapter 3

A case study of energy deposition and absorption by magnetic cloud electrons and protons over the high latitude stations: effects on the mesosphere and lower thermosphere*

* This chapter needs to be cited as:

Ogunjobi, O., V. Sivakumar and N. Mbatha. A case study of energy deposition and absorption by magnetic cloud electrons and protons over the high latitude stations: Effects on the mesosphere and lower thermosphere. *Terrestrial, Atmospheric and Oceanic Sciences,* 25, 219-232 (2014), doi: 10.3319/TAO.2013.10.14.01(AA).

Terr. Atmos. Ocean. Sci., Vol. 25, No. 2, 219-232, April 2014 doi: 10.3319/TAO.2013.10.14.01(AA)

A Case Study of Energy Deposition and Absorption by Magnetic Cloud Electrons and Protons over the High Latitude Stations: Effects on the Mesosphere and Lower Thermosphere

Olakunle Ogunjobi *, Venkataraman Sivakumar, and Nkanyiso Mbatha

School of Chemistry and Physics, University of KwaZulu-Natal, Durban, South Africa

Received 15 March 2013, accepted 14 October 2013

ABSTRACT

Several possible characteristics of magnetic clouds (MCs) have been discussed in the literature, but none appears to explain all the effects from accumulated observations. MC characteristics range from low proton temperature and plasma beta, to high magnetic field magnitude, to smooth rotation in the direction of the magnetic field thus resulting in strong geomagnetic disturbances. Varied instrumentation which is located not only in SANAE IV, Antarctica, but also at Halley, a same radial distance ($L \sim 4$) in the southern hemisphere and in the vicinity of a conjugate location in northern hemisphere provide an opportunity to test theories applied to high latitude heating rates on the arrival of MC. The Halley riometer is used to monitor coincidences of absorption with the arrival of MC which was observed on 8 November 2004. Using the Monte Carlo Energy Transport Model (MCETM), the corresponding altitude of electron and proton energy distribution indicates the importance of MC triggered geomagnetic storms on mesosphere dynamics.

Key words: Magnetic Cloud, Precipitation, MLT region, Absorption, Energy deposition, *L* shell

Citation: Ogunjobi, O., V. Sivakumar, and N. Mbatha, 2014: A case study of energy deposition and absorption by magnetic cloud electrons and protons over the high latitude stations: Effects on the mesosphere and lower thermosphere. Terr. Atmos. Ocean. Sci., 25, 219-232, doi: 10.3319/TAO.2013.10.14.01(AA)

1. INTRODUCTION

Solar wind is responsible for fueling magnetospheric storms, forming the Earth's magnetosphere. Energetic particles and momentum from the solar wind are consequently conveyed in form of energy to the terrestrial atmosphere via particle precipitation or as electromagnetic radiation. The region of the mesosphere (50 - 100 km) and lower thermosphere (100 - 180 km) is not fully understood when considering the overall energy budget in the Earth's atmosphere. The complication in understanding the energy budget ranges from the hemispherical differences to the large number of external and internal processes that are able to heat the atmosphere and as well cool it, depending on the specific effective conditions present (Roble 1995). However, for several decades, one of the controversial problems in solar-terrestrial physics has been the impact of solar activities on atmospheric energetics and dynamics (Georgieva et al. 2005). Several geophysical parameters are often used to gauge the impact of solar-terrestrial disturbances on the Earth's atmosphere (Zhang et al. 2006). Despite the present coordinated solar and geophysical parameters and meterological indices, it has been noted that the two solar hemispheres affect the Earth in a number of ways.

A major source of enhanced ionisation in the ionosphere is as a result of precipitating energetic particles depositing their energy in the upper atmosphere during geomagnetic disturbances, e.g., Estep et al. (1999). Particles, especially, electrons which usually have small mass, can be scattered through very large angles when they collide with neutrals in the atmosphere. If the resulting deviations decrease the pitch angle, it will backscatter and penetrate more on the other end of its bounce trajectory. On the other hand, if the deviations increase the pitch angle, it can lead to further penetration into the atmosphere causing loss of more energy by collisions. The presence of avalanche particles triggered by precipitation will increase atmospheric energy and ultimately influence the composition of the atmosphere through ionisation, dissociation and excitation. Also, the helicity of the magnetic structure in the plasma of solar wind flow

* *Corresponding author*
E-mail: olakunle.ukzn@gmail.com

governed by the electric field, together with the presence of resulting temperature gradients change neutral winds. Such perturbation induces chemical heating rates and infrared cooling. Precipitating particles produce forms of odd nitrogen (NO_x) and odd Hydrogen (HO_x) (Swider and Kenesha 1973; Rusch et al. 1981; Solomon et al. 1981; Sætre et al. 2004; Rodger et al. 2010b; Kang et al. 2012) which undergo a series of chemical reactions. Although minor gases, if they enter the uppermost layer of the stratosphere and troposphere, they contribute to the overall processes that catalytically deplete ozone (Grenfell et al. 2006) and partly affect the radiation budget of the polar atmosphere.

It has been noted recently that the helicity of magnetic structure is the most prominent feature of solar activity which determines the effectiveness of geomagnetic disturbances in both the southern and northern hemispheres (Antonucci et al. 1990). Scientific understanding of this feature requires an event based study, in particular, interplanetary coronal mass ejections (ICMEs) events. Burlaga et al. (1982) had earlier found that the strongest geomagnetic disturbances are predominant when the Earth encountered magnetic clouds (MCs) associated with ICMEs. A MC is a transient ejection in the solar wind defined by relatively strong fields, a smooth rotation of the magnetic field direction over about 0.25 and 1 AU, a low proton temperature and a low plasma pressure to magnetic pressure ratio (Burlaga 1988). MC is further characterised by Lepping et al. (1990) as the region between the leading half of the z-component of southward interplanetary magnetic field (IMF-Bz) and the trailing half which contains a strong northward peak, or vice versa, with an accompanying large density enhancement which strongly compressed the magnetosphere. These interplanetary properties have been found to be triggers of geomagnetic storms (Lepping et al. 1997).

The interactions of the precipitating energetic particles, associated with the storms, with increasingly denser atmospheric neutrals, such as hydrogen and nitrogen, in the MLT altitude ranges can produce the emissions which characterise the auroras. The difference between the normal and MC induced auroras has been investigated in the Northern high latitude by Hviuzova and Leontyev (1997, 2001). Based on the aurora observation data at the Loparskaya Observatory during 1970 - 1985, the yearly means of the of auroral intensity ratio were obtained. They showed that during MC-aurora there was an enhanced mean ratio between the red auroral emission (6300Å) and the green emission (5577Å), with the spectrum of precipitating electrons being shifted to the higher energies during the MC aurora type. This implies that the intensity and efficiency of energy deposition by MC are strongly altitude dependent. Similarly, the work of Sivjee and Shen (1997) examined the auroral emissions during the solar MC on October 18, 1995. Using continuous spectroscopic measurements, it was shown that there is a difference between the normal auroras and the MC induced auroras. Despite the possible ability of compressed MCs to cause many large geomagnetic storms (Wang et al. 2003), there has been little significant attention as to its effects on the MLT energy budget. It should be noted, Georgieva et al. (2005) showed the probable impact of MC on the middle atmosphere based on the geo-effectiveness of the MC and phases of the quasibiennial (QBO) oscillation of equatorial stratospheric winds. The general effects were found to be strongest for south-north oriented clouds in the QBO easterly phase. However, their statistical study, which was based on direct measurement, excludes the link between MC to energetic particles precipitating onto the atmosphere.

Based on the aforementioned studies, therefore, there is a need to estimate the energy deposition based upon model calculations with measurements and careful consideration of hemispherical differences to determine the influence on an energy balance on arrival of MC in the high latitude MLT region. In this paper, we investigate MLT responses to a fortuitous MC-driven geomagnetic storm which occurred on 8 November 2004 using ground and satellite based measurements from SANAE IV (71.7°S, 2.9°W, L = 4.3) and a nearby station, Halley (75.52°S, 26.63°W, L = 4.2) in Antarctica and also from the nearest vicinity of their conjugate magnetic footprint in the Northern hemisphere. This paper is organised as follows; we describe the data used in section 2. section 3 presents the various geophysical properties of MC and the effects from precipitating particle measurements; we present estimated energy deposition using the Monte Carlo energy transport method. Section 4 summarises the obtained results and conclusions.

2. DATA AND METHOD OF ANALYSIS

2.1 Observations

2.1.1 Geophysical Parameters

The geophysical parameters for this event were obtained from the space physics research facility in the OmniWeb database. The data set was created at the National Space Science Data Center, http://omniweb.gsfc.nasa.gov, by interspersing, after cross-normalizing, field and plasma data from each of several spacecrafts that contribute measurements (King and Papitashvili 2005). Therefore, the database provides multi-source measurements of near-Earth solar wind, magnetic field and plasma parameters from different instruments. The solar activity indices (King and Papitashvili 2005), included in the database served as a proxy for the state of the ring current and magnetospheric convection. From different parameters available from the database, only those relevant to characterising the MC were obtained as presented in section 3.1.

2.1.2 The Imaging Riometer Absorption Data

To study the reaction of MCs with the atmosphere over

the region of interest, we used the imaging riometer data (Hargreaves 1969; Browne et al. 1995; Wilson and Stoker 2002). The riometer data employed in this study was obtained from two locations, Halley in the Southern Hemisphere and stations belonging to the Finnish chain which is at the vicinity of the Halley magnetic conjugate in the Northern Hemisphere. One other aim of this work is to build a futurology over SANAE IV. Halley riometer techniques (Hargreaves 1969) are similar to that from SANAE IV (Wilson and Stoker 2002) but no data was available at SANAE IV during the event. It should be noted that the ionospheric status in Halley will be a true representative of absorption above SANAE IV due to the proximity of both stations along the same magnetic field line. The Earth's encounter with MC will modify the magnetic field significantly. Under adiabatic changes to the geomagnetic field L is a conserved quantity (Roederer 1970). In a dipole magnetic field, L, is the distance from the centre of the Earth to the equatorial crossing point of a given field line. The McIlwain L shell used in this study is calculated using the International Geomagnetic Reference Field (IGRF) model from http://ngdc.noaa.gov. It is expected that for any simultaneous precipitation, where particles are precipitated over a wide region, it would be detected at both stations simultaneously. For this reason the conjugate points of all the riometer data used are shown. Figure 1 shows that Halley and the Finnish riometer chains are on roughly the same L-shell, but are separated by about 4 hours of magnetic local time. The field line from Halley and SANAE IV intersects at Oulu, a location at close proximity to Rovalemi in Northern Hemisphere. The so called 'Wave-particle' interactions on a given field line may lead to precipitation at both foot-points of the field line. Therefore, the effect at the conjugate hemisphere is more true for Oulu and Rovalemi, which is at a roughly same L-value with SANAE IV and Halley. The locations of the Finnish chain of riometer stations and their L-values are tabulated in Table 1. A riometer responds to the integrated absorption of cosmic ray noise through the ionosphere (Clilverd et al. 2010) where the particle motion is collision dominated. The riometers are widebeam, typically 30 MHz and sensitive to any incident particle population capable of reaching the ionosphere in the range of 70 - 100 km (that is, D-region).

The amount of the background cosmic radio noise disrupting the ionosphere is known to be constant for a particular location and at a given time of the day. In order to identify extraordinary absorption, a reference Quiet Day Curve (QDC) is an important parameter to be considered. Any deviations from this expected value must be due to absorption in the ionosphere as used in this study. An absorption due to such an event was quantified by calculations of an electron number density.

2.1.3 Precipitation

The absorption was expected to be as a result of precipitating particles on 8 November 2004. So, we used electron and proton data from NOAA/POES (National Oceanic and Atmospheric Administration Polar Orbiting Environmental Satellites). During this event, three satellites, NOAA 15, 16 and 17 were orbiting the Earth in a polar-orbiting, Sun-synchronous, and low-altitude (850 km) pass with a period of about 100 minutes. Each satellite, has on-board the Medium Energy Proton and Electron Detector (MEPED) and Total Energy Detector (TED) that monitor the intensities of charged particle radiation at higher energies (Rodger et al. 2010a). The MEPED on each satellite provides directional

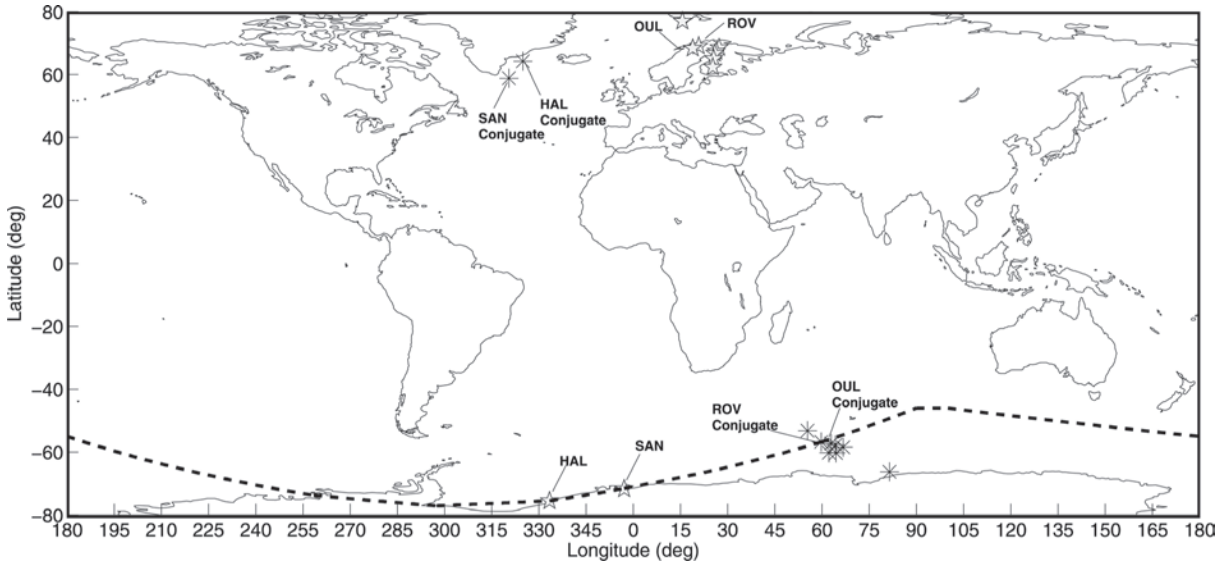

Fig. 1. Map showing locations of Halley's riometer, SANAE IV, the Finnish riometer chain with a star symbol and their conjugate points in pentagrams. Halley's L-shell is plotted as a dashed black curve.

Table 1. Locations of the riometer data used.

Station Name	Station Code	Geographic coordinates	*L*-value
SANAE IV	SAN	71.68°S, 2.85°W	4.32
Halley	HAL	75.52°S, 26.63°W	4.2
Hornsund	HOR	77.00°N, 15.60°E	13.2
Kilpisjärvi	IRIS	69.05°N, 20.79°E	6.0
Abisko	ABI	68.40°N, 18.90°E	5.7
Ivalo	IVA	68.55°N, 27.28°E	5.6
Sodankylä	SOD	67.42°N, 26.39°E	5.2
*Rovanlemi	ROV	66.78°N, 25.94°E	4.9
*Oulu	OUL	65.05°N, 25.54°E	4.4
Jyväskylä	JYV	62.42°N, 25.28°E	3.7

*Note: * ROV and OUL are the closest conjugate vicinity of SANAE IV and Halley.*

(0° telescopes for precipitating and 90° for trapped) measurements of protons and energetic electrons. For this study, data from the 0° telescope was selected only when it measured protons and electrons inside the loss cone. Similarly, TED monitors proton and electron fluxes. Four detectors (two electrons and two proton detectors) are mounted in two groups, where one group is viewing radially outward from the Earth and the other group viewing at 30°. Each group has a proton and an electron detector. At aurora altitudes the first group, looks approximately along the field line referred to as the vertical detector. In this study, we used fluxes from the TED vertical detector. Also, the POES measurements were ordered by parameter *L*. The MEPED measurements of energetic electrons have been found to be proton contamination (Rodger et al. 2010a). This study applies correction to remove protons from the precipitating electron data. For this corrective purpose, data from 0° telescope was selected only when it measure electrons inside the loss cone. The fidelity of reducing proton contamination, to provide clean measurements of precipitating electrons, was obtained from Lam et al. (2010) who suggested a first order correction,

$$\alpha + 15^{\circ} < \alpha_{LC} \tag{1}$$

where α is the local particle pitch angle at the satellite, α_{LC} is the edge of the lost cone, while the telescope opening angle is 15°. Assuming conservation of the first adiabatic invariant, the local pitch angle at the satellite, equivalent to the edge of the loss cone was determined by:

$$\alpha_{LC} = \int \frac{B_{sat}}{B_{120}} \tag{2}$$

Both the ambient magnetic field at the spacecraft B_{sat} and the ambient magnetic field at the foot of the field line which intersects ~120 km above the Earth are obtained from IGRF model.

2.2 Model Calculations

2.2.1 Energy Deposition

Based on Berger et al. (1970), the energy deposition by the energetic particles is calculated using the Monte Carlo Energy Transport model herein refer to as MCETM:

$$s_{mb} = \frac{z_m(h_b) - z_{mn}}{\cos\theta_n} \tag{3}$$

where, $z_m(h_b) = \int_h^{h_0} D(h_b')\,dh'$ is the atmospheric depth used as an input for the model with $D(h_b')$ as the density supposing the electron passes through a particular 'scoring boundary' h_b between the n'th and $n+1'$st collisions, and $z_m(h_b)$ being the mass thickness at each corresponding height. The distance, s_m, traveled by electrons within the boundary *b* was given as:

$$s_m = \int_{E_{n+1}}^{E_n} \frac{dE}{L(E)} = r_0(E_n) - r_0(E_{n+1}) \tag{4}$$

which we obtained by interpolating the atmospheric mean range r_0 against acquired electrons' energy *E* using stopping power *L*. The pathlength from the n'th collision point to the boundary results to s_{mb} as given in the first equation.

Berger et al. (1970) noted the applicability of this program to problems which were actually observed atmospheric phenomena and those predicted by the simplified calculations. In this case, rather than theoretical assumption of characteristic energy, we first combined the electron (> 30, > 100, and

> 300 keV) energies from MEPED detector into an energy range of 30 - 100 and 100 - 300 keV, these integral fluxes are then combined with those retrieved from TED in the range of 2116 - 3075 and 6503 - 9167 eV to obtain differential fluxes. That is, the four differential energy channels are fitted into a double exponential spectrum:

$$j(E) = A_1 \cdot e^{-\frac{E}{E_1}} + A_2 \cdot e^{-\frac{E}{E_2}} \quad (5)$$

The characteristic energies, E_1 and E_2 , and the factors A_1 and A_2 are then determined. We found a very high energy spectrum associated with this event with characteristic energies between 3 and 135 keV. At every pathlength, we obtained energy deposited at various heights of interest per time. Similar to Rees (1989), the energy expended by the primary precipitation for each ion-electron pair production is taken to be a value of 35 eV. Mæhlum (1973) provided a three part exponential technique useful for obtaining information about the deposition of proton energy as a function of altitude: $\frac{dE}{dz} = 236\, E^{-0.78}$, given that the energy loss, $\frac{dE}{dz}$, is in M eV cm^2 g^{-1} units. Using three part exponential function, we obtain the spectra used in MCTEM for proton energy deposition. Both electrons and protons were assumed to be vertically incident. In all, the aforementioned atmospheric composition and densities are estimated based on the Mass-Spectrometer-Incoherent-Scatter Extended model (MSISE-90) which is identical to the COSPAR International Reference Atmosphere-86 (CIRA-86).

2.2.2 Electron Number Density

Electron number density from an absorption of radio waves by the ionosphere was usually calculated using the Appleton-Hartree magnetoionic theory (Majumdar 1972). For the Halley riometer used in this study, the radio wave frequency (30 MHz) was larger than both the component of the gyro-frequency vector in the direction of propagation, and the collision frequency. Using a classical equation (Hargreaves 1992) and approximation (Wang et al. 1994), the expression for the absorption $A(dB)$ was reduced to the following formula:

$$A(dB) = \frac{4.58 \times 10^{-5} \pm \sqrt{b^2 - 4ac}}{\omega^2} \int N_e(h)\, \upsilon(h)\, ds \quad (6)$$

where $N_e(h)$ gives the electron number density at any height h, $\upsilon(h)$ which is $\sim\rho(h)$ (Hargreaves and Friedrich 2003) and obtained as the property of the atmosphere [i.e., proportional to pressure, $\rho(h)$], ω the radio wave angular frequency, and ds the path element.

3. RESULTS AND ANALYSIS

3.1 The Event Characteristics

A MC as one type of interplanetary ejecta can be identified by its definite geo effective signatures. Due to the important position of these signatures in solar terrestrial events, understanding the MC is valuable and helpful for the space weather research, especially for improving the prediction level of the occurrence of intense geomagnetic storms that can significantly affect the MLT energy budget. Measurements of geophysical parameters were then inspected from the OMNI data set for evidence of these signatures, including enhanced magnetic field strength, long and smooth rotation of field vector and low proton temperature (Burlaga et al. 1982; Burlaga 1988; Lepping et al. 1990). An enhanced magnetospheric convection resulting from the MC may be an indication that the solar wind energy gained access into the MLT region.

Figure 2 presents the geophysical properties of a MC event which occurred at about 3.4 UT on 8 November 2004 until 16.6 UT of the same day. Figure 2a is a strong magnetic field magnitude (peak value 40 nT) with low variance and organized rotation of the magnetic field direction (y - z) in geocentric solar magnetospheric (GSM) coordinate in Fig. 2b, and depressed proton number density in Fig. 2c. The solar wind speed is increased in Fig. 2d probably because this event is fast (a fast solar wind speed is defined as having speeds usually more than 500 km s^{-1}). The helium to proton ratio in Fig. 2e is enhanced throughout the MC causing low pressure. The low ratio of plasma pressure to magnetic pressure is affirmed by the drop in dynamic pressure in Fig. 2f and plasma beta in Fig. 2g. The magnetospheric convection measurement, Kp index in OMNI format as presented in Fig. 2h shows that the onset of event begins during enhanced magnetospheric activity indicating that the magnetosphere is immersed in high solar wind flow. It can be observed from this panel that there is a consistent pattern of magnetospheric response to the MC, as gauged by this index. Typical classifications of geomagnetic storms use the minimum of the Kp index to determine the size of the storm; by these classifications, this event is over 70 percent higher than the small geomagnetic storm.

The resultant increase in the activity during MC may cause the upper most layer of the magnetophere to move inward from its quiet-time median standoff distance. Such compression of the magnetopause from a stand-off distance will allow the gradual loss of energetic particles from the higher radial distances (that is, higher L-values). Depending upon the initial kinetic energy, particle of this magnetospheric origin can precipitate and be absorbed into different heights of the atmosphere.

3.2 Particle Absorption and Precipitation

Figure 3 shows hourly riometer absorption measurements.

At the arrival of MC there is a rise in absorption in coincidence with the onset of high magnetospheric activities. The absorption peaks continue to reach a maximum on arrival of MC and drops slightly after impact. We continue to notice absorption 3 days after the event which is almost the same value with the peak seen on MC, indicating that the particle precipitation is fairly uniform over a large area. Generally, the different values in absorption seen after the MC indicate, however, the precipitation has some localised or multiple contributing processes. These observations can be seen in the vicinity of the northern conjugate measured by a Finnish chain of riometers as presented in Fig. 3b. It is also noted that the average absorption peaks follow the duration of an enhancement in the magnetosphere. The energy spectrum of the precipitating energetic particles varies from one event to another, as well as during an event. However, the criterion for MC occurrence is fulfilled throughout this period with the peaks in absorption at the main phase of the storms triggered by MC. Even so, we wish to ascertain if the changes or the high peak in absorption are actually due to changes in particle precipitation at the onset of this event. A way toward ascertaining this is to first quantify the resulting electron density from the ionospheric absorption.

Figure 4 shows the resultant electron densities using Eq. (6). In order to effectively exclude any other possible local and multiple contributing processes, we have centered the calculations on a single day of the MC. The main part of the MC produces ionisation around 90 km on arrival of MC at Earth until following day. The electron number density calculations show enhanced electron densities above 90 km on the impact of the MC which coincides with the rise in the Kp index. In these conditions, lower energy protons are also expected to reach the atmosphere. Comparing this model variations with riometer absorption in Fig. 3 shows that the two impulsive peaks on arrival of MC and a day following it coincide well with each other suggesting that there is indeed a precipitation of energetic electrons into the D-region ionosphere; although, there is some discrepancy in the early part

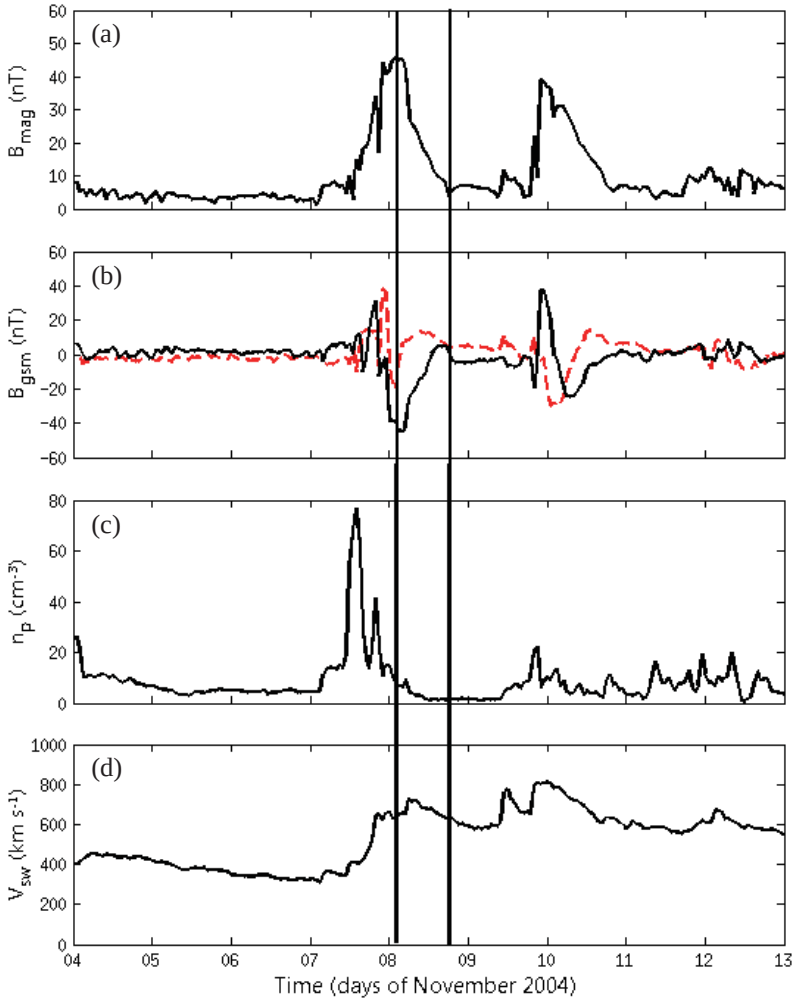

Fig. 2. Plots of properties of MC used: panels (a) show magnetic field magnitude, (b) IMF in GSM coordinate in z-component (black line) and y-component (red dashed line), (c) proton number density, (d) solar wind speed, (e) n_α/n_p, (f) dynamic pressure, (g) plasma beta, (h) Kp index in OMNI format. The vertical borderline indicates MC interval.

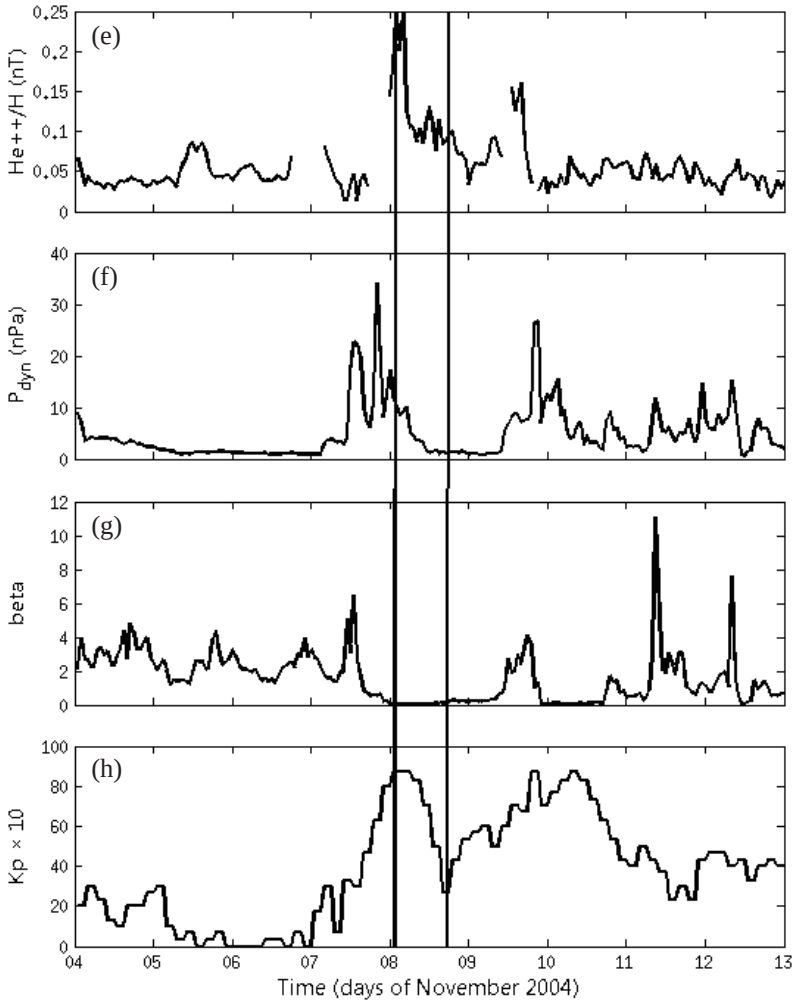

Fig. 2. (Continued)

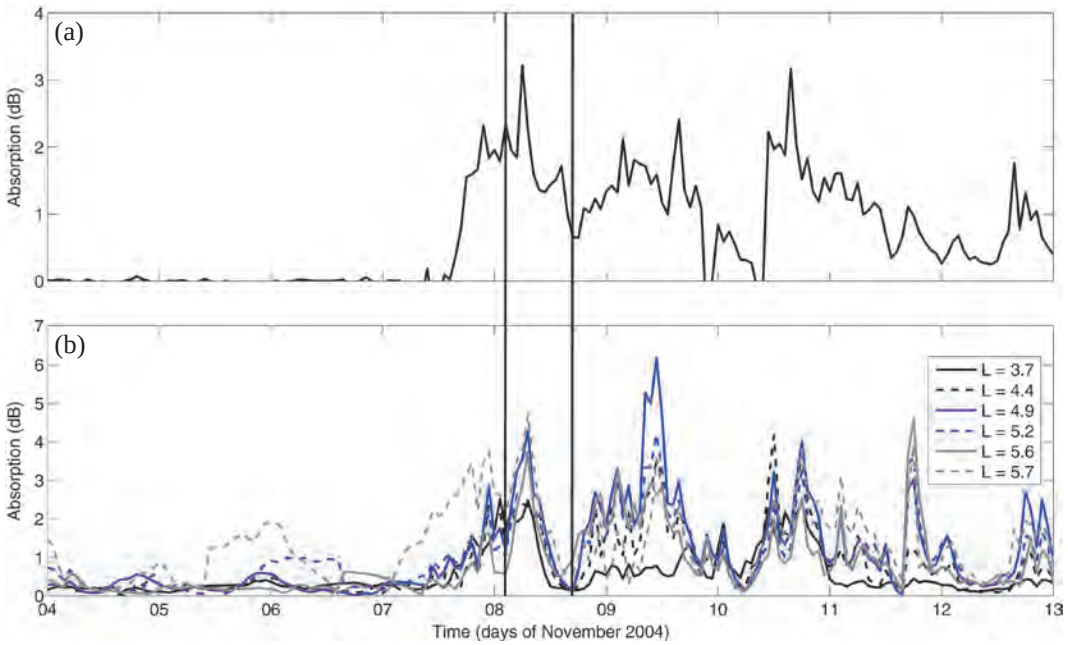

Fig. 3. Hourly riometers absorption during MC. (a) Indicates absorption from Halley and (b) Finnish chain of riometers. The format is same as in Fig. 2.

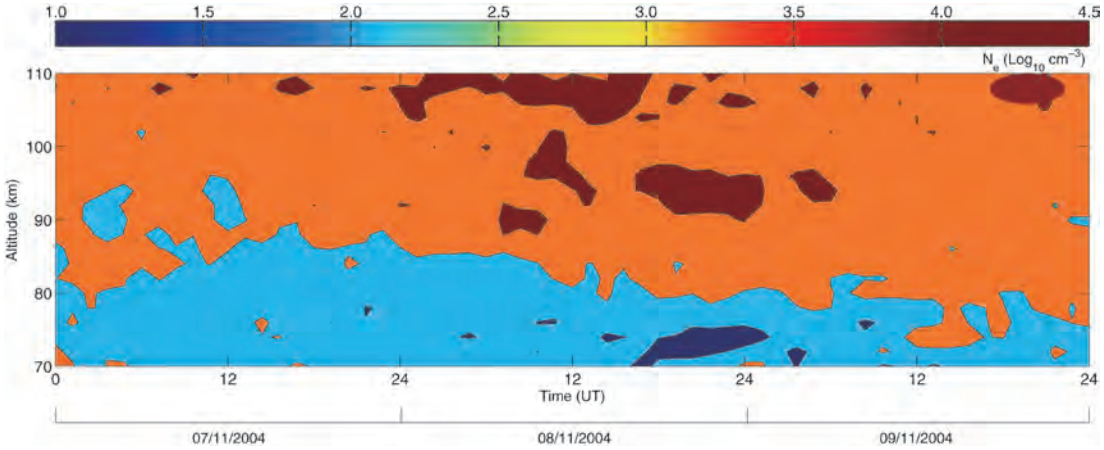

Fig. 4. Altitude-time-color map of modeled electron number density from absorption measurements.

(3:40 UT) of the event. This is likely to be as a result of the extremely low proton density at the start of the event, which causes less ionisation below 100 km altitude. On the other hand, the enhanced electron number densities above 100 km is due to background solar radiation in the E-region. For clarity, we checked the Solar flux proxy adjusted to 1 AU during the MC (not shown). The F10.7 index that measures the solar radio flux per unit frequency at a wavelength of 10.7 cm correlates well with Solar Extra Ultra Violet (EUV) emissions. A visual inspection indicated that the Solar flux proxy varied from 125 s.f.u. at the impact of MC to 140 s.f.u. a day after and later dropped to 90 s.f.u. The Halley and SANAE IV regions which lie entirely in the Southern Hemisphere's polar latitude receive relative high amount of solar EUV during summer. Previous studies, according to Sripathi (2012), have indicated that electron density varies linearly with solar flux. Another way to ascertain if the peaks in absorption are actually due to precipitation triggered by MC is to check the degree of precipitating particles at this time.

Using particle measurements from the 0° detectors on the MEPED and TED instruments onboard NOAA 15, 16 and 17, we obtained the precipitating particles over and near our regions of interest at several points in time. The particle measurement was projected down to about 100 km which is near the foot of the magnetic field line, and sort the measurement in a McIlwain *L* shell of ± 0.02 *L* around Halley (*L* = 4.2), SANAE IV (*L* = 4.3) and at the vicinity of their conjugates at only Oulu (*L* = 4.4) and Rovalemi (*L* = 4.9). As previously mentioned, the conjugate effect will verified more at both Oulu and Rovalemi in the Northern conjugate. Due to an increase in data points, a linear interpolation technique is employed (Fang et al. 2007). Due to the interpolation, however, the time differences between the satellite crossings, and the coarse grid averaging out of a possible local effect, we can only expect a relative correlation between riometer measurements at these regions and the fluxes retrieved from the NOAA satellites.

Figures 5a - d presents the electron fluxes in energy channels > 30, > 100, and > 300 keV above Halley, SANAE IV and at the vicinity of the Northern conjugate, Oulu and Rovalemi, using simple interpolation techniques. We find that over Halley and SANAE IV, as presented in Figs. 5a and b respectively, absorption peaks coincided with relative increase in precipitating electron flux on the arrival of MC. The MC driven precipitation is seen to be energy dependent at all local times, which did not recover quickly to the pre-event level. The prolonged recovery across all the energy bands was likely to be that acceleration processes are either enhanced or dominated by multiple loss processes capable of acting on varying electron energies. This partly explains the reason for absorption peaks seen days after the event. The region near Oulu and Rovalemi in Figs. 5c and d respectively show a similar scenario for the conjugate vicinity in the Northern Hemisphere indicating, perhaps, a global feature. We find this assumption meaningful because Halley, SANAE IV and the Finnish riometer chain along the same *L*-shell are separated by about 4 hours of magnetic local time; but, at the same time we find an increase in absorption from particle precipitation at Southern Hemisphere stations to have been simultaneous to or tied with that at the Northern conjugate. The idea that this may indeed occur is a concept of simultaneous precipitation, where particles are precipitated over a wide enough region to be detected at both stations simultaneously. As seen in Fig. 3, there is a very similar absorption profile at the Halley, SANAE IV and Finnish riometers indicating that the same precipitation event was measured at both stations. Apparently, the smooth rotation of IMF-Bz converts closed electron drift paths to open paths allowing electrons to be lost through magnetopause shadowing, thus, precipitate into the mesosphere region as indicated by riometer. Similar to the modeled background electron number density in the presence of the MC-triggered absorption, we investigated the density height profile by re- placing the absorption with these

measured differential electron fluxes as presented in Fig. 6. We find a significant correlation between Figs. 4 and 6 for densities upon a MC arrival. The high densities of electrons during the MC allow us to test whether a MC is related to the density of free electrons or to something else. The number density of electrons during the main phase of the event increase for both height profiles of electron density obtained from absorption and precipitating electron fluxes. The situation is obviously the same for protons as shown in Fig. 7. We find that protons across the energy channels are associated with the absorption due to the MC triggered storm.

3.3 Energy Deposition

Figure 8 shows the energy deposition by the electrons at the vicinity of SANAE IV and its conjugate using the MCETM discussed in Subsection 2.2.1. In Fig. 8 (top panel left), we find a local maxima of energy deposition at 90 km on 8 November 2004 after the impact of a MC. This is obvious from the mean profile in the top panel (right) of Fig. 8. The enhancement in the energy deposition persists till a day after the event. While we continue to notice a peak in the energy deposition, even in the Northern vicinity, Fig. 8 (bottom) shows that the situation is only comparable at 100 km a day after the impact of a MC. This also coincides with enhanced magnetospheric activity. Comparing the electrons deposition with the deposition by MC protons as presented in Fig. 9, we find that the energy deposition is generally dominated by electrons, indicating an enhanced electron fluxes.

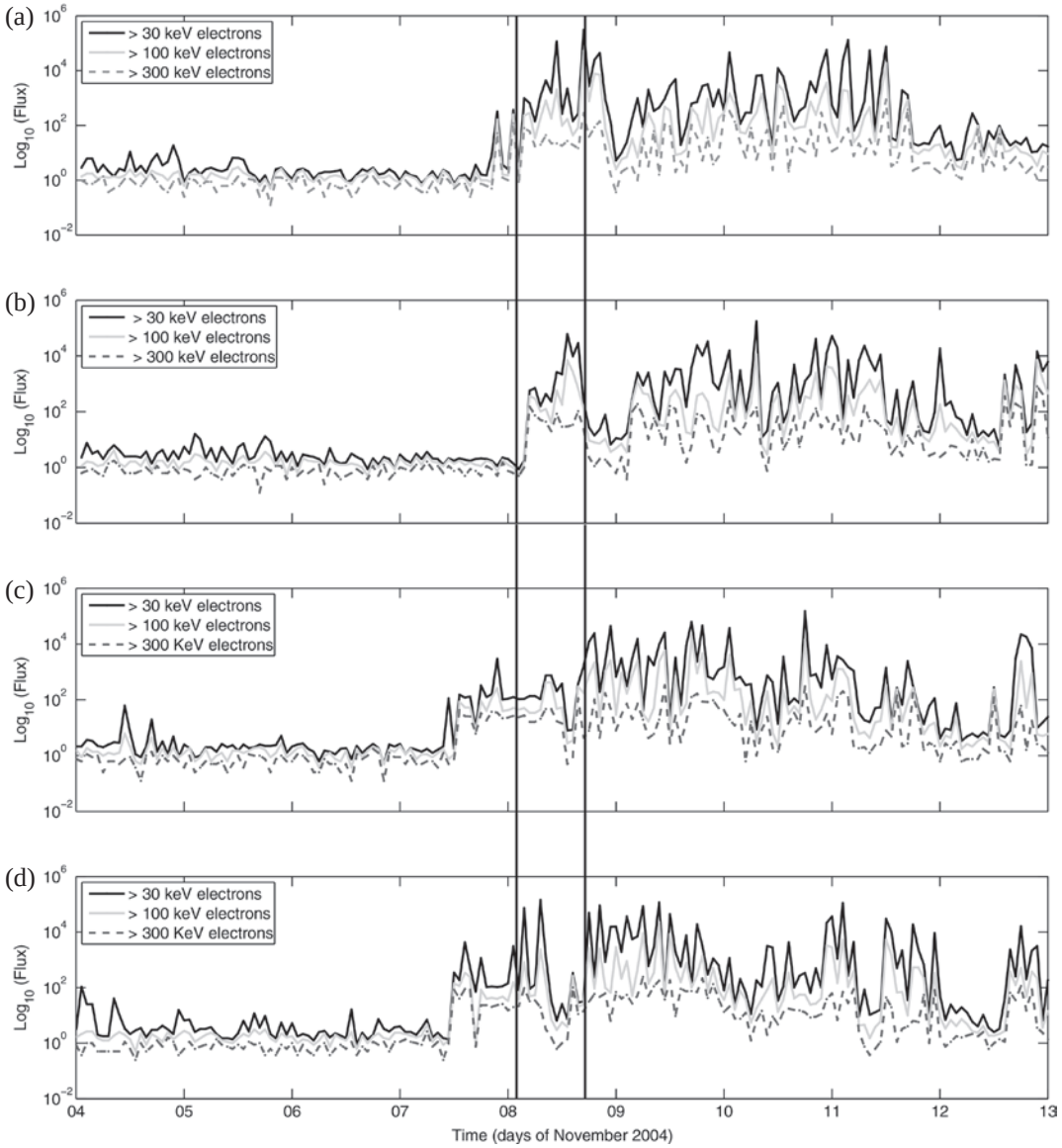

Fig. 5. NOAA/POES electrons precipitation on arrival of MC. (a - d) Indicate electron precipitation from Halley (a), SANAE IV (b), Oulu (c) and Rovalemi (d). MC interval is bordered by vertical lines.

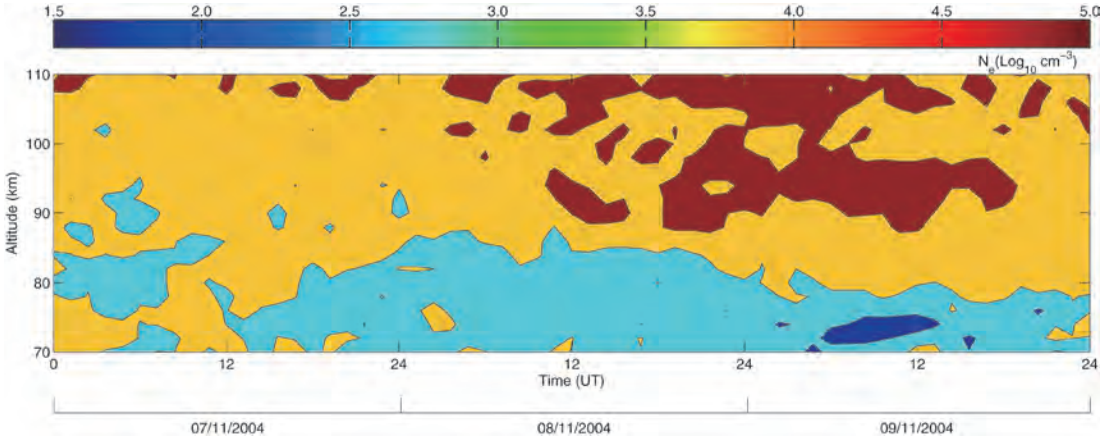

Fig. 6. Altitude-time-color map of modeled electron number density from differential electron fluxes.

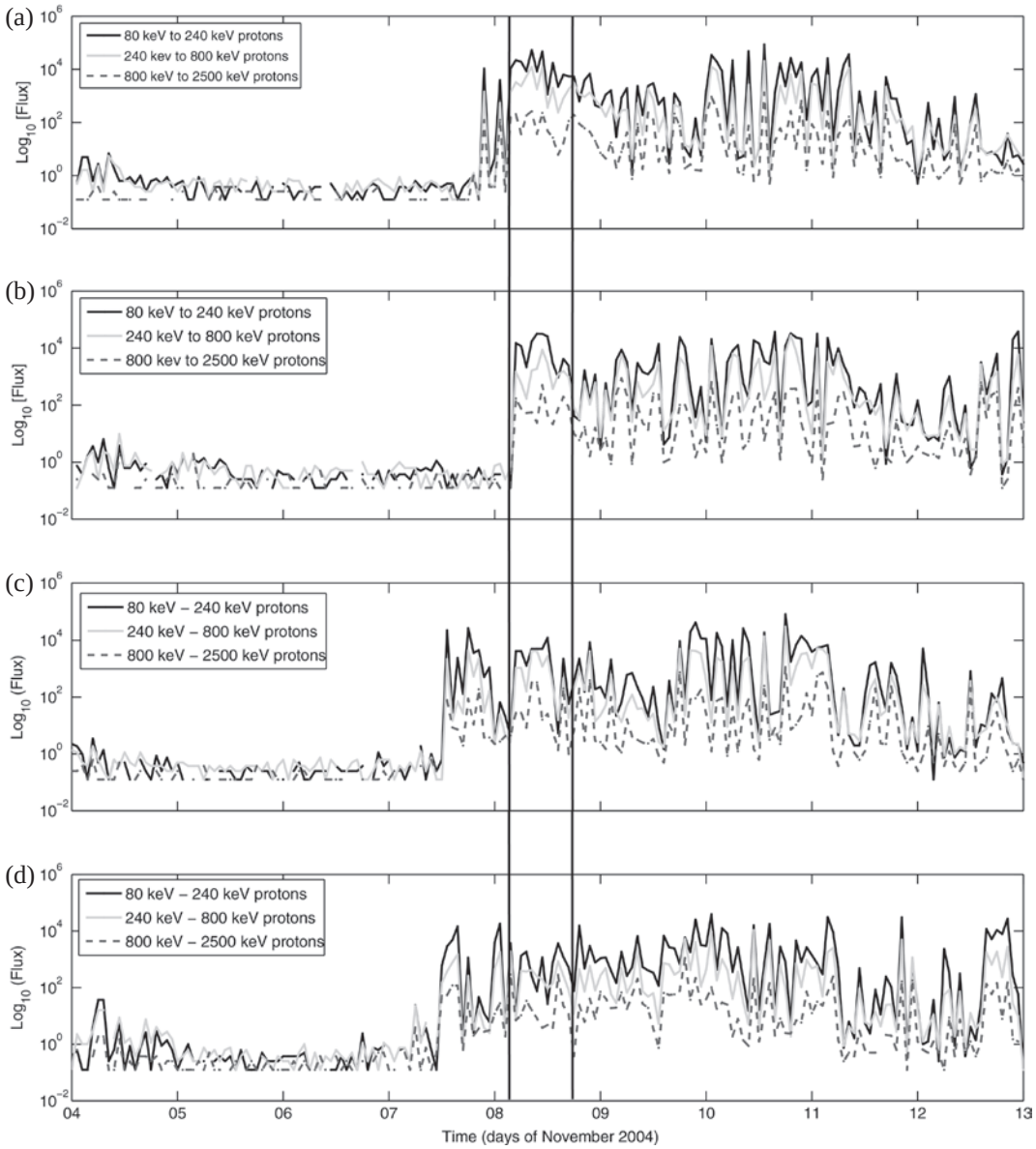

Fig. 7. NOAA/POES protons precipitation on arrival of MC. (a - d) Indicate precipitation from Halley (a), SANAE IV (b), Oulu (c) and Rovalemi (d). Format is as in Fig. 5.

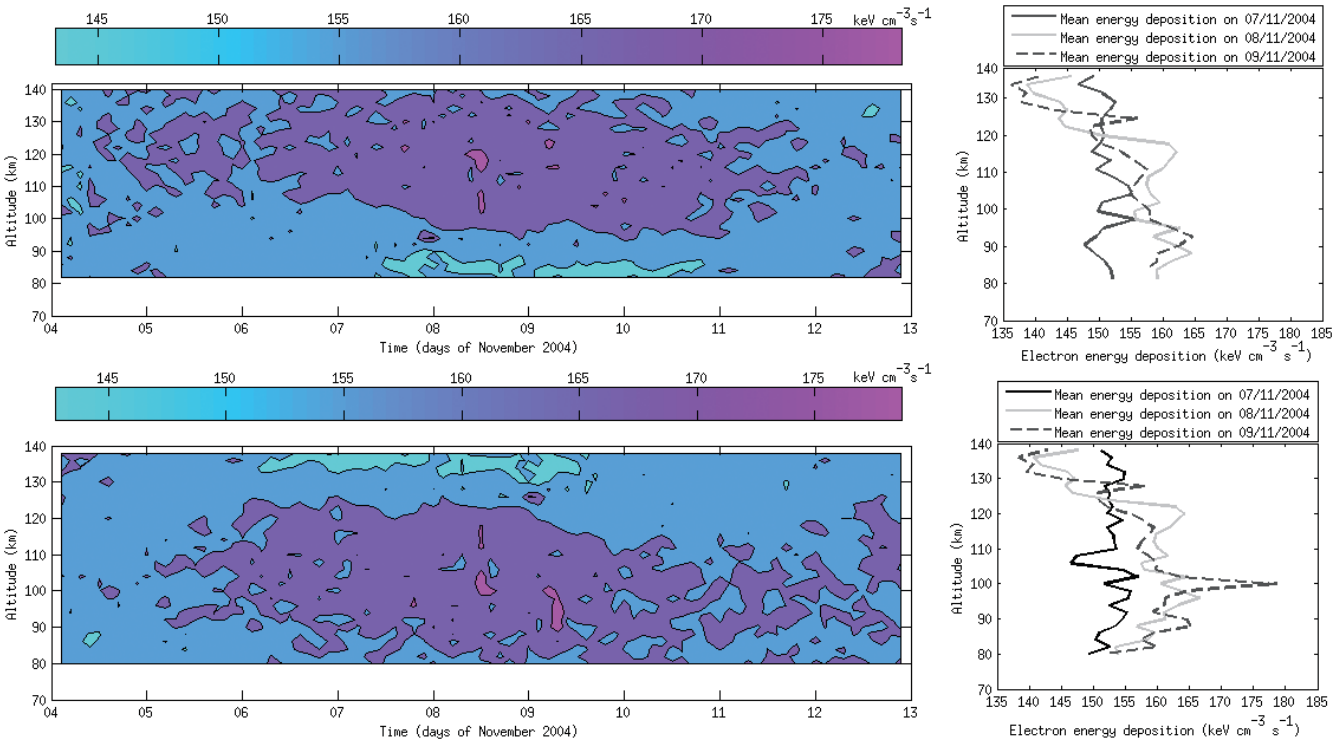

Fig. 8. Energy deposition by MC electrons. The top panel (left) shows the energy distribution as a function of altitude and time in days near SANAE IV and (right) daily mean profile centered a day on MC arrival at Earth. The bottom (left) and (right) panels are similar scenarios near Oulu in Northern Hemisphere.

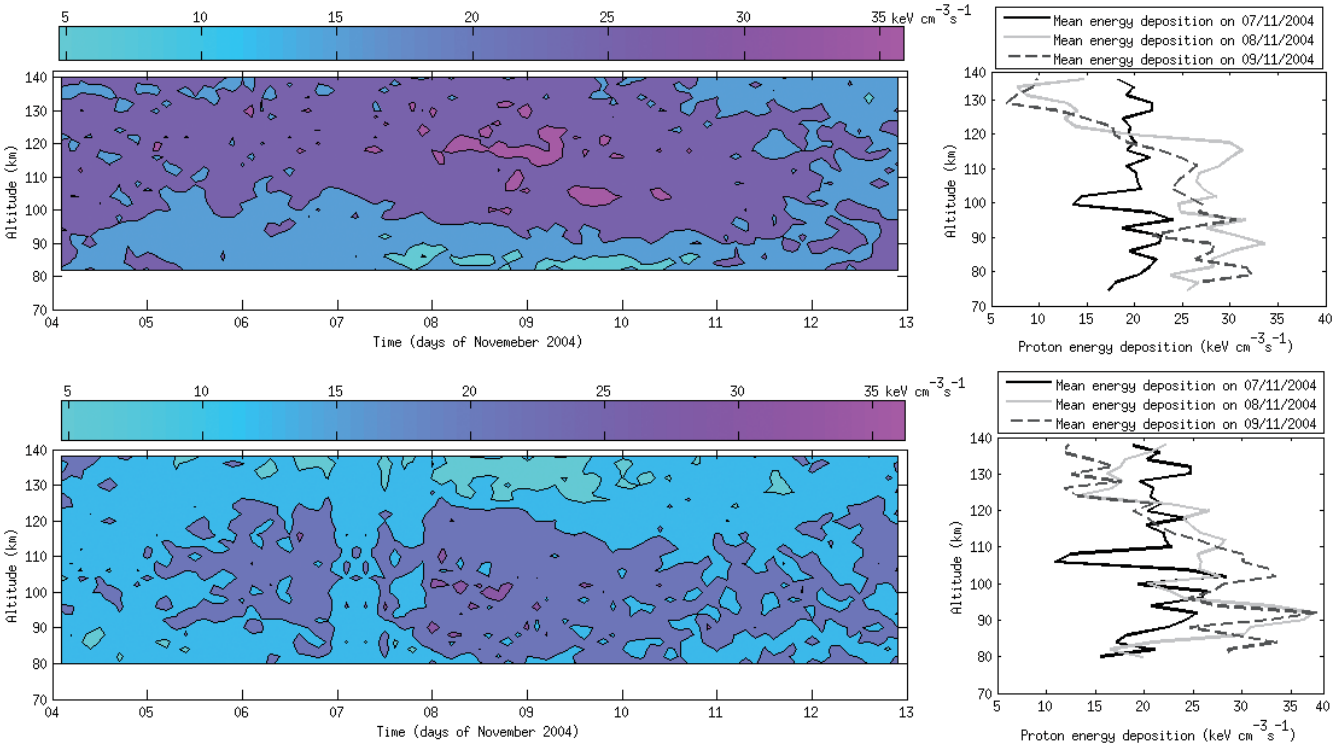

Fig. 9. Energy deposition by MC protons. Format is as in Fig. 8.

According to Fig. 8, we find an electron energy deposition rate of about 165 keV cm^{-3} s^{-1}, an equivalent of 2.64×10^{-14} J cm^{-3} s^{-1} in an acceptable SI unit, which is 0.32×10^{-14} J cm^{-3} s^{-1} less than what is found at 100 km altitude in the northern conjugate vicinity on the impact of MC. This is capable of giving rise to a heating rate of approximately 0.77 K h^{-1} in an ideal diatomic gas atmosphere or about 0.12 K h^{-1} if the atmosphere is assumed to be ideal monoatomic at this altitude. The rate derived for diatomic gas atmosphere is in close agreement with previous work posted by Offermann (1985), who found particle precipitation heating rates of approximately 0.1 K h^{-1} at 90 km during high geomagnetic conditions which is in closer agreement to what we have obtained for our region of interest in Northern hemisphere and at its conjugate. Energetic particles can cause heating and eventual cooling, depending upon which altitude is studied and the specific militating condition. Here, we find that energy deposition is deeper in the Southern hemisphere than in the Northern conjugate upon the arrival of a MC.

But it is more likely, however, that the arrival of MC causes the persistence of energy deposition seen days after the event. This is arguable since this paper presents a case study. However, momentum flux, that is, correlation of the meridional (V) winds and the longitudinal asymmetry of the zonal (U) wind, is a good proxy for disturbed mesopause region from geoineffective sources. Futurology aims to investigate momentum flux using neutral wind measurements from SuperDARN radar network. With this, we would be able to quantify the character of global-scale meridional wave period. A visual check on the QBO upon arrival of this left-handed MC shows that it was during easterly phase, indicating a probable disturbed stratosphere (Georgieva et al. 2005) caused by this event.

4. SUMMARY AND CONCLUSIONS

The MC event which occurred on 8 November 2004 coincided with enhanced magnetospheric conditions. On the arrival of the MC at Earth, which triggered large geomagnetic disturbance, we estimated energy deposition into the atmosphere. Upon arrival, the Halley riometers in Antarctica and that of Finish, a conjugate vicinity in the opposite hemisphere, indicated absorption peaks and enhanced electron densities. The energy deposited at this time interacted with various plasma waves and thus, causing enhanced ionospheric density within collision dominated regions. The electron number density calculations show enhanced densities above 90 km on the impact of MC which coincides with the rise in magnetospheric convection. Energetic particle measurements from NOOA/POES that pass through and near these regions confirm that the absorption events are most likely due to particle precipitation caused by the arrival of MC. Using MCETM shows that the energy deposition dominated by electrons on arrival of this event is capable of giving rise to an heating rate of approximately 0.77 K h^{-1} in an ideal diatomic gas atmosphere or about 0.12 K h^{-1} if the atmosphere is assumed to be ideal monoatomic at the altitude of about 100 km, which is in close agreement to previous work in the Northern Hemisphere. It was found that an approximation of these energy deposition rates for Southern Hemisphere extends to lower altitudes. Considering the size of the estimated heating rates, it could be hypothesized that there is significant temperature effects on the particle precipitation in the upper mesosphere above these regions following the arrival of MC. We choose to be prudent with our conclusions regarding these solar influences however, since the magnitude of the heating and cooling rate associated with MC do not necessarily preclude influences by atmospheric features such as tides and gravity waves as these remain an arduous challenge. In order to elucidate what these effects might have, further work is underway to analyze the associated wave field with the MC arrival at Earth. The particle precipitation investigated in the present study occurred during ICME-driven storms. Precipitation also needs to be studied in high-speed-solar wind-driven storms. Because high-speed-solar wind-driven storms are more variable than the ICME-driven storms, the rate of energy deposition under more varied conditions will be studied.

Acknowledgements The authors are grateful for the availability of OMNI data provided by the GSFC/SPDF at the OMNIWeb interface, the NOAA/POES at NGDC and Finnish chain of riometers in SGO. The SuperDARN radar network and Halley riometer data are provided by the British Antarctic Survey, UK, from their Web site at http://psddb.nerc-bas.ac.uk/. And, the authors also express thanks to TAO's anonymous reviewers for their valuable comments and suggestions. Research is supported by the South African National Space Agency (SANSA).

REFERENCES

Antonucci, E., J. T. Hoeksema, and P. H. Scherrer, 1990: Rotation of the photospheric magnetic fields: A north-south asymmetry. *Astrophys. J.*, **360**, 296-304, doi: 10.1086/169120. [Link]

Berger, M. J., S. M. Seltzer, and K. Maeda, 1970: Energy deposition by auroral electrons in the atmosphere. *J. Atmos. Terr. Phys.*, **32**, 1015-1045, doi: 10.1016/0021-9169(70)90115-7. [Link]

Browne, S., J. K. Hargreaves, and B. Honary, 1995: An imaging riometer for ionospheric studies. *Electron. Comm. Eng. J.*, **7**, 209-217, doi: 10.1049/ecej:19950505. [Link]

Burlaga, L. F., 1988: Magnetic clouds and force-free fields with constant alpha. *J. Geophys. Res.*, **93**, 7217-7224, doi: 10.1029/JA093iA07p07217. [Link]

Burlaga, L. F., L. Klein, N. R. Sheeley Jr., D. J. Michels,

R. A. Howard, M. J. Koomen, R. Schwenn, and H. Rosenbauer, 1982: A magnetic cloud and a coronal mass ejection. *Geophys. Res. Lett.*, **9**, 1317-1320, doi: 10.1029/GL009i012p01317. [Link]

Clilverd, M. A., C. J. Rodger, R. J. Gamble, T. Ulich, T. Raita, A. Seppälä, J. C. Green, N. R. Thomson, J. A. Sauvaud, and M. Parrot, 2010: Ground-based estimates of outer radiation belt energetic electron precipitation fluxes into the atmosphere. *J. Geophys. Res.*, **115**, A12304, doi: 10.1029/2010JA015638. [Link]

Estep, G. M., J. L. Horwitz, Y. J. Su, P. G. Richards, G. R. Wilson, and D. G. Brown, 1999: A Dynamic Fluid-Kinetic (DyFK) model for ionosphere-magnetosphere plasma transport: Effects of ionization and thermal electron heating by soft electron precipitation. *Terr. Atmos. Ocean. Sci.*, **10**, 491-510.

Fang, X., M. W. Liemohn, J. U. Kozyra, D. S. Evans, A. D. DeJong, and B. A. Emery, 2007: Global 30-240 keV proton precipitation in the 17-18 April 2002 geomagnetic storms: 1. Patterns. *J. Geophys. Res.*, **112**, A05301, doi: 10.1029/2006JA011867. [Link]

Georgieva, K., B. Kirov, D. Atanassov, and A. Boneva, 2005: Impact of magnetic clouds on the middle atmosphere and geomagnetic disturbances. *J. Atmos. Sol.-Terr. Phys.*, **67**, 163-176, doi: 10.1016/j.jastp.2004.07.025. [Link]

Grenfell, J. L., R. Lehmann, P. Mieth, U. Langematz, and B. Steil, 2006: Chemical reaction pathways affecting stratospheric and mesospheric ozone. *J. Geophys. Res.*, **111**, D17311, doi: 10.1029/2004JD005713. [Link]

Hargreaves, J. K., 1969: Auroral absorption of HF radio waves in the ionosphere: A review of results from the first decade of riometry. *P. IEEE.*, **57**, 1348-1373, doi: 10.1109/PROC.1969.7275. [Link]

Hargreaves, J. K., 1992: The Solar-Terrestrial Environment: An Introduction to Geospace - the Science of the Terrestrial Upper Atmosphere, Ionosphere, and Magnetosphere, Cambridge Atmospheric and Space Science Series, Cambridge University Press, Cambridge, 420 pp.

Hargreaves, J. K. and M. Friedrich, 2003: The estimation of D-region electron densities from riometer data. *Ann. Geophys.*, **21**, 603-613, doi: 10.5194/angeo-21-603-2003. [Link]

Hviuzova, T. and S. Leontyev, 1997: Characteristics of aurora spectra connected with high-speed streams from coronal holes. *Geomagn. Aeron.*, **37**, 155-159. (in Russia)

Hviuzova, T. and S. Leontyev, 2001: Characteristics of aurora spectra connected with non-stationary solar wind streams. *Geom. Aeron.*, **41**, 337-341. (in Russia)

Kang, J. E., S. K. Song, H. W. Lee, and Y. K. Kim, 2012: The influence of meteorological conditions and complex topography on ozone concentrations in a valley area near coastal metropolitan cities. *Terr. Atmos. Ocean. Sci.*, **23**, 25-38, doi: 10.3319/TAO.2011.06.30.02(A). [Link]

King, J. H. and N. E. Papitashvili, 2005: Solar wind spatial scales in and comparisons of hourly wind and ace plasma and magnetic field data. *J. Geophys. Res.*, **110**, A02104, doi: 10.1029/2004JA010649. [Link]

Lam, M. M., R. B. Horne, N. P. Meredith, S. A. Glauert, T. Moffat-Griffin, and J. C. Green, 2010: Origin of energetic electron precipitation >30 keV into the atmosphere. *J. Geophys. Res.*, **115**, A00F08, doi: 10.1029/2009JA014619. [Link]

Lepping, R. P., J. A. Jones, and L. F. Burlaga, 1990: Magnetic field structure of interplanetary magnetic clouds at 1 AU. *J. Geophys. Res.* **95**, 11957-11965, doi: 10.1029/JA095iA08p11957. [Link]

Lepping, R. P., L. F. Burlaga, A. Szabo, K. W. Ogilvie, W. H. Mish, D. Vassiliadis, A. J. Lazarus, J. T. Steinberg, C. J. Farrugia, L. Janoo, and F. Mariani, 1997: The wind magnetic cloud and events of october 18 - 20, 1995: Interplanetary properties and as triggers for geomagnetic activity. *J. Geophys. Res.*, **102**, 14049-14063, doi: 10.1029/97JA00272. [Link]

Mæhlum, B. N., 1973: Particle precipitation: Scattering and absorption. In: Egeland, A., Ø. Holter, and A. Omholt (Eds.), Cosmical Geophysics, Universitetsforlaget, 211-219.

Majumdar, R. C., 1972: Generalization of appleton-hartree equation of theories of collision frequency. *Indian J. Radio Space*, **1**, 31-37.

Offermann, D., 1985: The energy budget campaign 1980: Introductory review. *J. Atmos. Terr. Phys.*, **47**, 1-26, doi: 10.1016/0021-9169(85)90120-5. [Link]

Rees, M. H., 1989: The interaction of energetic solar photons with the upper atmosphere. Physics and Chemistry of the Upper Atmosphere, Cambridge Atmospheric and Space Science Series, Cambridge University Press, Cambridge, 8-23, doi: 10.1017/CBO9780511573118.003. [Link]

Roble, R. G., 1995: Energetics of the mesosphere and thermosphere, in The Upper Mesosphere and Lower Thermosphere: A Review of Experiment and Theory. AGU, Washington D.C., **87**, 1-21.

Rodger, C. J., M. A. Clilverd, J. C. Green, and M. M. Lam, 2010a: Use of POES SEM-2 observations to examine radiation belt dynamics and energetic electron precipitation into the atmosphere. *J. Geophys. Res.*, **115**, A04202, doi: 10.1029/2008JA014023. [Link]

Rodger, C. J., M. A. Clilverd, A. Seppälä, N. R. Thomson, R. J. Gamble, M. Parrot, J. A. Sauvaud, and T. Ulich, 2010b: Radiation belt electron precipitation due to geomagnetic storms: Significance to middle atmosphere ozone chemistry. *J. Geophys. Res.*, **115**, A11320, doi: 10.1029/2010JA015599. [Link]

Roederer, J. G., 1970: Dynamics of Geomagnetically Trapped Radiation, Physics and Chemistry in Space, vol. 2, Springer-Verlag, New York, 166 pp.

Rusch, D. W., J. C. Gérard, S. Solomon, P. J. Crutzen, and G. C. Reid, 1981: The effect of particle precipitation events on the neutral and ion chemistry of the middle atmosphere-I. odd nitrogen. *Planet. Space Sci.*, **29**, 767-774, doi: 10.1016/0032-0633(81)90048-9. [Link]

Sætre, C., J. Stadsnes, H. Nesse, A. Aksnes, S. M. Petrinec, C. A. Barth, D. N. Baker, R. R. Vondrak, and N. Østgaard, 2004: Energetic electron precipitation and the NO abundance in the upper atmosphere: A direct comparison during a geomagnetic storm. *J. Geophys. Res.*, **109**, A09302, doi: 10.1029/2004JA010485. [Link]

Sivjee, G. G. and D. Shen, 1997: Auroral optical emissions during the solar magnetic cloud event of October 1995. *J. Geophys. Res.*, **102**, 7431-7437, doi: 10.1029/97JA00195. [Link]

Solomon, S., D. W. Rusch, J. C. Gérard, G. C. Reid, and P. J. Crutzen, 1981: The effect of particle precipitation events on the neutral and ion chemistry of the middle atmosphere: II. Odd hydrogen. *Planet. Space Sci.*, **29**, 885-893, doi: 10.1016/0032-0633(81)90078-7. [Link]

Sripathi, S., 2012: COSMIC observations of ionospheric density profiles over Indian region: Ionospheric conditions during extremely low solar activity period. *Indian J. Radio Space Phys.*, **41**, 98-109.

Swider, W. and T. J. Keneshea, 1973: Decrease of ozone and atomic oxygen in the lower mesosphere during a PCA event. *Planet. Space Sci.*, **21**, 1969-1973, doi: 10.1016/0032-0633(73)90126-8. [Link]

Wang, Y. M., P. Z. Ye, and S. Wang, 2003: Multiple magnetic clouds: Several examples during March-April 2001. *J. Geophys. Res.*, **108**, doi: 10.1029/2003JA009850. [Link]

Wang, Z., T. J. Rosenberg, P. Stauning, S. Basu, and G. Crowley, 1994: Calculations of riometer absorption associated with *F* region plasma structures based on Sondre Stromfjord incoherent scatter radar observations. *Radio Sci.*, **29**, 209-215, doi: 10.1029/93RS01507. [Link]

Wilson, A. and P. H. Stoker, 2002: Imaging riometer observations on energetic electron precipitation at SANAE IV, Antarctica. *J. Geophys. Res.*, **107**, doi: 10.1029/2000JA000463. [Link]

Zhang, J., M. W. Liemohn, J. U. Kozyra, M. F. Thomsen, H. A. Elliott, and J. M. Weygand, 2006: A statistical comparison of solar wind sources of moderate and intense geomagnetic storms at solar minimum and maximum. *J. Geophys. Res.*, **111**, A01104, doi: 10.1029/2005JA011065. [Link]

Chapter 4

A superposed epoch study of the effects of solar wind stream interface events on the upper mesospheric and lower thermospheric temperature*

* This chapter needs to be cited as:

Ogunjobi, O., Sivakumar, V., Sivla, W.T., 2014b. A superposed epoch study of the effects of solar wind stream interface events on the upper mesospheric and lower thermospheric temperature. *Advances in Space Research*, in press, doi: 10.1016/j.asr.2014.07.005.

Available online at www.sciencedirect.com

ScienceDirect

Advances in Space Research xxx (2014) xxx–xxx

ADVANCES IN SPACE RESEARCH (a COSPAR publication)

www.elsevier.com/locate/asr

A superposed epoch study of the effects of solar wind stream interface events on the upper mesospheric and lower thermospheric temperature

O. Ogunjobi [a,*], V. Sivakumar [a], W.T. Sivla [b]

[a] School of Chemistry and Physics, University of KwaZulu–Natal, Durban, South Africa
[b] Department of Physics, Kogi State University, Anyigba, Nigeria

Received 26 March 2014; received in revised form 2 July 2014; accepted 7 July 2014

Abstract

The response of mesosphere and lower thermosphere (MLT) temperature to energetic particle precipitation over the Earth's polar regions is not uniform due to complex phenomena within the MLT environment. Nevertheless, the modification of MLT temperatures may require an event-based study to be better observed. This work examines the influence of precipitation, triggered by solar wind stream interfaces (SI) event from 2002 to 2007, on polar MLT temperature. We first test the relationship between the ionospheric absorption measured by the SANAE IV (South African National Antarctic Expedition IV) riometer and the layer of energetic particle precipitation from POES (Polar Orbiting Environmental Satellites). The combined particle measurements from POES 15, 16, 17 and 18 were obtained close in time to the pass of the SABER (Sounding of the Atmosphere using Broadband Emission Radiometry) temperature retrieval. Here, a superposed epoch technique is described and implemented to obtain average temperature profiles during SI-triggered particle precipitation. The superposed epoch average shows no significant temperature decrease below 100 km prior to the onset of SI-triggered precipitation, whereas a clear superposed average temperature decrease is observed at 95 km after the SI impact. A case study of SI event also yields similar observations. Results indicate that cooling effects due to the production of mesospheric odd hydrogen might be major contributors to temperature decrease under compressed solar wind stream.

Keywords: Solar wind stream interface region; Polar MLT temperature; Magnetospheric convection; Superposed epoch analysis

1. Introduction

The MLT (mesosphere (50–100 km) and lower thermosphere (100–180 km)) regions are not fully understood when considering the dynamics of the Earth's upper atmosphere. The complication in understanding the energy and thermal balance ranges from a great number of parameters determining the heating processes to those cooling it (Offermann, 1985). Plasma flow from the sun, energetic particle precipitation, heat conduction, neutral winds, gravity waves breaking and infrared cooling are among the important parameters. These parameters play significant roles in the heating and cooling processes depending on the effective geophysical conditions (Roble, 1995). The level of geophysical activities generally increases during magnetospheric storms. The magnetospheric storms can be fueled by the solar wind streams and consequently drive particles into the Earth's upper atmosphere; this function defines the term geomagnetic storms. During geomagnetic storms, the atmosphere experiences influx of precipitating energetic particles (Rees, 1989). The rate of precipitation

* Corresponding author. Tel.: +27 84 824 2132.
E-mail addresses: olakunle.ukzn@gmail.com (O. Ogunjobi), Venkataramans@ukzn.ac.za (V. Sivakumar), sivlaw@yahoo.com (W.T. Sivla).

http://dx.doi.org/10.1016/j.asr.2014.07.005
0273-1177/

Please cite this article in press as: Ogunjobi, O., et al. A superposed epoch study of the effects of solar wind stream interface events on the upper mesospheric and lower thermospheric temperature. J. Adv. Space Res. (2014), http://dx.doi.org/10.1016/j.asr.2014.07.005

also depends on the solar wind stream structure that triggers the geomagnetic storm. For instance, the bimodal structure of the solar wind streams provides the mechanism for the stream interface (SI) occurrence (Burlaga, 1974).

The slow-speed solar wind streams (SSWS) from the vicinity of streamer belt are constantly at the leading edge of the trailing high-speed solar wind streams (HSSWS) which originate from coronal holes. Due to the Earth's magnetic field, however, both streams cannot mingle. The region that separates these dense, slow-moving plasma from fast, less dense plasma is the SI (Burlaga, 1974; Gosling et al., 1978). SI is a type of storm-driven event (Friedel et al., 2002; Dal Lago et al., 2002) and can trigger precipitation, which might cause significant compositional changes if it interacts with the upper atmospheric constituents. Intuitively, particle precipitation is anticipated to enhance upper atmospheric temperature. Nonetheless, some previous works (for example, Banks, 1977; Offermann, 1985; Jackman et al., 2007; von Savigny et al., 2007; Pancheva et al., 2007) have shown a potential heating effect, an apparent cooling effect or no measurable temperature response to precipitating particles. The apparent inconsistency is probably due to some differences in the solar wind–magnetosphere coupling processes. Here, we focused on just the SI-triggered precipitation effects on the MLT temperature within the period of 2002–2007, the details of which will be presented in Section 2. It should be noted that SI is associated with the corotating interaction region (CIR) and thus recurs (Heber et al., 1999; Borovsky and Denton, 2008, 2009; Morley et al., 2010b). Due to this recurrence nature, according to Borovsky and Denton (2009), SI is amenable to superposed epoch analysis (SEA).

In this study, we have performed SEA on the selected 27 SI-driven storms that occurred from 2002 to 2007. We have investigated the ultimate implications of these events by studying the associated geophysical properties, solar wind conditions and absorption of the precipitating particle. We also examined the MLT temperature changes in response to (or caused by) SI-triggered precipitation over SANAE IV (71.7°S, 2.9°W, $L = 4.32$). Finally, we validated our technique with temperature measurement above 100 km and also with a nightside SI event that occurred on 7 May 2007.

2. Data description and event selection

2.1. TIMED/SABER data

The TIMED (Thermosphere Ionosphere Mesosphere Energetic and Dynamics) satellite was launched on 7 December 2001 into a 625-km circular orbit, with 74.1° inclination. The satellite's orbit period is 102 min. The SABER (Sounding of the Atmosphere using Broadband Emission Radiometry), which is one of the four instruments on-board the TIMED satellite, measures the CO_2 15-μm limb emission, which is useful for estimating the neutral temperatures up to approximately 130 km. In order to maintain the instrument at a certain temperature, SABER obtains temperature profiles from 83°S to 52°N during its south-looking mode for 60 days and then switches to an analogous north-looking mode. Here, we obtain the temperature measurements during SABER's south-looking mode.

TIMED/SABER has been found to be useful and contributes to the validation of assimilative atmospheric models such as the International Reference Ionosphere (IRI, Bilitza et al., 2014). An empirical model of neutral (CIRA-86) temperature published on the IRI-2007 website http://omniweb.gsfc.nasa.gov/vitmo/iri_vitmo.html is employed in this study.

2.2. NOAA/POES data

The NOAA/POES (National Oceanic and Atmospheric Administration/Polar Orbiting Environmental Satellites) is a polar-orbiting, Sun-synchronous, low-altitude (850 km) satellite with a period of approximately 100 min. The satellite has on-board the Medium Energy Proton and Electron Detector (MEPED) and Total Energy Detector (TED), which monitor the intensities of precipitating energetic particles (Rodger et al., 2010). These detectors have up to 30° field of view. POES (15–18) orbit the Earth in such a way that they pass over the poles within the period under study. The MEPED on each satellite provides directional (0° telescopes for precipitating and 90° for trapped) measurements of protons and energetic electrons. At high latitudes, the vertical detector measures the particles in the drift loss cone. During geomagnetic disturbances, trapped energetic particles can enter drift shells located above the upper ionosphere via a loss mechanism. Since the vertical detectors look approximately along the field line, it will only detect precipitating particles.

In this study, data from 0° telescope were selected only when it measures protons and electrons within the loss cone. With POES satellites, our statistical work is organised across all local time such that at any given time, one of the POES satellites provides measurements.

2.3. Riometer data

Remote sensing of electromagnetic waves of cosmic origin is a technique useful in studying the state and the structure of the ionosphere (Hargreaves, 1979). Riometers respond to both the integrated absorption of cosmic ray noise through the ionosphere and electron density at heights where there is a high collision (see, Clilverd et al., 2010). The riometers are mostly widebeam, typically 30 MHz, and sensitive to any incident particle population capable of reaching the altitude range of 70–100 km. In order to identify extraordinary ionospheric absorption from remote measurements, a reference Quiet Day Curve (QDC) value is an important parameter to be considered (Ogunjobi et al., 2014). Any deviations from this expected

Please cite this article in press as: Ogunjobi, O., et al. A superposed epoch study of the effects of solar wind stream interface events on the upper mesospheric and lower thermospheric temperature. J. Adv. Space Res. (2014), http://dx.doi.org/10.1016/j.asr.2014.07.005

value must then be due to absorption in the ionosphere. The riometer absorption during SI event is employed in this study as a robust indicator of precipitation of high-energy particles.

2.4. SEA technique and event selection

The collection of the SI-driven storms used in this study is from the year 2002 to 2007 which is the possible time frame of riometer measurements from SANAE IV. The events are a subset of the solar wind SI found in Varotsou et al. (2008), Simunac et al. (2009), Morley et al. (2010b) and Ogunjobi (2011). Any SI-driven storms that are preceded and/or followed by another interface within 2 days is excluded from the SI collection. This condition is meaningful because such an event is sufficiently close to be considered as a duplicate event or as a result of multiple contributing processes. After imposing this condition, a total of 27 SI-driven storms occur during SABER's south-looking mode. The hourly OMNI database is used to examine the geophysical properties, solar wind conditions and the interplanetary magnetic field (IMF) near the Earth on SI arrival. The OMNI data set from http://omniweb.gsfc.nasa.gov. is created by interspersing, after cross-normalizing, field and plasma measurements at the Earth's Bow Shock Nose (BSN) from each contributing spacecraft (King and Papitashvili, 2005).

The SEA technique, as earlier noted, is one method of composition of time series data. This technique of analysis can apply to large noisy data set so as to reveal a consistent response to some repeatable phenomenon (Chree, 1908; Miyoshi and Kataoka, 2005; Freeman and Morley, 2009; Borovsky and Denton, 2009; Morley et al., 2010b). In this study, time series of the SI parameters are extracted from a window around the epoch and all data at a given time relative to epoch form the sample of events at that lag. The data at each time lag are then averaged so that fluctuations not consistent around the epoch is canceled. The choice of reference (zero epoch) time for SEA are important and could substantially influence the results (Borovsky and Denton, 2009). One major characteristic of SI events on arrival at Earth is the deflection of solar wind azimuthal velocity in GSE (geocentric solar ecliptic) coordinate. Therefore, the zero epoch of the 27 SI was taken at the time when the azimuthal solar wind velocity flow reverses from westward to eastward. Fig. 1 shows an epoch view of solar wind azimuthal velocity for the 27 SI events. The traces for many of the 27 events are overlaid by the other events; hence, only a smaller number of traces are visible in Fig. 1.

3. Observations and analysis

3.1. SEA: geophysical properties of the set of 27 SIs

Fig. 2(a)–(h) presents the superposed measurements of the near-Earth solar wind conditions and geophysical parameters from the OMNI database (King and Papitashvili, 2005). In Fig. 2(a), the superposed average of Kp is plotted. The Kp is a measure of the strength of the solar wind driving the magnetosphere (Thomsen, 2004). Kp is low prior to the arrival of SI while there is a gradual rise that coincides with the SI onset. The Kp in OMNI format is seen to be ramping up from −0.8 days and reaches an average peak of 4+ coinciding at SI onset, which implies an enhanced magnetospheric convection at SI arrival near Earth. The geomagnetic activity remains at a comparatively high level after the arrival for about 3 days. A superposed average of the Dst index as a measure of ring current is shown in Fig. 2 (b). The positive interval prior to the onset of SI indicates weakly driven compressed magnetosphere (e.g, Borovsky and Denton, 2006). At the onset, Dst reverses to a modest average of about −30 nT indicating that the magnetospheric convection is increasing the pressure of the magnetospheric plasmas. Since SI is typically a high-speed stream-driven storm, strong ring current perturbation is not expected (Friedel et al., 2002; Morley et al., 2010b), but the increasing pressure of the plasmas can result in a diamagnetic effect lasting for days (Borovsky and Denton, 2009). The superposed average of the IMF B_z is plotted in Fig. 2(c). The northward IMF B_z interval prior to the onset of SI creates a calm before the storm. There is a sector reversal from north to south on arrival of SI. A southward interplanetary magnetic field will cause the magnetopause to be pushed inward from its stand-off distance (Dmitriev and Suvorova, 2013). During the southward turning of IMF B_z, energetic particles can gain access into the Earth's upper atmosphere due to magnetopause distortion. Prior to the arrival of SI, the solar wind number density in Fig. 2(d) shows compressed slow wind and an average elevation of 17 cm^{-3} at SI onset.

Further evidence of compressed plasma flow at the onset is seen in the superposed average of the solar wind radial velocity (V_x GSE) in Fig. 2(e). Prior to the SI onset is the low wind speed in the range of approximately 400 km/s, which is ramping up near the arrival of SI. At the onset, V_x (GSE) rises to about 550 km/s for over +3 days with high Alfvén Mach number, MA, (Fig. 2(f)). High MA is expected of CIR storm drivers due to high-speed solar wind stream. The solar wind pressure (Fig. 2(g)) is ramping up a few hours prior to SI at Earth and reaches a peak of about 10 nPa on its arrival. The pressure increase on the arrival of SI is a clear indication of the dynamic pressure difference as the fast solar wind overtakes the slow solar wind. So, SSWS is compressed prior to the SI onset and HSSWS is compressed after the onset.

The plasma compression from the SI onset, controlled by the electric field and the new temperature gradients, can alter the neutral atmosphere, and can ultimately affect the temperature of the upper atmosphere. Nevertheless, the outcomes of such effects on MLT temperature observations are yet to be completely understood. The solar wind azimuthal velocity (GSE-V_y is presented in Fig. 2(h). The superposed average of GSE-V_y reverses from an average of −12 km/s to +19 km/s on arrival of SI. The point where

Please cite this article in press as: Ogunjobi, O., et al. A superposed epoch study of the effects of solar wind stream interface events on the upper mesospheric and lower thermospheric temperature. J. Adv. Space Res. (2014), http://dx.doi.org/10.1016/j.asr.2014.07.005

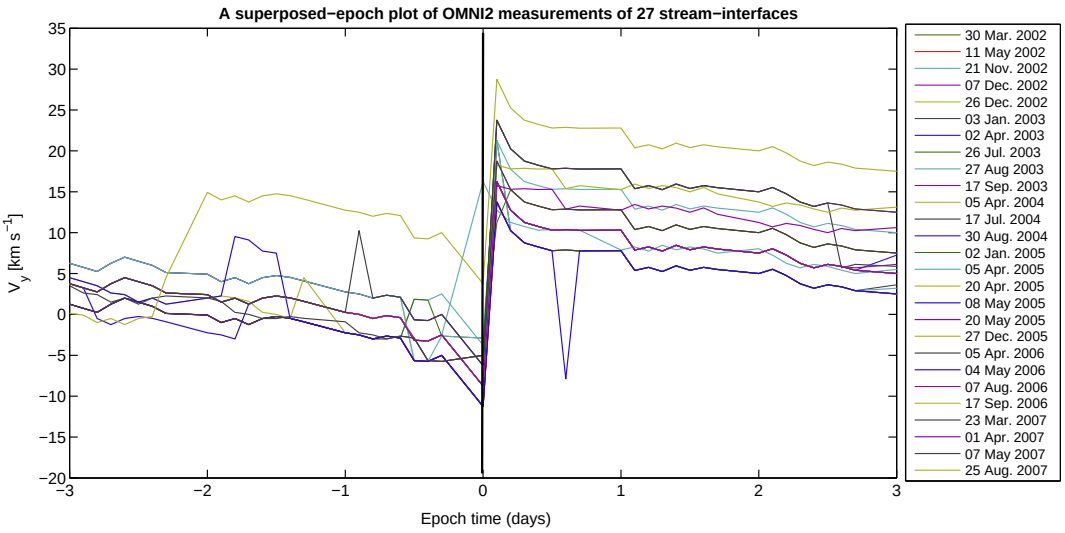

Fig. 1. The solar wind azimuthal velocity (GSE-V_y) for set of the 27 SI.

the V_y flow reverses from westward to eastward through zero is the SI.

These observations represent, perhaps, an increased ring current particle density via an enhanced magnetospheric convection which might result in particle precipitation.

3.2. SEA: particle precipitation during SI-driven storms

Using measurements from the MEPED instruments onboard NOAA 15, 16, 17 and 18, we examine particle precipitation over the vicinity of SANAE IV at several periods of time. The precipitating particle measurement is projected down to around 100 km which is near the foot of the magnetic field line, and then sorted over ±4° and ±10° latitude and longitude, respectively. Due to an increase in data points, a linear interpolation technique is employed (Fang et al., 2007).

Prior to the period of increased magnetospheric convection, there is no significant precipitation with only an average of 10^0 cm^{-2} s^{-1} sr^{-1} flux for >30 and >100 keV electrons as seen in Fig. 3 (upper panel), whereas an abrupt slower decaying peak (up to 10^6 cm^{-2} s^{-1} sr^{-1}) is seen on arrival until 0.5 days. With the magnetopause possibly having been stripped off, the energetic particles can gain access into the MLT region. The sharp peak in precipitating electron flux on arrival of the SI coincides with the time of enhanced magnetospheric activities and plasma flow presented in Fig. 2. This SEA characteristic of the electron fluxes is also observed for a proton energy of 80–240 keV and 240–800 keV, as seen in Fig. 3 (bottom panel). Generally, the energetic particle precipitation does not regress to the pre-event level with the return of the IMF B_z from southward to northward. This may be interpreted as a non-adiabatic effect. A non-adiabatic response means that there is a real loss of energetic particles from the 'outer radiation belt' and eventual precipitation into the upper atmosphere. Precipitation associated with this type of event confirms the expectation of Tsurutani and Lakhina (1997). It is expected that at the storm recovery phase, any interaction involving the so-called 'whistler mode waves' and outer radiation belt particles is capable of scattering energetic particles into the drift loss cone. Particles from the drift loss cone may result in ring current decay and perhaps affect the MLT compositions.

3.3. SEA: absorption and deposition during SI triggered precipitation

Given the interpolation mentioned earlier, the correlation between absorption measurements over the region of interest and the fluxes retrieved from the NOAA satellites can only be qualitative. Nevertheless, the riometer observation can be used to quantify any possible effects caused by intense particle precipitation in the ionospheric D-region (~90 km).

Fig. 4 shows the superposed average of cosmic radio noise absorption from the SANAE IV riometer. The superposed average of the absorption rate is seen to be approximately half an order of magnitude higher than the pre-event level. The absorption peaks for >3 h after the SI impact. The superposed average from the riometer shows that SI-triggered precipitation reaches the MLT altitude. This indicates a probable link between the dominant mechanism acting during precipitation and the resulting atmospheric heating or cooling. This will be the subject for a future study. However, the absorption due to SI-triggered precipitation further confirms an enhanced magnetospheric convection.

We consider the energy deposition height profile using the Monte Carlo Energy Transport model (MCTEM, Ogunjobi et al., 2014). Fig. 5 presents the energy deposition height profile due to the precipitating particles in the vicinity of SANAE IV. Fig. 5(a)–(d) shows that the superposed average of energy deposition increases around the time of

Please cite this article in press as: Ogunjobi, O., et al. A superposed epoch study of the effects of solar wind stream interface events on the upper mesospheric and lower thermospheric temperature. J. Adv. Space Res. (2014), http://dx.doi.org/10.1016/j.asr.2014.07.005

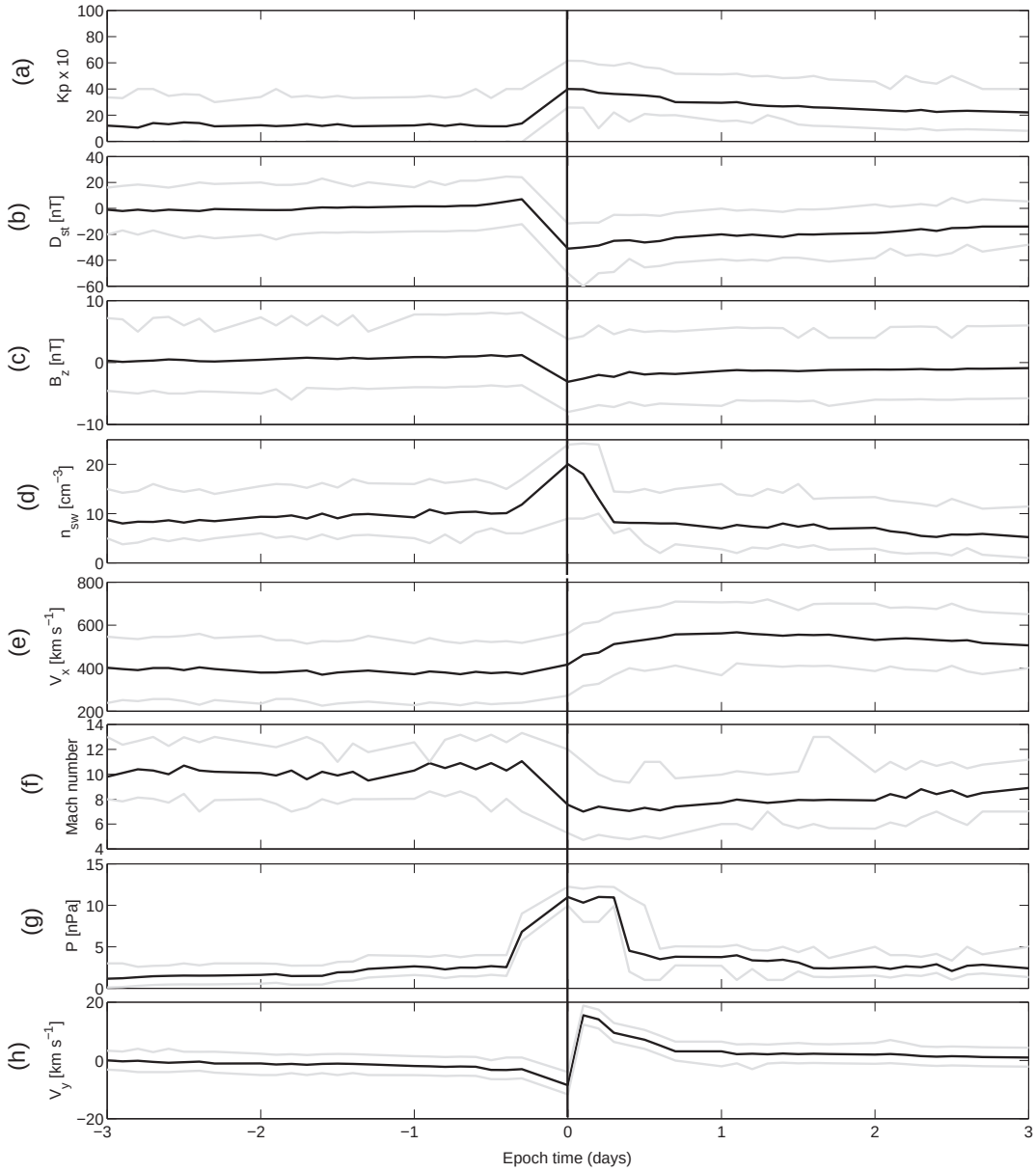

Fig. 2. Plots of superposed properties of SIs used: in each panel, the grey lines are the upper and lower quartiles while black line indicates the average. From top is Kp, Dst, IMF B_z, solar wind number density, solar wind radial velocity V_x, Alfvén Mach number, solar wind pressure and the solar wind azimuthal (V_y, east–west) flow velocity. The trigger for the data superposition (epoch = 0) is the time at which the sense of the eastwest flow deflection reversed.

SI (which indicates the precipitation of high energy particles). The rate of energy deposition is increased and peaks around 90 km altitude immediately after SI arrival. The energy deposition at mesospheric height remains elevated until approximately 3 h after SI impact and gradually returns to pre-event level at 6 h later.

3.4. SEA: corresponding temperature modification

From the geophysical and solar wind conditions, it is apparent that the SI-triggered energetic particle precipitation ultimately results in energy deposition in mesospheric heights. In view of this, the temperature measurement from SABER is obtained in the area where MEPED measures particle precipitation. It should be recalled that particle measurement over SANAE IV is projected down to about 100 km which is near the foot of the magnetic field line, and sorted over ±4° latitude and ±10° longitude. In order to have more realistic temperature estimates, we ensure that SABER measurements are taken immediately after the NOAA/POES satellite pass. Also with SEA, we expect only temperature changes that coincide with the SI-particle precipitation. Fig. 6 presents the average temperature profiles during the SI event.

Prior (−6 h) to the event as seen in Fig. 6(a) and (b) there is no significant temperature decrease below 100 km,

Please cite this article in press as: Ogunjobi, O., et al. A superposed epoch study of the effects of solar wind stream interface events on the upper mesospheric and lower thermospheric temperature. J. Adv. Space Res. (2014), http://dx.doi.org/10.1016/j.asr.2014.07.005

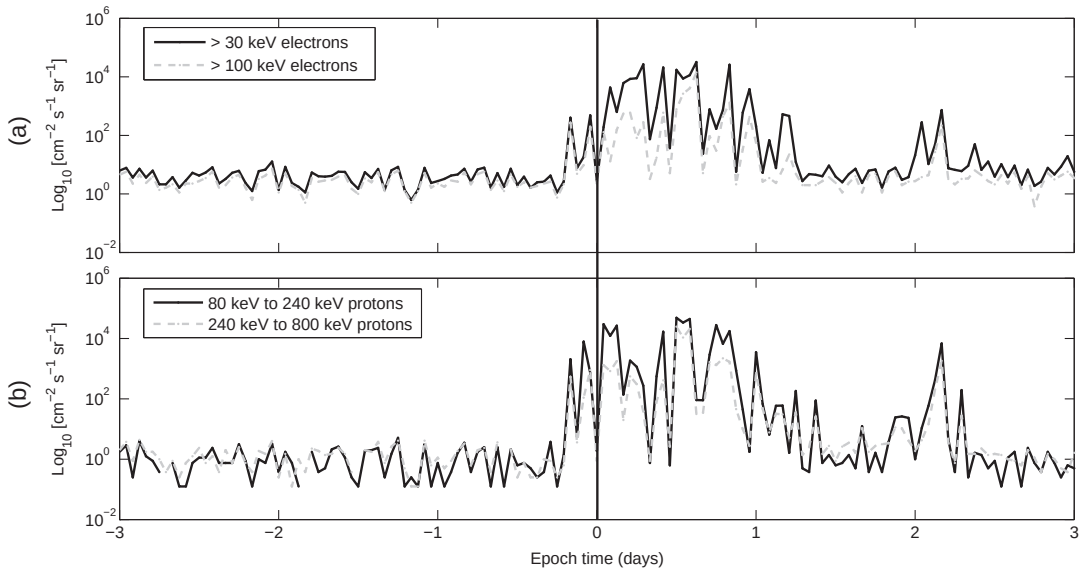

Fig. 3. Averaged NOAA/POES electrons (top panel) and protons (bottom) precipitation on arrival of SI. The zero epoch taken as the SI onset time (i.e., V_y reversal) is indicated by a vertical line.

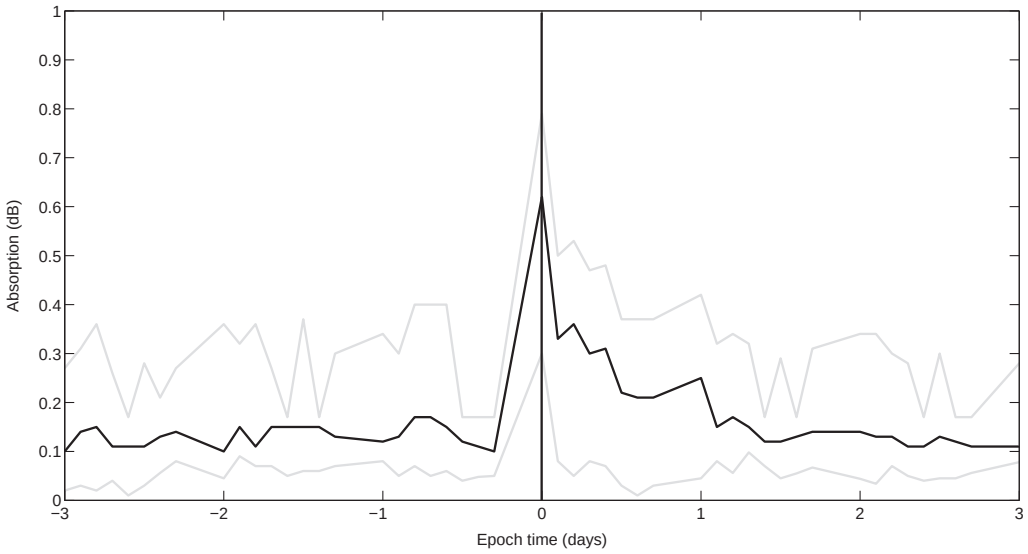

Fig. 4. Superposed epoch of SANAE IV riometer absorption during SI-triggered precipitation. The grey lines are the third quartile and first quartile while the black line indicates the average, with the zero epoch taken as the onset time of V_y reversal indicated by the vertical line.

whereas at the SI onset (Fig. 6(c)) until +6 h afterward (Fig. 6(d)) we observe a superposed average temperature decrease of approximately 35 K around 95 km. The superposed average temperature characteristics at 95 km correlates with the abrupt peaks seen during particle precipitation and absorption on SI arrival. Previous work by Pancheva et al. (2007) also found a temperature decrease of about 25 K below 100 km associated with a geomagnetic storm in the Northern hemisphere. This implies that particle precipitation has perhaps affected the neutral chemistry of the MLT via ionisation. According to Solomon et al. (1981), the direct impact of energetic particles on mesosphere constituents will include not only reaction to form odd nitrogen (NOx) but also induced production and recombination of water cluster ions to produce odd hydrogen (HOx). The production of HOx can cause mesospheric cooling (e.g. Rusch et al., 1981; Damiani et al., 2010). Grenfell et al. (2006) found HOx to be an important contributing catalyst in ozone loss reactions in the mesospheric region. Ozone itself is significant in the absorption of solar ultraviolet radiation and thus may affect the radiative balance, temperature and dynamics of the atmosphere. While our observations of the cooling effect below 95 km is similar to Pancheva et al. (2007), it is however not fully consistent with the work of von Savigny et al. (2007), Jackman et al. (2007) and Ogunjobi et al. (2014).

Please cite this article in press as: Ogunjobi, O., et al. A superposed epoch study of the effects of solar wind stream interface events on the upper mesospheric and lower thermospheric temperature. J. Adv. Space Res. (2014), http://dx.doi.org/10.1016/j.asr.2014.07.005

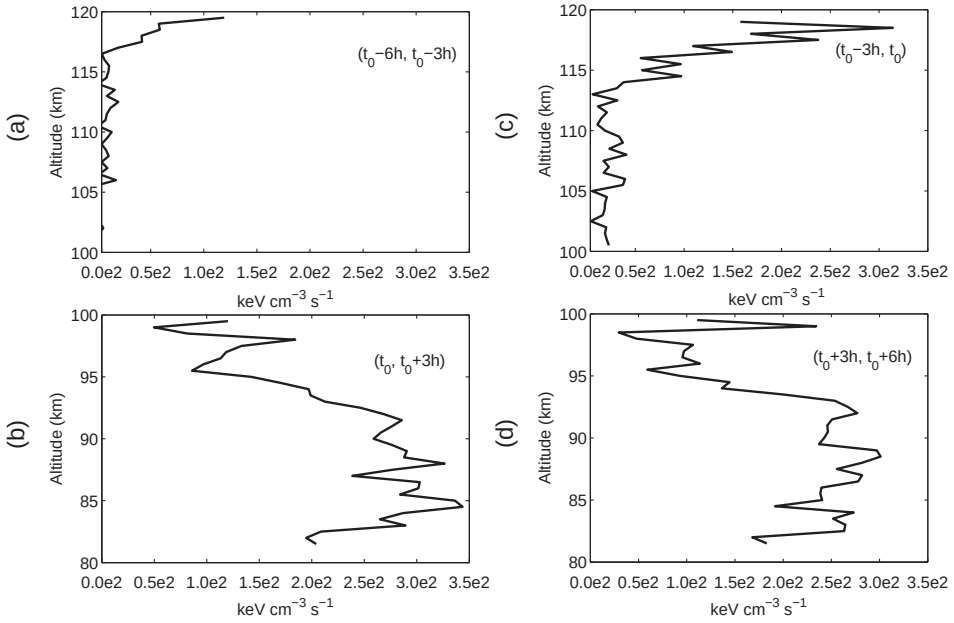

Fig. 5. Superposed epoch of energy deposition height profiles estimated based on the electron and proton spectra from MCTEM.

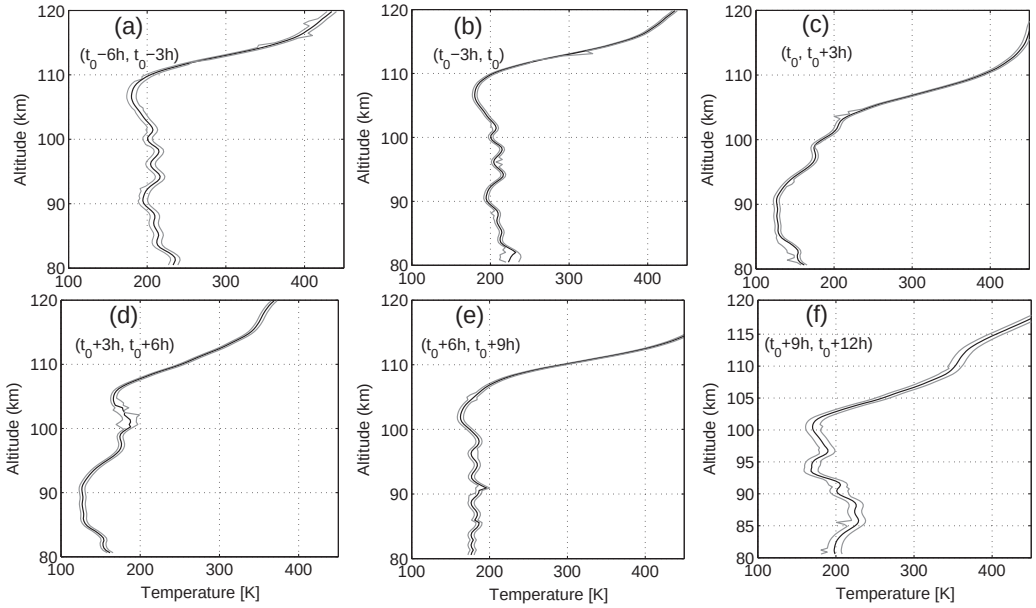

Fig. 6. Superposed epoch average of SABER temperatures associated with SI-triggered precipitation.

In the observational work of von Savigny et al. (2007), a temperature increase of a few K/d was observed around 90 km during solar proton event (SPE). The model of Jackman et al. (2007) shows a small heating effect of 2–3 K in the Southern hemisphere while there is no significant response in the Northern hemisphere during an SPE event. A heating effect was also found below 100 km in the Southern hemisphere in a recent case study by Ogunjobi et al. (2014) for a different type of storm-driven event known as magnetic cloud (MC). The apparent contradictory temperature responses demonstrate the complexity of the energy budget in the MLT region. It might be that, within each of these structures (MC, SPE and SI), the magnetic fields are of fundamentally different origin and the solar wind parameters that control the solar wind–magnetosphere coupling might also have different behaviour. Another plausible explanation is hemispherical differences in the observable locations.

In the recovery phase (Fig. 6 (e) and (f)), the temperature response to an SI-triggered precipitation shows a gradual return to pre-event level from 9 h after the SI onset. The return of temperature to a pre-event level shows that the precipitation indeed plays a substantial part in temperature changes. Generally, we find a temperature increase

Please cite this article in press as: Ogunjobi, O., et al. A superposed epoch study of the effects of solar wind stream interface events on the upper mesospheric and lower thermospheric temperature. J. Adv. Space Res. (2014), http://dx.doi.org/10.1016/j.asr.2014.07.005

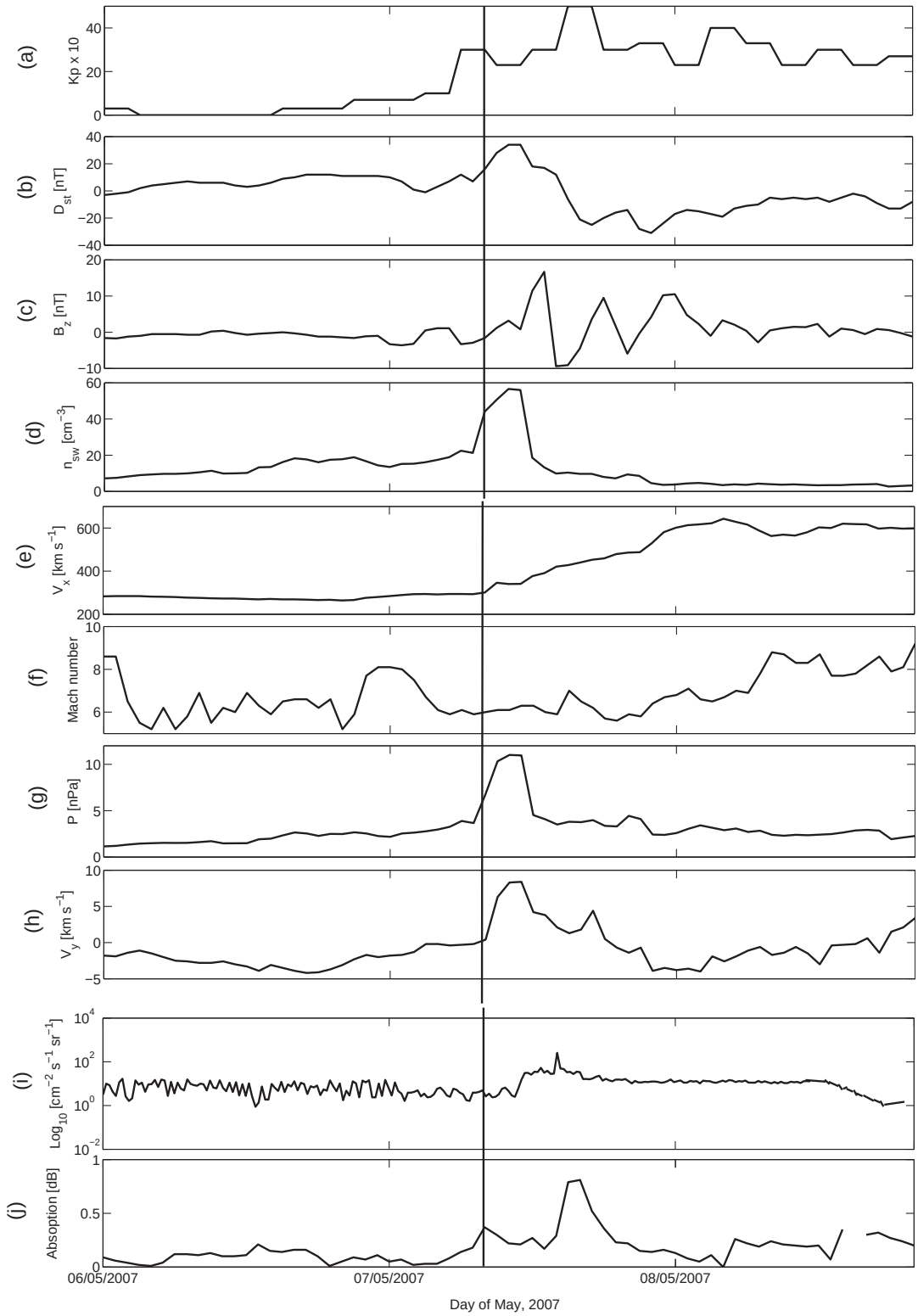

Fig. 7. Geophysical parameters and activities on 7 May 2007 SI-driven storm. From (a)–(j) are Kp index, Dst index, BZ (GSM), solar wind number density, solar wind radial velocity, Alfvén Mach Number, solar wind pressure and the solar wind azimuthal (west–east) flow velocity, >30 keV electrons precipitation and absorption from riometer. The vertical line indicates the onset of SI.

associated with SI-triggered precipitation at ~110 and 120 km. An increase in dynamic pressure at SI arrival (Fig. 2(g) is an indication that the magnetopause may be closer to the Earth, resulting in the loss of magnetospheric particles through the 'magnetopause shadowing'. The resultant heating due to magnetospheric convection

Please cite this article in press as: Ogunjobi, O., et al. A superposed epoch study of the effects of solar wind stream interface events on the upper mesospheric and lower thermospheric temperature. J. Adv. Space Res. (2014), http://dx.doi.org/10.1016/j.asr.2014.07.005

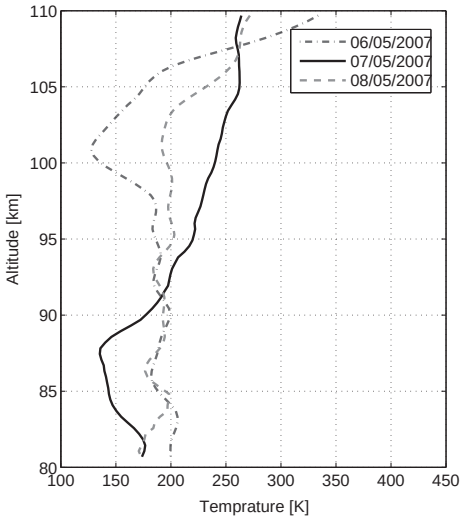

Fig. 8. Average temperatures associated with >30 keV electron fluxes on 7 May 2007 SI-triggered precipitation. The dashed–dotted, solid and dashed lines present temperatures measured on 6, 7 and 8 May 2007, respectively.

together with Joule heating might be the major contributors to the observed temperature increase at ~110 and 120 km. According to Banks (1977), enhanced heating rates of about 40 k/h is not unusual at 120-km altitude due to accumulated Joule heating. Although SI-triggered precipitation is just a single parameter in a system of multiple variables, an SEA on a large number of measurements may average out the effects of some of the other parameters, such as tides and gravity waves. One other possible reason for the apparent contradiction in temperature responses might be the sunlit condition, which might affect the temperature estimate in the SEA. Thus, it is necessary to validate the SEA technique using temperature measurements on the nightside. This can be achieved by analysing a nightside SI event.

3.5. A case study on 7 May 2007 SI event

An SI event arrives near at about 1430 UTC on 7 May 2007. Using global positioning system (GPS) satellites, Morley et al. (2010a) had examined earlier the time scale of the particle precipitation from the outer radiation belt during this event. However, the ultimate effect that such a particle could have on mesospheric dynamics is yet to be studied, although it is not all the particles that drop out of the trapped radiation belt that will precipitate onto the polar atmosphere. We, however, find this event in the list of our epoch collections and it is regarded here as a special event as it allows useful validation of SEA.

Using the OMNI data (King and Papitashvili, 2005), we obtain the geophysical parameters during the SI event on 7 May 2007 as presented in Fig. 7(a)–(h). Similar to the events in Fig. 1, storm activities are relatively low prior to the SI arrival. Most important of these is a peak in solar wind dynamic pressure on the arrival which again indicates inward movement of the magnetopause. The precipitation of >30 keV of electrons shows an abrupt peak (similar to SEA) on SI arrival as can be seen in Fig. 7(i). Electrons above 30 keV can penetrate to <105 km (Lam et al., 2010). This is confirmed using a SANAE IV riometer. A significant peak in absorption is seen over SANAE IV on arrival of SI as presented in Fig. 7(j).

We examine the SABER temperature measurement on the nightside (18–06 LT), at exactly the same height and spatial location with NOAA/POES. During the Southern winter season (this case), we expect influence from diurnal variation which needs to be accounted for. Fig. 8 presents an average vertical temperature profile centered on a day of SI. Similar to SEA, an increase in temperature is generally seen above 105 km. Prior to the SI arrival, there was no significant average temperature decrease below 100 km, whereas at the event's onset, we find an apparent average

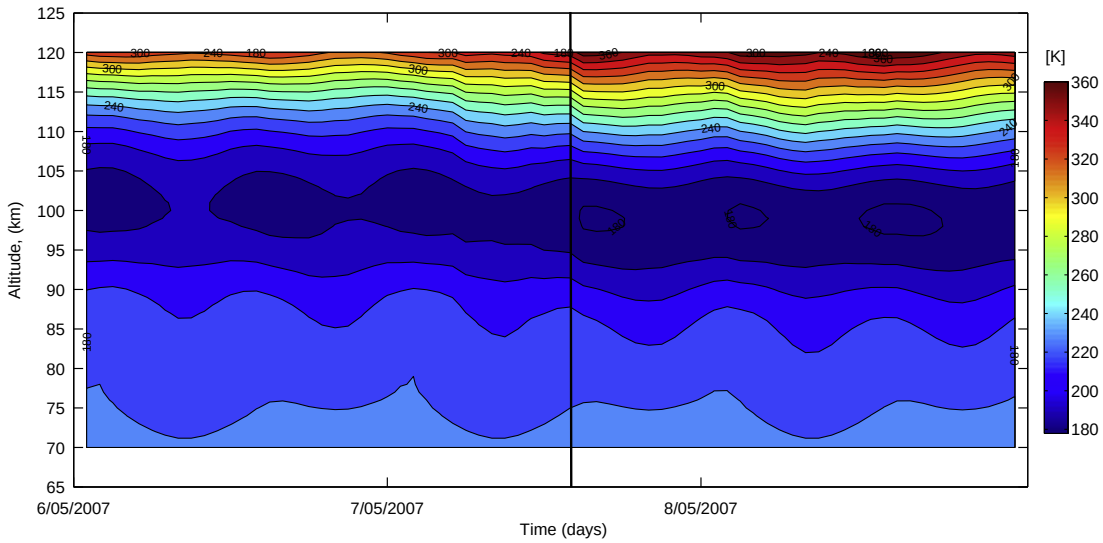

Fig. 9. Contour plots of CIRA-86 neutral temperature (published in IRI-2007 model) on 6, 7 and 8 May 2007. The vertical line indicates SI onset.

Please cite this article in press as: Ogunjobi, O., et al. A superposed epoch study of the effects of solar wind stream interface events on the upper mesospheric and lower thermospheric temperature. J. Adv. Space Res. (2014), http://dx.doi.org/10.1016/j.asr.2014.07.005

temperature decrease of approximately 30 K below 90 km. We attribute this temperature decrease to HOx production processes initiated by direct particle impact on mesosphere composition. Again, the temperature profile is seen to have returned to pre-event level a day after the SI. Compared with the IRI model (Fig. 9), the tendency for decreased temperature below 100 km can also be seen near the SI impact. At SI arrival, we observe significant cooling below 100 km. It should be noted that SABER temperature measurements are retrieved in the area of >30 keV electron precipitation. Therefore, we do not expect perfect correlation between SABER temperature profile and the CIRA-86 model of neutral temperatures.

4. Summary and conclusion

We have performed an SEA study on 27 SI-driven storms. Data from SABER on-board the TIMED satellite provide unique information on MLT temperature in the area of SI-triggered precipitation measured by NOAA/POES. Generally, we find a significant superposed average temperature enhancement at 110 and 120 km. Prior to SI onset, there is no significant temperature decrease below 100 km, whereas at the onset of the SI-triggered precipitation, we observe an immediate superposed average temperature decrease of about 35 K around 95 km. We continue to observe a temperature decrease at 95 km until over 6 h after the SI impact and gradual return to pre-event level between 9 and 12 h later. To further validate the SEA observations, we examined a nightside SI event on 7 May 2007. Similar to the SEA observations, we find a temperature reduction of approximately 30 K around 95 km related to >30 keV electron precipitation at SI onset.

From these observations, we suggest that the heating due to enhanced magnetospheric convection together with Joule heating might be the major contributors to the observed temperature increase at ~110 and 120 km, while the decrease around 95 km might be as a consequence of the mesospheric cooling effects during HOx production processes.

The SI-triggered precipitation investigated in the present study all occurred during compressed, high-speed-stream-driven storms. The MLT temperature changes can be studied under different magnetospheric conditions. In particular, coronal mass ejection (CME)-driven storms will be of great interest to confirm or modify the suggestions of the present study.

Acknowledgements

The authors are thankful for the availability of the geophysical parameters in OMNI database and the CIRA-86 neutral temperature (published in IRI-2007 model) provided by the GSFC/SPDF at OMNIWeb interface, the NOAA/POES at NGDC. The authors express thanks for the support of South African National Antarctic Program (SANAP) and logistics of South Africa National Space Agency (SANSA) in providing SANAEIV riometer data. In addition, the authors also express thanks to ASR anonymous reviewers for their valuable comments and suggestions. Research is supported by SANSA.

References

Banks, P.M., 1977. Observation of Joule and particle heating in the auroral zone. J. Sol. Terr. Phys. 39, 179–193.

Bilitza, D., Altadill, D., Zhang, Y., et al., 2014. The international reference ionosphere 2012 – a model of international collaboration. J. Space Weather Space Clim. 4, A07.

Borovsky, J.E., Denton, M.H., 2006. Differences between CME-driven storms and CIR-driven storms. J. Geophys. Res. 111, A07S08.

Borovsky, J.E., Denton, M.H., 2008. A statistical look at plasmapheric drainage plume. J. Geophys. Res. 113, A09221.

Borovsky, J.E., Denton, M.H., 2009. Relativistic-electron dropouts and recovery: a superposed epoch study of the magnetosphere and the solar wind. J. Geophys. Res. 114, A02201.

Burlaga, L.F., 1974. Interplanetary stream interfaces. J. Geophys. Res. 79, 3717–3725.

Chree, C., 1908. Magnetic declination at Kew observatory, 1890–1900. Philos. Trans. R. Soc. Lond. A, 205–246.

Clilverd, M.A., Rodger, C.J., Gamble, R.J., Ulich, T., Raita, A., Seppälä, A., Green, J.C., Thomson, N.R., Sauvaud, J.A., Parrot, M., 2010. Ground-based estimates of outer radiation belt energetic electron precipitation fluxes into the atmosphere. J. Geophys. Res. 115, A12304.

Dal Lago, A., Gonzalez, W.D., Gonzalez, A.L.C., Vieira, L.E.A., 2002. Stream-interacting magnetic clouds causing very intense geomagnetic storms. Adv. Space Res. 30, 2225–2229.

Damiani, A., Storini, M., Santee, M.L., Wang, S., 2010. Variability of the nighttime OH layer and mesospheric ozone at high latitudes during winter: influence of meteorology. Atmos. Chem. Phys. 10, 10291–10303.

Dmitriev, A.V., Suvorova, A.V., 2013. The shape of strongly disturbed dayside magnetopause. Terr. Atmos. Oceanic Sci. 24, 225–232.

Fang, X., Liemohn, M.W., Kozyra, J.U., Evans, D.S., DeJong, A.D., Emery, B.A., 2007. Global 30–240 keV proton precipitation in the 17–18 April 2002 geomagnetic storms: 1. Patterns. J. Geophys. Res. 112, A05301.

Freeman, M.P., Morley, S.K., 2009. No evidence for externally triggered substorms based on superposed epoch analysis of IMF Bz. Geophys. Res. Lett. 36, L21101.

Friedel, R.H.W., Reeves, G., Obara, T., 2002. Relativistic electron dynamics in the inner magnetosphere – a review. J. Atmos. Sol. Terr. Phys. 64, 265.

Gosling, J.T., Asbridge, J., Bame, S., Feldman, W., 1978. Solar wind stream interfaces. J. Geophys. Res. 83, 1401.

Grenfell, J.L., Lehmann, R., Mieth, P., Langematz, U., Steil, B., 2006. Chemical reaction pathways affecting stratospheric and mesospheric ozone. J. Geophys. Res. 111, D17311.

Hargreaves, J.K., 1979. The Upper Atmosphere and Solar Terrestrial Relations. Van Nostrand Reinhold, New York.

Heber, B., Sanderson, T.R., Zhang, M., 1999. Corotating interaction regions. Adv. Space Res. 23, 567–579.

Jackman, C.H., Roble, R.G., Fleming, E.L., 2007. Mesospheric dynamical changes induces by the solar proton events in October–November 2003. Geophys. Res. Lett., 34.

King, J., Papitashvili, N., 2005. Solar wind spatial scales in and comparisons of hourly wind and ACE plasma and magnetic field data. J. Geophys. Res. 110, A02209.

Lam, M.M., Horne, R.B., Meredith, N.P., Glauert, S., Moffat-Griffin, T., Green, J.C., 2010. Origin of energetic electron precipitation >30 keV into the atmosphere. J. Geophys. Res. 115, A00F08.

Miyoshi, Y., Kataoka, R., 2005. Ring current ions and radiation belt electrons during geomagnetic storms driven by coronal mass ejections and corotating interaction region. Geophys. Res. Lett. 32, L21105.

Please cite this article in press as: Ogunjobi, O., et al. A superposed epoch study of the effects of solar wind stream interface events on the upper mesospheric and lower thermospheric temperature. J. Adv. Space Res. (2014), http://dx.doi.org/10.1016/j.asr.2014.07.005

Morley, S.K., Friedel, R.H.W., Cayton, T.E., Noveroske, E., 2010a. A rapid, global and prolonged electron radiation belt dropout observed with the global positioning system constellation. Geophys. Res. Lett. 37, L06102.

Morley, S.K., Friedel, R.H.W., Spanswick, E.L., Reeves, G.D., Steinberg, J.T., Koller, J., Cayton, T., Noveroske, E., 2010b. Dropouts of the outer electron radiation belt in response to solar wind stream interfaces: global positioning system observations. Proc. R. Soc. 466, 3329–3350.

Offermann, D., 1985. The energy budget campaign 1980. J. Atmos. Terr. Phys. 47, 1–26.

Ogunjobi, O., 2011. Outer electron radiation belt dropouts: geosynchronous and ionospheric responses. Master's thesis. School of Chemistry and Physics.

Ogunjobi, O., Sivakumar, V., Mbatha, N., 2014. A case study of energy deposition and absorption by magnetic cloud electrons and protons over the high latitude stations: effects on the mesosphere and lower thermosphere. Terr. Atmos. Oceanic Sci. 25, 219–232.

Pancheva, D., Singer, W., Mukhatrov, P., 2007. Regional response of the mesosphere-lower thermosphere dynamics over Scandinavia to solar proton events and geomagnetic storms in late October 2003. J. Sol. Terr. Phys. 69, 1075–1094.

Rees, M.H., 1989. Physics and Chemistry of the Upper Atmosphere. Cambridge University Press, Cambridge.

Roble, R.G., 1995. Energetics of the mesosphere and thermosphere. The Upper Mesosphere and Lower Thermosphere: A Review of Experiment and Theory, vol. 87. AGU, Washington D.C, pp. 1–21.

Rodger, C.J., Clilverd, M.A., Green, J.C., Lam, M.M., 2010. Use of POES SEM-2 observations to examine radiation belt dynamics and energetic electron precipitation into the atmosphere. J. Geophys. Res. 115, A04202.

Rusch, D.W., Gerard, J.-C., Solomon, S., Crutzen, P.J., Reid, G.C., 1981. The effect of particle precipitation events on the neutral and ion chemistry of the middle atmosphere – I. Odd nitrogen. Planet Space Sci. 29, 767–774.

Simunac, K.D.C., Kistler, L.M., Galvin, A.B., et al., 2009. In situ observations of solar wind stream interface evolution. Sol. Phys. 259, 323–344.

Solomon, S., Rusch, D.W., Gerard, J.C., Reid, G.C., Crutzen, P.J., 1981. The effect of particle precipitation events on the neutral and ion chemistry of the middle atmosphere: II. Odd hydrogen. Planet Space Sci. 8, 885–893.

Thomsen, M.F., 2004. Why Kp is such a good measure of magnetospheric convection. Space Weather 2, S11004.

Tsurutani, B.T., Lakhina, G.S., 1997. some basic concepts of wave-particle interactions in collisionless plasmas. Rev. Geophys. 35, 491–502.

Varotsou, A., Friedel, R., Reeves, G., Lavraud, B., Skoug, R., Cayton, T., Bourdarie, S., 2008. Characterization of relativistic electron flux rise times during the recovery phase of geomagnetic storms as measured by the NS41 GPS satellite. J. Atmos. Sol. Terr. Phys. 70, 1745–1759.

von Savigny, S., Sinnhuber, M., Bovensmann, H., Burrows, M.B., Schwartz, M., 2007. On the disappearance of noctilucent clouds during the January 2005 Solar proton events. Geophys. Res. Lett..

Please cite this article in press as: Ogunjobi, O., et al. A superposed epoch study of the effects of solar wind stream interface events on the upper mesospheric and lower thermospheric temperature. J. Adv. Space Res. (2014), http://dx.doi.org/10.1016/j.asr.2014.07.005

Chapter 5

Long term observations of polar mesosphere summer echoes observed by SuperDARN SANAE HF radar in Antarctica*

* This chapter needs to be cited as:

Ogunjobi, O., Sivakumar, V., Stephenson, J. A. E., 2014c. Long term observations of polar mesosphere summer echoes observed by SuperDARN SANAE HF radar in Antarctica. *Advances in Space Research*, in review (Journal Ref. ASR–D–14–00464).

Long term observations of polar mesosphere summer echoes observed by SuperDARN SANAE HF radar in Antarctica

O. Ogunjobi*, V. Sivakumar, J. A. E. Stephenson

School of Chemistry and Physics, University of KwaZulu–Natal, Durban, South Africa

Abstract

Using SuperDARN (Super Dual Auroral Radar Network) HF radar, we report the long term trends and variations of Polar Mesosphere Summer Echoes (PMSE) over SANAE IV (South African National Antarctic Expedition IV). An extraction algorithm is implemented to obtain SuperDARN–PMSE during the summer from 1998 to 2007. The SuperDARN–PMSE occurrence probability rate in relation to the mesospheric neutral winds and temperature are also studied and presented in this paper. The SuperDARN–PMSE occurrence on day–to–day scale show predominantly diurnal variations, a broader maximum peak at local noon and distinct minimum at midnight. The SuperDARN–PMSE occurrence is high in the summer solstice with an insignificant interannual variability in the shape of the seasonal curves. The SuperDARN–PMSE peaks coincide with lower summer mesopause temperature and higher geomagnetic activity. Analysis of the neutral wind variations indicates the importance of pole to pole mesospheric transport circulations in SuperDARN–PMSE occurrence rates.

Keywords: PMSE, SANAE IV, SuperDARN radar, Neutral winds, MLT Temperatures

1. Introduction

It has been known that from November to February in the southern hemisphere, lower temperatures (< 130 K, Lübken et al., 2004) are usually found at polar latitudes mesopause (about 90–100 km altitudes). This enables the charging ice particles from water vapor to grow at mesopause. The interactions of the charged ice particle and mesospheric air turbulence, initiated by propagating gravity waves, results in strong radar backscatter echoes (bragg's scattering) in the high–latitude summer mesosphere (Rapp and Lübken, 2004). Ecklund and Balsley (1981) had earlier refereed to such strong radar echoes as Polar Mesosphere Summer Echoes (PMSE). In the past few years, the PMSE have been closely linked to visible ice particles below 90 km altitude, known as Noctilucent Clouds (NLC) (Cho, 1997; Rapp and Lübken, 2004; Smirnova et al., 2010).

The NLC and PMSE phenomena arise from the formation of ice particles in the low temperatures of the polar summer mesopause. NLC in particular have been suspected to be, perhaps,

*Corresponding author. Tel.: +27 84 824 2132.

Email addresses: olakunle.ukzn@gmail.com (O. Ogunjobi), venkataramans@ukzn.ac.za (V. Sivakumar), stephens@ukzn.ac.za (J. A. E. Stephenson)

Preprint submitted to Advances in Space Research

a good index of global change in the middle atmosphere (For example, Thomas and Olivero, 2001). It has been suggested, nevertheless, that NLC and PMSE are comparatively different in their manifestations. NLC indicate only the presence of thin water–ice particles, formed at a low summer mesopause temperature, between 120 to 150 K (Hervig et al., 2009), while PMSE exist because the electrically charged ice particles (on the scale of Bragg's wavelength) reduce the mobility of free electrons (see, Röttger, 1994; Rapp and Lübken, 2004). Thus, the phenomena of PMSE formation can be ascribed to both ionospheric plasma condition and the thermal variations in the mesosphere. Also, PMSE observations with radar have the advantage of being continuous, unlike NLC which depends on the observer and weather conditions (in the case of 'lidar' usage). Thus, in an alternative to NLC, PMSE observations might contribute to the understanding of Polar mesospheric temperature changes (Huaman and Balsley, 1999; Lübken et al., 2004). Although PMSE have been examined for over three decades, aspects revealed by various instruments are still expected in this field.

Over the last 3 decades, incoherent VHF radars have been found to be a useful tool in studying PMSE characteristics in relation to neutral winds, particle precipitation, mesopause temperatures and cosmic noise absorption (Ecklund and Balsley, 1981; Kirkwood, 1993; Palmer et al., 1996; Hoffmann et al., 1999; Rapp and Lübken, 2004; Klekociuk et al., 2008). However, these studies are mostly concentrated in the Arctic region. Thus, the characteristics of PMSE and its aspect from various instruments in the Antarctic are yet to be entirely realised. However, efforts to complement the VHF observation of PMSE are now being addressed with coherent HF Super Dual Auroral Radar Network (SuperDARN) (e.g, Ogawa et al., 2004; Hosokawa et al., 2005; Liu et al., 2013). Using data from Syowa East HF radar in the Antarctic (during 1999/200 and 2000/2001 summers) and Iceland HF radar in the Arctic (1999 and 2000 summers), Hosokawa et al. (2005) observed a predominant diurnal PMSE variation and a weaker interhemispheric asymmetry of PMSE occurrence than those earlier reported results based on VHF radars. Even so, they noticed possible contamination from ionospheric E–region echoes. In order to avoid contamination from ionospheric echoes, Liu et al. (2013) extracted PMSE from SuperDARN Zhongshan HF radar in Antarctica (2010–2012 summer) when Kp $\leq$ 1. In a keen contrast to Hosokawa et al. (2005), Liu et al. (2013) found a semidiurnal variation of PMSE. This special diurnal characteristics of PMSE from Zhongshan was attributed to the influence of auroral particle precipitation.

During maximum solar activity, energetic particle precipitation and levels of extreme ultraviolent (EUV) radiation could be high. It is however expected that solar quiet time electrodynamics of the Mesosphere and Lower Thermosphere (MLT) region might be driven mainly by tides and gravity waves propagating upward from their source regions in the lower atmosphere (Richardson et al., 2001). Here, we have analysed PMSE observations during maximum and minimum phases of solar cycle to add valuable insights in this field.

This paper presents first long term observations of PMSE with SuperDARN SANAE IV (71.68°S, 2.85°W) HF radar (hereafter referred as SuperDARN–PMSE) over the period 1998–2007. The seasonal, diurnal and interannual characteristics of SuperDARN–PMSE are determined and presented in the results and analysis section. We have examined the SuperDARN–

PMSE occurrence rate in relation to geomagnetic activity and flow of mesospheric winds measured by meteor radar. Furthermore, the temperature changes in relation to SuperDARN–PMSE have been studied.

2. Instrumentation and data analysis

2.1. SUPERDARN SANAE IV Radar

Data from the SuperDARN SANAE IV radar is employed in this study. The antenna array consists of 16 antennae, which are operated as a phased array having 170° boresite. The radar uses approximately 12 MHZ frequency. SANAE IV radar is technically and operationally similar to other 32 SuperDARN radars located at polar and mid latitudes (see Greenwald et al., 1995; Lester, 2013). The SuperDARN radars at different locations use uniform frequency (common mode) and other scanning parameters for half of the daily operational time (Greenwald et al., 1995; Hosokawa et al., 2005; Lester, 2013). For the remaining observational time, individual radar may be discretionary thus the operational parameters can be modified. In common mode (time) measurements which are used in this study, the SuperDARN radar beam is sequentially scanned from beam 0 to beam 15 across its 75 range gates with a step in azimuth variation of 3.33°, a scan repeat time of $\sim$ 2 minutes, a range resolution of 45 km, and a peak power of about 10 kW. The beams have maximum sensitivity at elevation angles of $\leq$ 35° to allow backscatter echo detection. The return echoes for each beam are integrated over 3 or 7 s. The field of view (FOV) of SANAE IV radar in geographic and geomagnetic coordinates is presented in Figure 1. The FOV shows that SuperDARN SANAE IV HF radar is located at the sub auroral location suitable for observations of HF backscatters within the Antarctic region. The backscatter delays at slant range gate 0 is set to 1200 μs inter–pulse period (length), which is equivalent to 180 km [i.e, within the MLT (Mesosphere and Lower–Thermosphere) region]. The subsequent pulse length is set to 300 μs, equivalent to a length of 45 km. We use measurements from the near range gates (0 to 1) which corresponds to 180–225 km. The oblique sounding technique of SuperDARN is such that it can detect coherent backscatters simultaneously within near range gates. These include field aligned irregularities in the ionospheric E region (sporadic E–region echoes), meteor trail, and PMSE. In order to isolate PMSE from other contaminating echoes, a systematic approach is needed. The sporadic E–region echoes are differentiated from the SuperDARN–PMSE by eliminating echoes with Doppler velocity and spectral width that are >50 m/s (see, Hosokawa et al., 2005) while the meteor echoes are removed by specifying a threshold of the backscatter power of greater than 6 dB. This is because the meteors are normally short–lived feature (<120 s scan time of SuperDARN radar) with a lower signal–to–noise ratio of the backscatter power (<6 dB), whereas PMSE generally exist longer than 20 minutes with higher (>6 dB backscatter power (Ogawa et al., 2004).

Figure 2 illustrates the typical example of the backscatter features (power, velocity and width) observed for 21 December and April 2005, for demonstrating the PMSE disturbances in the signal returns from radar. During the summer solstice (Figure 2 left) on 21 December 2005, backscatters return are seen to be higher in comparison to 21 April 2005 (see, Figure 2 right). According to the selection criteria mentioned above, we have analysed the diurnal and seasonal occurrence

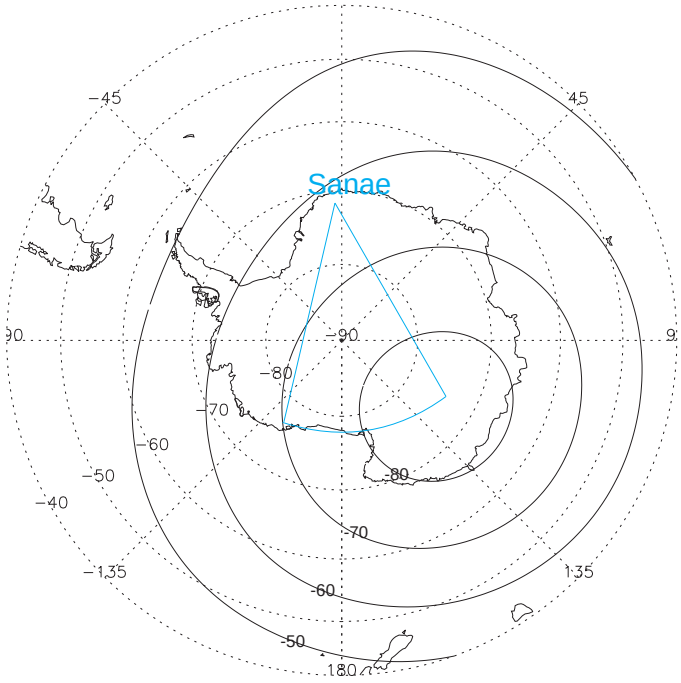

Figure 1: Map showing the SANAE radar field of view (blue line) projected on a geographic (dash lines) and geomagnetic (solid lines) coordinates.

characteristics of the SuperDARN–PMSE and concentrated on the SuperDARN–PMSE in relation to geomagnetic activity, cosmic noise absorption, mesopause temperature and mesospheric neutral winds. Note that in this study, winter season is referred to as April–September while summer refers to as October–March.

2.1.1. SUPERDARN neutral wind data

In addition to backscatters detection, SuperDARN observation of meteor trails in and below E–region (90–95 km) is associated with drift in neutral wind velocities which allows for studying the trends of meridional and zonal winds in relation to SuperDARN–PMSE season. A detailed description of neutral winds tracking using SuperDARN radar can be found elsewhere (Hussey et al., 2000; Chisham et al., 2007). Hussey et al. (2000), for example, found a good agreement between neutral wind measurements from SuperDARN radar and MF radar at an altitude of about 95 km. The advantage of MF radar observations of winds are its good altitude resolution. Note, that winds are altitude dependent and thus meteor radar observation of neutral winds may only be relative and not high accurately enough (Yukimatu and Tsutumi, 2002, 2003).

2.2. TIMED/SABER

The TIMED/SABER (Thermosphere Ionosphere Mesosphere Energetic and Dynamics / Sounding of the Atmosphere using Broadband Emission Radiometry) satellite was launched on 7 December 2001 into a 625 km circular orbit, with 74.1° inclination. The orbit period of TIMED/SABER is 102 minutes. SABER is measuring CO_2 15 μm limb emission which can be used to estimate

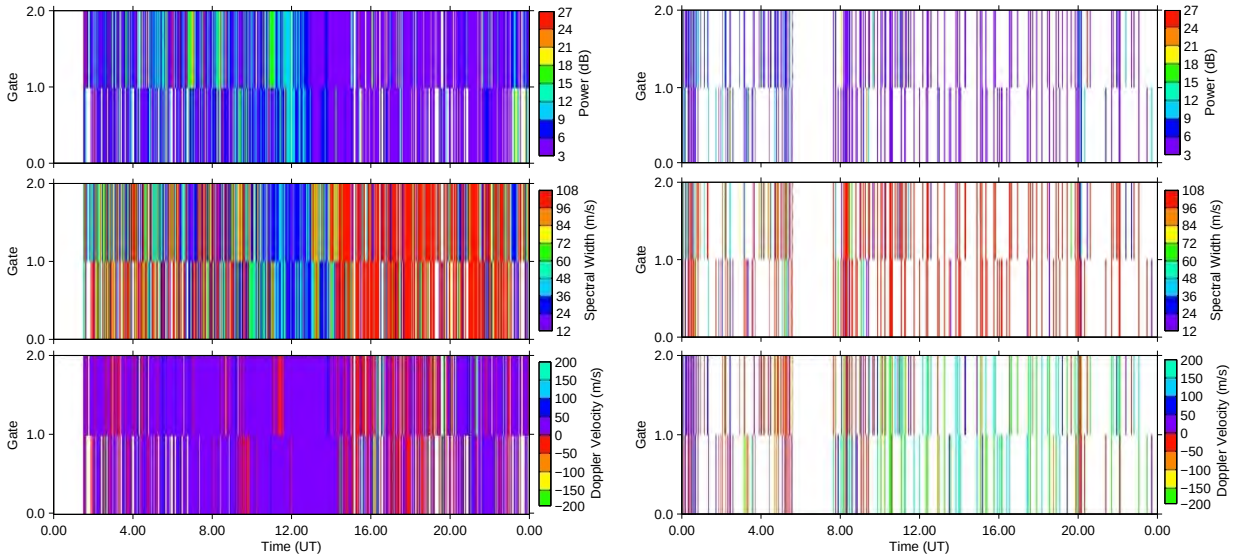

Figure 2: Range–time colormap of observed SuperDARN SANAE IV radar backscatter power, spectral width and Doppler velocity. The figure illustrates for beam 12 near range gates on 21 December 2005 (Left) and 21 April 2005 (Right).

the neutral temperatures up to approximately 130 km. In order to maintain a certain temperature in the instrument, SABER obtains profiles from 83°S to 52°N during its south–looking mode and of every 60 days the look direction switches to an analogous North–looking mode. Here, we have used the SABER temperature measurements during its south–looking mode. The data were then acquired in the vicinity of SANAE IV (i.e, 71 +/− 4° latitudes and 2 +/− 10° longitudes). We have used the temperature measurements for the year 2002/2003, 2003/2004, 2004/2005, 2005/2006 and year 2006/2007 summers.

3. Observations and analysis

3.1. Diurnal variation

Making use of SuperDARN data set covering about a decade, we examine both SuperDARN–PMSE conditions (Power, Spectral width and Doppler velocity) and occurrence rate. Figure 3 shows the local time (LT) variations of: (a) average power, (b) average Doppler velocity and (c) spectral width of backscatter echoes averaged over the near range gate and at the interval from 1 October to 31 March, for the different years. Since these aforementioned parameters are factors that might influence the form of the SuperDARN–PMSE, it will enable comparison with the long term SuperDARN–PMSE rate .

It is evident from the figure that the echo parameters have predominant diurnal variations. We observe peak average power on the local noon and lower on the night sides, as shown in Figure

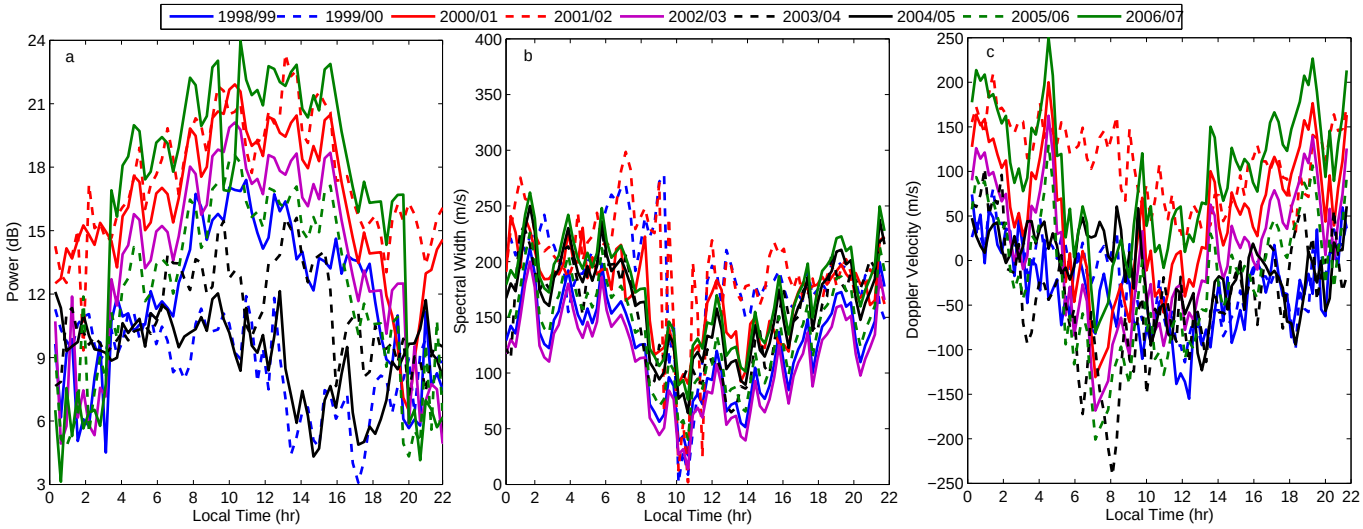

Figure 3: Diurnal variations of: a, average power; b, average spectral width; c, average Doppler velocity at slant range gate 0–1 from 1998 to 2007.

3 (a). The usually low average power observe for 1999/2000 and 2004/2005 summer might be, perhaps, due to data gap that exist during these periods. Generally, the average power for all years have similar behavior and exhibit a broad peak structure with the main peaks ($>$ 6 dB) around 11–14 LT and minima ($<$ 6 dB) around 20–22 LT. Between 10 LT and 13 LT, the average widths are 50–100 m/s and increase gradually with LT, peak around the midnights. The difference in spectral width variation for the different years is not obvious on both noon and night. In the early hours, we observe greater spectral widths for echoes, probably as a result of particle precipitation near the aurora oval region (Tsunoda, 1988). For Doppler velocity and spectral width (Figures 3 (b) and 3 (c)), the local noon variation is deeper than that of the night. The measured Doppler velocities indicate diurnal variations and are mainly negative on the local noon (around 13 LT) with a maximum of -250 m/s, and mainly positive at local midnight (around 22 LT) with a maximum of 250 m/s which indicates that the radar scatters are moving towards the radar. We found that there is no substantial difference in the diurnal variations of the Doppler velocity for all years; nonetheless, the values of the minima vary significantly between -250 m/s and 150 m/s and the maxima between -50 m/s and 150 m/s.

The SuperDARN–PMSE occurrence rate averaged over the interval from 1 October to 31 March from the SANAE IV HF radar is shown in Figure 4. The diurnal trends in the SuperDARN–PMSE occurrence rate show similar behaviour to those of radar backscatter parameters. The occurrence rates exhibit diurnal trends for all year and are characterised by maxima as seen almost at the same times as that of radar power and minima almost at the time of minimum

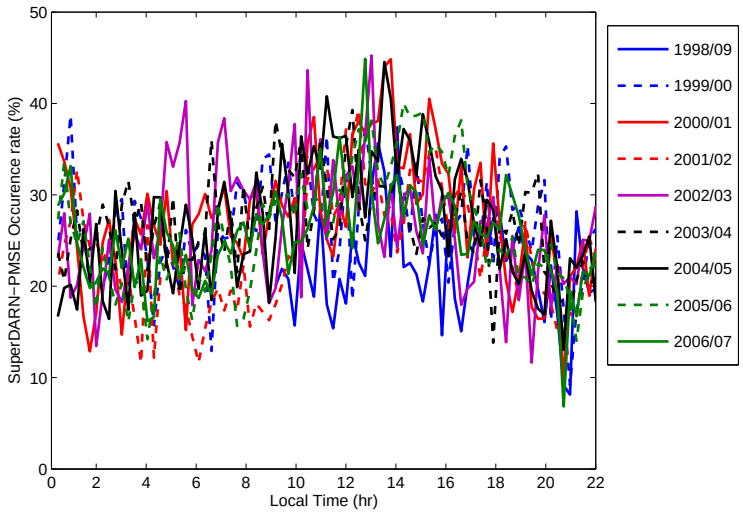

Figure 4: Averaged diurnal variations of SuperDARN–PMSE occurrence rate from the years 1998 to 2007.

spectral widths and Doppler velocities. Note that there are broader minima from 11 LT to 13 LT and minima between 20 LT to 22 LT. The shapes of diurnal variations are seen almost every year except 2002/2003 summer when occurrence rate peaks have about 3 h time lag. Assuming that SuperDARN–PMSE is a Poisson process, the hourly mean intervals from year to year rates should be described by an exponential distribution. Employing the maximum possible occurrence rate to evaluate the Cumulative Distribution Function (CDF), one finds that the probability of changes occurring by chance in the year to year SuperDARN–PMSE within an arbitrary 20 minute interval is P = 1.0–2.5 from year to year.

Similar diurnal pattern of PMSE variations was found by VHF radar observations (Hoffmann et al., 1999; Morris et al., 2005; Latteck et al., 2007; Nilsson et al., 2008). Hosokawa et al. (2005) observed similar diurnal results with Syowa and Iceland HF radar too. Also, a fitted diurnal model of PMSE variation by Klostermeyer (1999) show that, the contribution from solar ionisation and particle precipitation to diurnal variation of PMSE reflectivity is high. At high–latitudes, the ionisation of the MLT is mainly ascribable to the Lyman α radiation (Brekke, 1997) and precipitation of magnetospheric particles (for instance, De Abreu et al., 2010; Ogunjobi et al., 2014b,a). The α radiation can cause enhanced ionisation at the noon while the precipitation has a minimum at dawn (Codrescu et al., 1997). Thus a superposition of both ionisation sources might be a likely explanation for diurnal variations of SuperDARN–PMSE. One step way to ascertain this is by studying the geomagnetic activity dependence of SuperDARN–PMSE details of which is presented later (see Subsection 3.3). Nevertheless, there are some discrepancies in the temporal positions of maximum and minimum occurrences due to different conditions and

criteria such as power, width and velocity being employed for analysis in this study. Another plausible reasons for temporal discrepancies might be small from year to year changes in the shape of the diurnal variations.

Although, Liu et al. (2013) noted a semidiurnal variation of PMSE occurrence with Zhongshan HF radar. They observed primary maximum PMSE occurrence near 0 LT and a secondary maximum near 13 LT while a distinct minimum was near 19 LT. Balsley et al. (1983) and Morrison et al. (2007) had earlier reported that the occurrence of PMSE has a broad maximum at 1–2 h after the local noon and that of the secondary peak usually appears around the local midnight.

The major cause of diurnal and semidiurnal PMSE occurrence is not yet completely understood. Several factors can affect the PMSE intensity which includes electron density (Kirkwood, 1993), 3hr–shifted meridional winds (Hoffmann et al., 1999), temperature (Klostermeyer, 1999), planetary waves (Klekociuk et al., 2008) and energetic particle precipitation (Liu et al., 2013). Nonetheless, it is clear to note that these factors are complex and have different contributions.

3.2. Seasonal variation

The seasonal average of the echoes parameters from the near range gate can be compared with SuperDARN–PMSE rates. Therefore, we have combined the radar power, velocity and width measurements over the years 1998 to 2007 and grouped interms of months (from January to December). Figure 5 shows mean monthly variations of: (a) average power, (b) average Doppler velocity and (c) average spectral widths.

It is evident from the Figure 5 (a) that, the combined average power is higher during the Antarctic summer than in winter, which might probably be as a result of smaller population of backscatters owing to the solar radiation in summer. In Figure 5 (b), we observe the high level velocity during the winter (around late March) and gradual decrease towards the summer (late November). The echoes Spectral widths in the winter are larger than those in the summer as shown in Figure 5 (c).

Based on the seasonal average of the parameters, we examine the start and end periods of SuperDARN–PMSE peaks. The inter annual variations of the SuperDARN–PMSE occurrence rate observed by SANAE IV HF radar during Antarctic summers of the years from 1998 to 2007 are examined. To eliminate the influence of frequent data gap, the data (during common mode) are averaged with a running mean over 2 days.

It can be seen in Figure 6 that the highest peaks are shifted towards the summer solstice, suggesting that in the majority of cases, the SuperDARN–PMSE follows the initial conditions of Power, Doppler velocity and spectral width. The SuperDARN–PMSE suddenly peak in early December, maximise around December solstice, stay at the highest level of about 50 % to the early part of January and then decrease gradually to the end of February every year. Apparently, the increasing rates of SuperDARN–PMSE at higher power is attenuated towards the beginning of winter by larger spectral width. Through the observational periods, there is no significant changes in the trend of SuperDARN–PMSE occurrence rates.

These seasonal variations are in agreement with other PMSE observations from VHF radars Bremer et al. (for example, 2009) despite the difference in radar locations and experimental

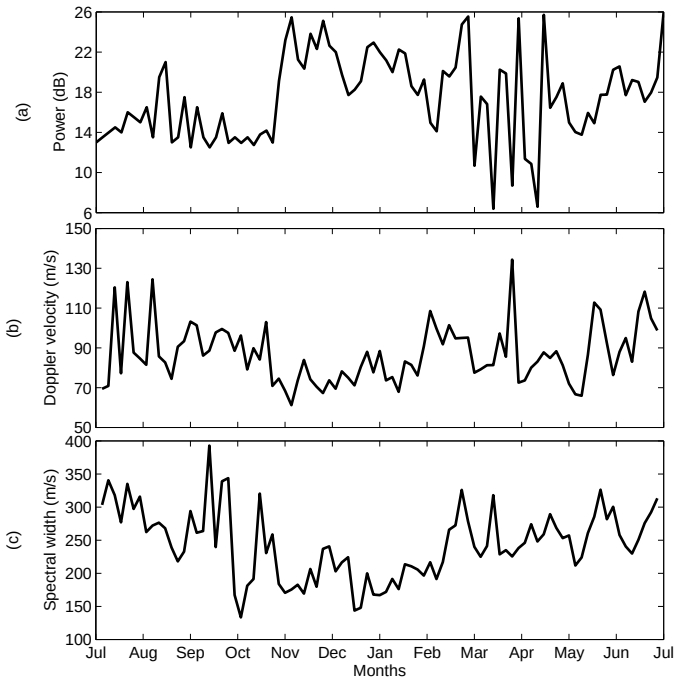

Figure 5: Combined Monthly variation of: a, average power; b, average spectral width; c, average Doppler velocity at slant range gate 0–1 from the years 1998 to 2007.

setup. These results also agree with previous short–term observations of PMSE with other radars despite the differences in location and time. Using SuperDARN HF radar, Hosokawa et al. (2005) found that the PMSE occurrence at Syowa (1999–2000 and 2000–2001) and Iceland (1999 and 2000) shows a sudden increase in the beginning of the summer, maximises days after the summer solstice, and a gradual decay to the end of January. Similarly, Liu et al. (2013) found an enhancement of PMSE intensity around the summer solstice using Zhongshan HF radar in Antarctica during 2010–2012. Note that, the determination of the range gate for potential PMSE depends partly on the radar location.

3.3. SuperDARN–PMSE occurrence in relation to geomagnetic activity

As noted above in Subsection 3.1, some radar observations have not only examined the geomagnetic activity dependence of backscatter echoes, but also the physics of the mechanisms involved. In order to examine a possible connection between SuperDARN–PMSE and geomagnetic activity, we present the combine diurnal and seasonal variations of SuperDARN–PMSE occurrence rate at different geomagnetic activity levels. The monthly average Kp index from the OMNI website (`http://omniweb.gsfc.nasa.gov`) illustrates the average level of geomagnetic activities from the years 1998 to 2007 as shown in Figure 7. On average, the level of Kp index varies for different years. For clarity, the Kp values are grouped into three thresholds; Kp = 0 (quite time), Kp = 1 (low activity), Kp = 2 (moderate activity) and Kp $\geq$ 3 (strong activity) during the period from 01 October to 31 March. Base on these thresholds, we combine the diurnal and seasonal SuperDARN–PMSE occurrence probability rate from 1998 to 2007 in 3°

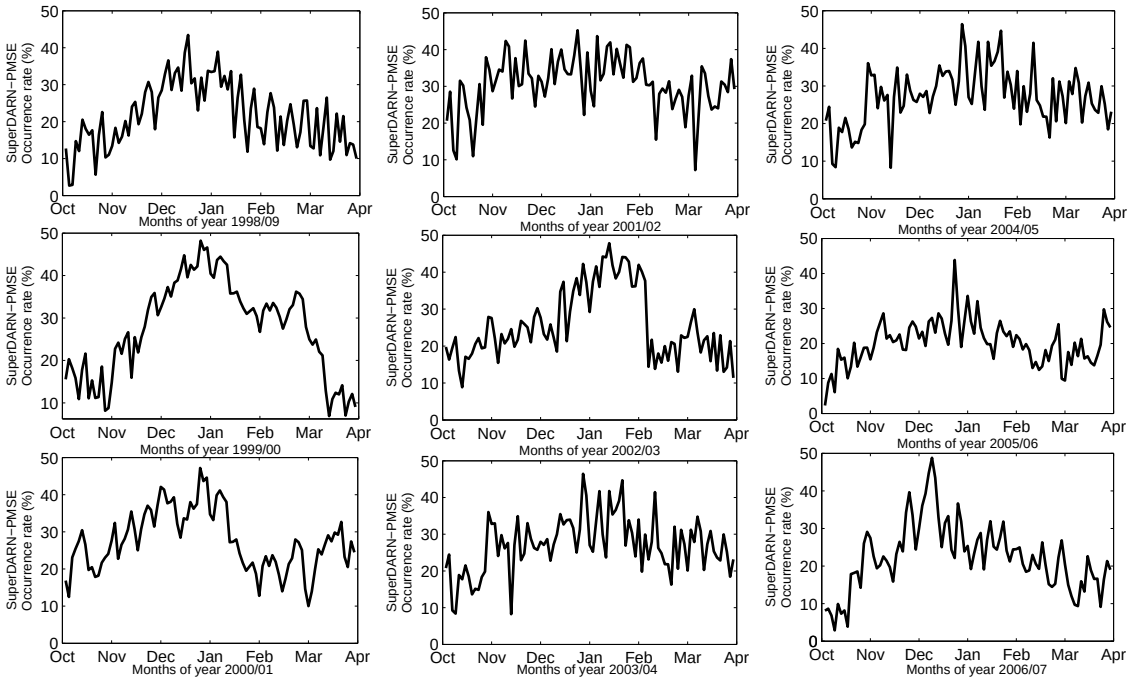

Figure 6: Inter annual variations of SuperDARN–PMSE occurrence rate from the years 1998 to 2007.. The data were averaged using a running mean over 2 days for time interval from 1 October till 31 March

resolution grid as shown in Figure 8.

In Figure 8 (a), when Kp = 0, the diurnal and seasonal SuperDARN–PMSE occurrence rate is shown. It is evident from the figure that, the peak occurrence is around 10–12 LT, minima is $\sim$ 21 LT. There is a high probability of the SuperDARN–PMSE occurrence during the summer months, with a value of $\sim$30%. At Kp$\leq$2 (Figures 8 (b) and (c)), the SuperDARN–PMSE occurrence probability rate rise to about 35%. We continue to observe enhancement in SuperDARN–PMSE occurrence probability rate at Kp$\geq$ 3 (Figure 8 (d)) with about 10% (i.e rise to over 45%) increase in comparison with quiet times interval.

The results support previous work by Ruohoniemi and Greenwald (1997) who have used the Goose Bay HF radar and showed that there is significant dependence of diurnal/seasonal echo occurrence on Kp index. Using the SuperDARN Syowa HF radar data, Hu et al. (2013) also examined the influence of geomagnetic activity on echo power, spectral width and Doppler velocity. They have suggested that the average spectral widths decrease while the echo power increase with an enhancement of geomagnetic activity. In this study, we found a significant correlation between the SuperDARN–PMSE occurrence probability rate and Kp index for the years 1998–2007 during the period from 1 October to 31 March; the highest rates are obtained during high geomagnetic activity and low during a quiet condition. This might, partly, be as a result of the polar hole near the aurora location of SANAE IV and/or due to strong activity associated with auroral substorms (Crowley et al., 1993).

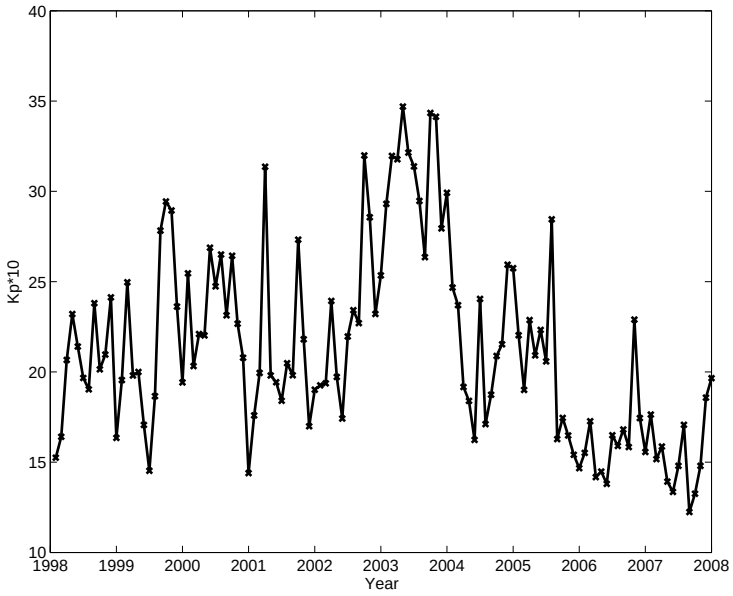

Figure 7: Monthly averaged Kp index in OMNI format from the years 1998 to 2007.

In order to understand the connection between ionisation and SuperDARN–PMSE occurrence rate, we have examined the SuperDARN–PMSE variations and cosmic noise absorption (not shown). We found no significant correlations between SuperDARN–PMSE occurrence rate and absorption. However, Morris et al. (2005) found a very weak correlation of PMSE observation from VHF radar and cosmic noise absorption. The anti correlation of SuperDARN–PMSE with absorption may be attributed to long HF radar wavelength in comparison to VHF radar wavelengths. Using HF radar, one is observing icy dust particle charging while electron diffusion is observed with VHF radar (Mahmoudian et al., 2011). Therefore, the VHF requires strong density gradient and by extension, high cosmic absorption. Intuitively, we expect high Kp index to cause robust cosmic noise absorption (Ogunjobi et al., 2014b); hence similar trend in the occurrence rate with Kp and absorption. Nonetheless, the inconsistency might be partly due to technical approach for obtaining Kp index, radar and riometer measurements. The Kp index, for example, is based on global geomagnetic field measurements and thus depends on the electron density above 100 km (Thomsen, 2004), while cosmic noise absorption is determined by height integrated electron density below 100 km (Clilverd et al., 2010).

3.4. Mesospheric temperature and winds in relation to SuperDARN–PMSE

Other factors might also induce significant influence on SuperDARN–PMSE occurrence probability rate if varies or remain steady over many years, for example, the neutral wind forcing. Since SANAE IV is at sub–auroral location, we may expect neutrals to dominate. The trend of neutrals (neutral winds and neutral temperature) in relation to SuperDARN–PMSE season might be significant. We investigate a possible connection between SuperDARN–PMSE peaks

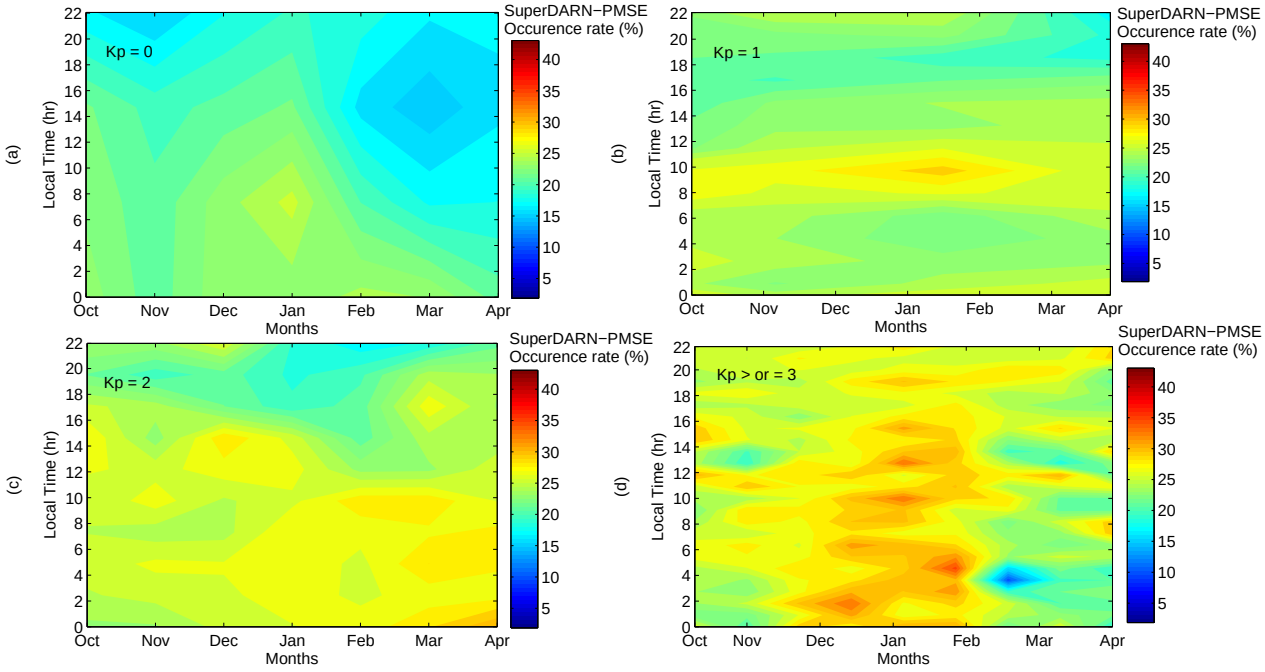

Figure 8: Diurnal and Seasonal contours for SuperDARN–PMSE at different geomagnetic activity levels: a, Kp = 0; b, Kp = 1; c, Kp = 2 and d, Kp $\geq$ 3 over observational periods.

and mesospheric temperature over SANAE IV. We present the average SABER vertical temperature during November, December, January and March of the possible years from 2002/2003, 2003/2004, 2004/2005, 2005/2006, 2006/2007 Antarctic summers in Figure 9. Note that SABER is mostly outside its south–looking mode in February months.

From the figures (Figures 9 a b, c ,d and e) it can be seen that, there is a lowering of mesopause temperature from December until January. These two months represent the relative period of maximum occurrence rate. In December and January, temperatures decrease to about 150 K while SuperDARN–PMSE rate also increases significantly to about 50% except for the year 2003/2004.

Conversely, we observe decrease in mesopause temperature in the months of November and March in comparison with SuperDARN–PMSE seasonal distribution in Figure 6, the mesopause temperature during November and March is generally seen to be $>$ 180 K tied to lower ($\sim$10%) superDARN–PMSE occurrence rate. Perhaps the temperatures in the austral mesosphere are closer to radiative equilibrium. This can only be true if the topography in the troposphere plays an important role (via gravity wave generation) in the mesospheric dynamics since there is less orographic terrain in Antarctic (Lübken et al., 2004). Unfortunately, temperature measurements is not available in our region of interest during February when the SuperDARN–PMSE rate gradually decreases. Nevertheless, temperature profiles during March illustrate what should be anticipated as it gets higher than the summer solstice. Analysis of mesospheric neutral wind flow may, perhaps, provide a reasonable light on this aspect.

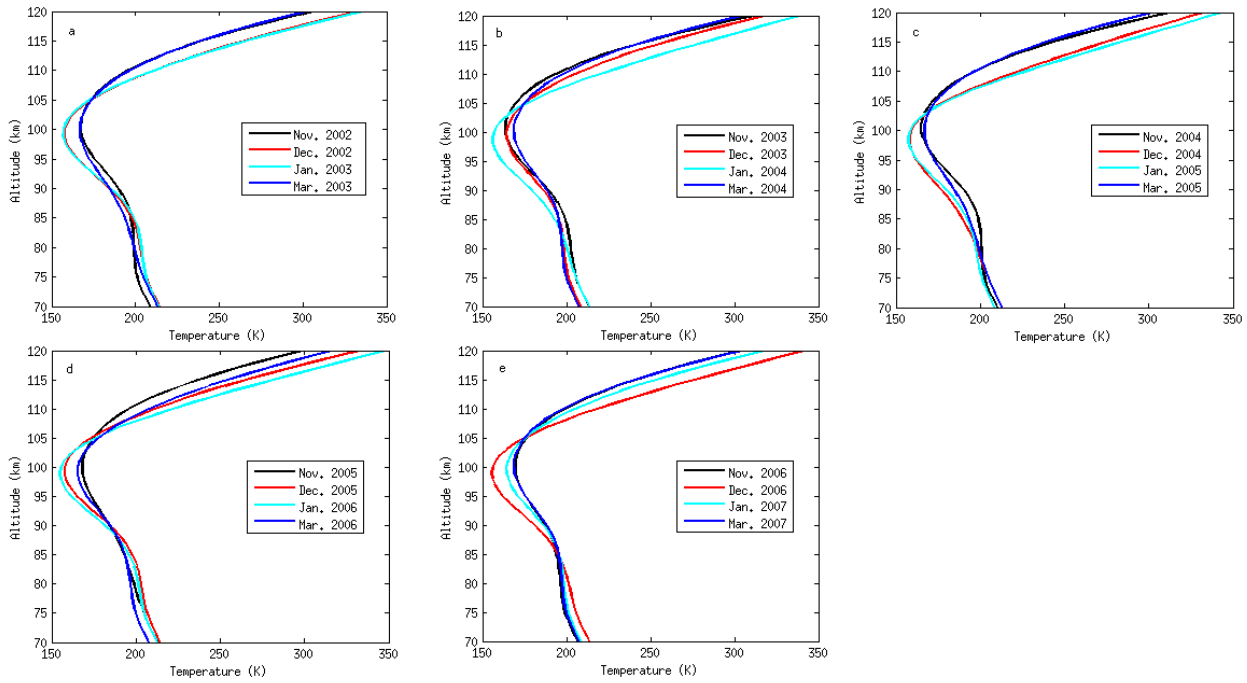

Figure 9: From a–d: SABER mean temperature profiles from 2002/2003 to 2006/2007 Antarctic summers. The black, red, light green and blue line represents November, December, January and March respectively. The measurements are obtained from SABER in the vicinity of SANAE IV Radar site location.

Although fewer attempts to obtain convincing correlations between PMSE and temperature can be found in literature. The first direct simultaneous observations of temperature and of PMSE was demonstrated by Kirkwood et al. (2002) with SkiYMET and ESRAD radar. The authors examined the response of PMSE to temperature fluctuations associated with 5–day planetary waves and found that the temperature was the most significant parameter affecting PMSE occurrence. Some previous work (e.g, Morris et al., 2009) observed minor linkage between PMSE and temperatures with satellite observation. Smirnova et al. (2010) also suggested that pole to pole circulation would result in extremely low temperature around summer solstice to have charged ice particle formation, hence high PMSE production in summer.

In order to test if SuperDARN–PMSE observation corroborate these suggestions, we examine the direction of meridional and zonal wind over SANAE IV in relation to mesospheric temperature variations. This might indirectly help to confirm if SuperDARN–PMSE peaks are indeed steady over the long term. Here we obtained radar measurements of mesospheric winds (meridional and zonal winds) from the years 1998–2007. Note that this is meteor radar wind observation hence the caveat in Sub-subsection 2.1.1 applies. Figure 10 (top panel and bottom) presents contours of all the available monthly–mean winds. There is a data gap in early parts of 1998 and 2007 from SANAE IV superDARN radar. This Figure shows a clear indication of how the monthly–mean winds vary from year to year. Since the data analysis is based on monthly averages, we might ignore the short periodic waves.

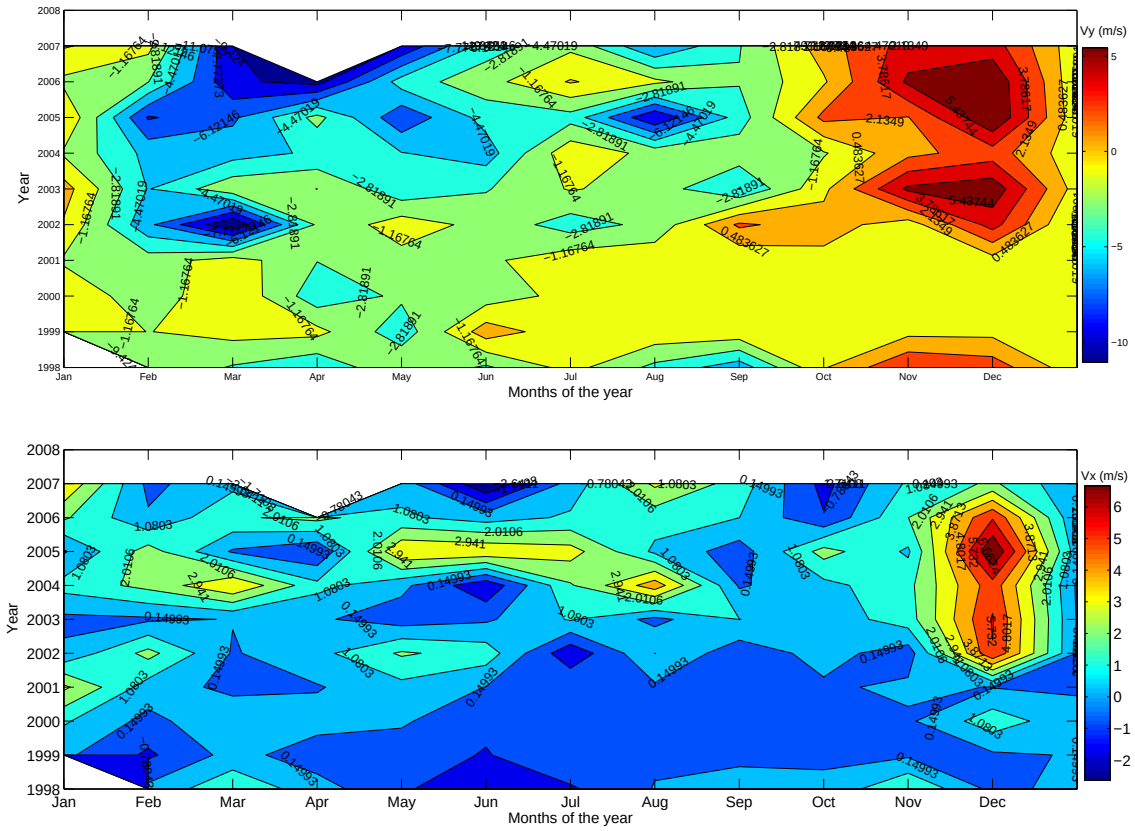

Figure 10: Seasonal and year–to–year variations of meridional (top) and zonal (bottom) mean winds from the years 1998 to 2007.

In both meridional (Figure 10 top) and zonal wind (Figure 10 bottom) we observe a seasonal pattern that repeats from year–to–year, at least in summer. It can be seen that prior to the start of the SuperDARN–PMSE peaks (November), the mean meridional winds become more positive and the zonal winds also grow significantly. Conversely, we observe a period of equatorward (negative) zonal winds starting from middle of December to early January months while the poleward meridional winds are decreasing. This period (mid December to early January) represents the time of high peaks in seasonal SuperDARN–PMSE (Figures 6). According to Andrews et al. (1987), mesospheric transport circulation is pole to pole; there is rising motion in the summer hemisphere, cross equatorial drift, and sinking in the winter hemisphere. Such that the equatorward circulation will induce the cold air (Morrison et al., 2007) for the benefit of superDARN–PMSE occurrence rates (e.g, Lübken et al., 2004; Morris et al., 2009). This sinking situation in winter is more obvious around March.

4. Summary and conclusion

We have observed strong backscatter echoes at near ranges by SuperDARN SANAE IV HF radar that cannot be explained by sporadic E–region or meteor echoes. We have proposed SuperDARN–PMSE as the most possible origin of these echoes. Furthermore, we presented several characteristics of SuperDARN–PMSE based on the nine summer (1998/1999–2006/2007) observation using SANAE IV HF radar. These include diurnal variation, seasonal variation and its dependence on geomagnetic activity, cosmic noise absorption, mesospheric temperature and winds. Based on the obtained results, following are salient features noted:

- Similar to previous observations, SuperDARN–PMSE seasonal rate is enhanced at the beginning of December summer, remains at the highest level until several days after the summer solstice and then gradually decreases towards the end of February every year. The SuperDARN–PMSE occurrence rate show diurnal variations with broader minima from 11 LT to 13 LT and minima between 20 LT to 22 LT. No significant year–to–year variation is found in the diurnal SuperDARN–PMSE occurrence rate.

- The difference of SuperDARN–PMSE occurrence rate is significant for different geomagnetic activity, Kp, levels. We observed higher occurrence rates during enhanced magnetospheric convection. When Kp = 0, we obtained ∼30% of SuperDARN–PMSE occurrence rate. At Kp $\leq$ 2 SuperDARN–PMSE occurrence probability rate increases to about 35%. We continue to observe increase of SuperDARN–PMSE at Kp$\geq$3 with over 45% increase occurrence probability rate. Since at high–latitudes the ionisation of the MLT is mainly ascribable to the Lyman α radiation and precipitation of magnetospheric particles, we suggest that a superposition of both ionisation sources might be a likely explanation for diurnal variations of SuperDARN–PMSE.

- The SuperDARN–PMSE peaks are found to correlate with the decrease of mesospheric temperature. At the same time, the decrease in temperature coincides with the equatorward zonal wind and decelerating poleward meridional winds. After comparing the relative trend of both meridional and zonal winds is from year–to–year, we can conclude that the pole to pole mesospheric transport circulations might play an important role in SuperDARN–PMSE occurrence probability rate.

Acknowledgements. The authors express thanks for the support of South Africa National Antarctic Program (SANAP) and logistics of South Africa National Space Agency (SANSA) in providing SANAEIV riometer data. SANAP, SANSA and HF radar group, University of KwaZulu–Natal, SA support the SANAE IV HF radar. The SuperDARN radar wind data is provided by British Antarctic Survey, UK, at http://psddb.nerc–bas.ac.uk. Research is supported by SANSA.

References

Andrews, D., Holton, J., Leovy, C., 1987. Middle Atmospheric Dynamics. Academic Press, New York and London.

Balsley, B., Ecklund, W., Fritts, D., 1983. Mesospheric radar echoes at Poker Flat, Alaska: evidence for seasonally dependent generation mechanisms. Radio Science 18, 1053–1058.

Brekke, A., 1997. Physics of the Upper Polar Atmosphere. Wiley-Praxis Series in At- mospheric Physics, John Wiley and Sons, New York.

Bremer, J., Hoffmann, P., Latteck, R., Singer, W., Zecha, M., 2009. Long-term changes of (polar) mesosphere summer echoes . Journal of Atmospheric and Solar-Terrestrial Physics 71, 1571–1576.

Chisham, G., Lester, M., Milan, S.E., Freeman, M.P., et al., 2007. A decade of the super dual auroral radar network (superdarn): scientific achievements, new techniques and future directions. Survey in Geophysics 28, 33–109.

Cho, J.Y.N., 1997. An updated review of polar mesosphere summer echoes' observation, theory, and their relationship. Journal of Geophysical Research 102 (D2), 2001–2020.

Clilverd, M.A., Rodger, C.J., Gamble, R.J., Ulich, T., Raita, A., Seppälä, A., Green, J.C., Thomson, N.R., Sauvaud, J.A., Parrot, M., 2010. Ground-based estimates of outer radiation belt energetic electron precipitation fluxes into the atmosphere. Journal of Geophysical Research 115, A12304.

Codrescu, M., Evans, D., Fuller-Rowell, T.J., Roble, R., 1997. Medium energy particle precipitation influences on the mesosphere and lower thermosphere . Journal of Geophysical Research 102 (A9), 19977–19987.

Crowley, G., Carlson, H.C., Basu, S., et al., 1993. The dynamic ionospheric polar hole. Radio Science 28, 401–413.

De Abreu, A.J., et al., 2010. Hemispheric asymmetries in the ionospheric response observed in the American sector during an intense geomagnetic storm. Journal of Geophysical Research 115, A12312.

Ecklund, W., Balsley, B., 1981. Long–term observations of the Arctic mesosphere with the MST radar at Poker Flat, Alaska. Journal of Geophysical Research 86, 7777–7780.

Greenwald, R.A., Baker, K.B., Dudeney, J.R., Pinnock, M., Jones, T.B., Thomas, E.C., Villain, J.P., Cerister, J., Senior, C., Hanuise, C., et al., 1995. DARN/SuperDARN. Space Science Review 71, 761–796.

Hervig, M.E., Gordley, L.L., Russell III, J.M., Bailey, S.M., 2009. SOFIE PMC observations during the northern summer of 2007. Journal of Solar–Terestrial Physics 71, 331–339.

Hoffmann, P., Singer, W., Bremer, J., 1999. Mean seasonal and diurnal variations of PMSE and winds from 4 years of radar observations at ALOMAR. Geophysical Research Letters 26, 1525–1528.

Hosokawa, K.T., Ogawa, N.F., Arnold, M., Lester, N.S., and, A.S.Y., 2005. Extraction of polar mesosphere summer echoes from SuperDARN data. Geophysical Research Letters 32, L12801.

Hu, H.Q., Liu, E.X., Liu, R.Y., 2013. Statistical characteristics of ionospheric backscatter observed by SuperDARN Zhongshan radar in Antarctica . Advances in polar science 24, 19–31.

Huaman, M.M., Balsley, B., 1999. Differences in near–mesopause summer winds, temperatures, and water vapour at northern and southern latitudes as possible causal factors for inter–hemispheric PMSE differences. Geophysical Research Letters 26, 1529–1532.

Hussey, G.C., Meek, C.E., André, D., Manson, A.H., Sofko, G.J., 2000. A comparison of Northern Hemisphere winds using SuperDARN meteor trail and MF radar wind measurement . Journal of Geophysical Research 105, 18053–18066.

Kirkwood, S., 1993. Modeling the undisturbed high-latitude E region. Advances in Space Research 13, 3101–3104.

Kirkwood, S., Barabash, V., Brandstrom, B., Hocking, W., Mostrom, A., Mitchell, N., Stebel, K., 2002. Noctilucent clouds, PMSE and 5-day planetary waves: a case study. Geophysical Research Letters 29, 50.1–50.4.

Klekociuk, A., Morris, R., Innis, J., 2008. First Southern Hemisphere common volume measurements of PMC and PMSE. Geophysical Research Letters 35, L24804.

Klostermeyer, J., 1999. On the diurnal variation of polar mesosphere summer echoes. Geophysical Research Letters 26, 3301–3304.

Latteck, R., Holdsworth, D.A., Morris, R.J., Murphy, D.J., Singer, W., 2007. Observation of polar mesosphere summer echoes with calibrated VHF radars at 69° in the northern and southern hemispheres. Geophysical Research Letters 34, L14805.

Lester, M., 2013. The Super Dual Auroral Radar Network (SuperDARN): An overview of its development and science. Advances in polar science 24, 1–11.

Liu, E.X., Hu, H.Q., Hosokawa, K., Liu, R.Y., Wu, Z.S., Xing, Z.Y., 2013. First observations of polar mesosphere summer echoes by SuperDARN Zhongshan radar. Journal of Atmospheric and Solar–Terrestrial Physics 104, 39–44.

Lübken, F.J., Mullemann, A., Jarvis, M.J., 2004. Temperatures and horizontal winds in the Antarctic summer mesosphere. Journal of Geophysical Research 109, D24112.

Mahmoudian, A., Scales, W.A., Kosch, M.J., Senior, A., Rietveld, M., 2011. Dusty space plasma diagnosis using temporal behavior of polar mesospheric summer echoes during active modification. Annales Geophysicae 29, 2169–2179.

Morris, R., Holdsworth, D., Klekociuk, A., Latteck, R., Murphy, D., Singer, W., 2009. Inner-hemispheric asymmetry in polar mesosphere summer echoes and temperature 69 latitude. Journal of Atmospheric and Solar-Terrestrial Physics 71, 464–469.

Morris, R., Terkildsen, M., Holdsworth, D., Hyde, M., 2005. Is there a causal relationship between cosmic noise absorption and PMSE? . Geophysical Research Letters 32, L24809.

Morrison, R.J., Murphy, D., Klekociuk, A., Holdsworth, D.A., 2007. First complete season of PMSE observations above Davis, Antarctica, and their relation to winds and temperatures . Geophysical Research Letters 34, L05805.1–L05805.5.

Nilsson, H., Belova, E., Kirkwood, S., Klekociuk, A., Latteck, R., Morris, R.J., Murphy, D.J., Zecha, M., 2008. Simultaneous observations of polar mesosphere summer echoes at two different latitudes in Antarctica. Annales Geophysicae 26, 3783–3792.

Ogawa, T., Nozawa, S., Tsutumi, M., Arnold, N.F., Nishitani, N., Sato, N., Yukimatu, A.S., 2004. Arctic and Antarctic polar mesosphere summer echoes observed with oblique incidence HF radars: analysis using simultaneous MF and VHF radar data. Annales Geophysicae 22, 4049–4059.

Ogunjobi, O., Sivakumar, V., Mbatha, N., 2014a. A case study of energy deposition and absorption by magnetic cloud electrons and protons over the high latitude stations: effects on the mesosphere and lower thermosphere. Terrestrial, Atmospheric and Oceanic Sciences 25, 219–232.

Ogunjobi, O., Sivakumar, V., Sivla, W.T., 2014b. A superposed epoch study of the effects of solar wind stream interface events on the upper mesospheric and lower thermospheric temperature. Advances in Space Research , In press.

Palmer, J.R., Rishbeth, H., Jones, G.O.L., S., W.P.J., 1996. A statistical study of polar mesosphere summer echoes observed by EISCAT. Journal of Atmospheric and Solar–Terrestrial Physics 58, 307–315.

Rapp, M., Lübken, F.J., 2004. Polar mesosphere summer echoes (PMSE): review of observations and current understanding. Atmospheric Chemistry and Physics Discussions 4, 4777–4876.

Richardson, I.G., Cliver, E.W., Cane, H.V., 2001. Sources of geomagnetic storms for solar minimum and maximum conditions during 1972-2000. Geophysical Research Letters 28, 2569–2572.

Röttger, J., 1994. Polar mesosphere summer echoes: Dynamics and aeronomy of the mesosphere. Advances in Space Research 14, (9)123–(9)137.

Ruohoniemi, J.M., Greenwald, R.A., 1997. Rates of scattering occurrence in routine HF radar observations during solar cycle maximum. Radio Science 32, 1051–1070.

Smirnova, M., Belova, E., Kirkwood, S., Mitchell, N., 2010. Polar mesosphere summer echoes with ESRAD, Kiruna, Sweden: Variations and trends over 1997–2008. Journal of Atmospheric and Solar-Terrestrial Physics 72, 435–447.

Thomas, G.E., Olivero, J., 2001. Noctilucent clouds as possible indicators of global change in the mesosphere. Advances in Space Research 28, 937–946.

Thomsen, M.F., 2004. Why Kp is such a good measure of magnetospheric convection. Space Weather 2, S11004.

Tsunoda, R.T., 1988. High-Latitude F-Region Irregularities: A Review and Synthesis. Technical Report.

Yukimatu, A.S., Tsutumi, M., 2002. A superDARN meteor wind measurement: Raw time series analysis method and its application to mesopause region dynamics. Geophysical Research Letters 29, 1981.

Yukimatu, A.S., Tsutumi, M., 2003. Correction to "A new SuperDARN meteor wind measurement: Raw time series analysis method and its application to mesopause region dynamics" by Akira Sessai Yukimatu and Masaki Tsutsumi. Geophysical Research Letters 30, 1026.

Chapter 6

The mid–latitude upper thermospheric zonal winds variation during the recent solar minimum*

* This chapter needs to be cited as:

Ogunjobi, O., Sivla, W. T., Sivakumar, V., 2014d. The mid–latitude upper thermospheric zonal winds variation during the recent solar minimum. *To be submitted for publication.*

The mid–latitude upper thermospheic zonal winds variation during the recent solar minimum

O. Ogunjobi[a,*], W. T. Sivla[b], V. Sivakumar[a]

[a]*School of Chemistry and Physics, University of KwaZulu–Natal, Durban, South Africa*
[b]*Department of Physics, Kogi State University, Anyigba, Nigeria*

Abstract

Using zonal wind data from the accelerometer on board the CHAMP satellite, we examined the variations of mid–latitude upper thermospheric zonal winds during low solar activity period of year from 2005 to 2008. This period is characterised by low magnetic activity and extreme low solar flux levels. Asymmetry in diurnal wind variations is observed during the March and September equinox periods in both Northern (40°N to 50°N) and Southern (40°S to 50°S) mid–latitudes. No significant difference is observed between Northern and Southern mid–latitude wind variations during the equinox seasons. The switch from westward to eastward direction is observed at about 1400 LT, while the westward transition occurs from about mid-night to 0400 LT for all the seasons. Large zonal wind speeds are observed at and after dawn in both hemispheres. The significant differences observed in the morning winds at the two mid–latitude bands during the solstices may be ascribed to the differences in the solar irradiation. The zonal winds in this study are longitudinally averaged and results may thus differ from single station measurements.

Keywords: Zonal wind, Mid–latitudes, CHAMP satellite, iterative algorithm, solar irradiation

1. Introduction

The neutral winds are an important driver or a critical parameter in nearly all electrodynamics and plasma physics processes in the mid–latitude ionosphere–thermosphere (Larsen and Fesen, 2009). The thermosphere is often considered as a linear dissipative oscillatory system, which suppresses the small–scale and short–term structures more effectively (Kazimirovsky et al., 2006). Thermospheric variability can be externally or internally generated. External sources arise from geomagnetic activity, solar extreme ultraviolet (EUV), tides and wave disturbances from the lower layers of the atmosphere while the internal variabilities arise from the coupling between ionised species and the neutral gas. Under very quiet geomagnetic conditions, a clear thermospheric and ionospheric response to magnetospheric processes can be observed at high geomagnetic latitudes (Rees, 1995). It has been suggested, however, that the electrodynamics of the mid–latitude ther-

*Corresponding author. Tel.: +27 84 824 2132.
Email addresses: olakunle.ukzn@gmail.com (O. Ogunjobi), sivla_w@yahoo.com (W. T. Sivla), venkataramans@ukzn.ac.za (V. Sivakumar)

mosphere can also be influenced by magnetospheric processes (Walker, 1988).

High latitude forcing contributes to the energy and momentum of the Earth's thermosphere. According to Aruliah et al. (2004), the ionospheric ion velocity and thermospheric neutral wind are related to the effective ionospheric electric field and Earth's magnetic field as follows:

$$E_{eff} = (\vec{v} - \vec{B}) + (\vec{u} - \vec{B}) \tag{1}$$

where E_{eff} is the ionospheric electric field, v is the ionospheric ion velocity, u is the neutral wind and B the Earth's magnetic field. Zonal wind flow in the upper thermosphere is regulated by ion drag. The pressure gradient force balances ion drag in the mid–latitudes upper thermosphere. Ion drag results from collision or interactions of the neutral gas with the plasma. Ignoring all the forces that contribute in driving thermospheric circulation, the change in wind velocity according to Nozawa and Brekke (1995) is given by:

$$\frac{\vec{u}}{dt} = -v_{in}(\vec{u} - \vec{v}) \tag{2}$$

where v_{in} is the ion–neutral collision frequency. Thermospheric winds blow in great circular paths along the pressure gradient from the high pressure on the day side to the low pressure on the night side. At mid–latitudes the pressure variation in the thermosphere is dominated by in–situ solar heating, giving rise to a diurnal circulation pattern (Emery, 1977) and irregular behavior on a time scale of hours (Walker, 1988). The thermosphere is stably stratified, so the factors that give rise to the irregular behavior are, likely, different from those in the mid–latitude troposphere.

Today thermospheric winds are observed using three main techniques namely; the Incoherent Scatter Radar technique, the optical technique and the satellite drag technique. Although a number of important features have been derived from datasets obtained from Fabry–Perot interferometer wind observations. The interferometer technique has its limitations (e.g. uncertainty in emission height, restriction to dark hours, clear sky and reduced moon phases Lühr et al., 2007). Also, the physical assumptions used by the radar technique break down under disturbed conditions (Liu et al., 2006). Nevertheless, the satellite technique provides wind measurements globally and can be used for wind measurements at all altitudes. Although mid–latitude thermospheric wind studies have been carried out in the last two decades using Fabry–Perot interferometers, incoherent scatter radar, ground–based ionosonde, satellite data and general circulation models (Bounsanto, 1991; Hedin et al., 1991; Duboin and Lafeuille, 1992; Fuller-Rowell et al., 1994, 1996; Burns et al., 1995; Fesen et al., 1995; Emery et al., 1999; Kawamura et al., 2000; Fejer et al., 2002; Balan et al., 2004).

In this study, we have used zonal wind data from the CHAMP (Challenging Mini–Satellite Payload) accelerometer readings to study diurnal wind variation in the mid–latitudes during quiet times of the recent solar minimum phase. The prolonged minimum in solar activity between solar cycles 23 and 24 was unique during the Space Age, and the resulting state of the thermosphere has never been fully observed (Bruinsma and Forbes, 2010).

Long term periods of high solar activity or low solar activity are of great importance in the energy balance of our planet (Moussas et al., 2005). As neutral densities are drastically reduced,

during this extremely low solar activity period, it may also induce changes in seasonal variations, atmospheric compositions, neutral winds and ionospheric density. In response to corresponding prolonged low levels of solar EUV irradiance, during the minimum cycle 23/24, the thermosphere was expected to have been unusually cool and contracted. This study will augment the previous ground–based observations of wind behavior and improve our understanding of wind climatology in the mid–latitudes.

2. Data source and selection

The satellite CHAMP, an acronym for challenging minisatellite payload (Reigber et al., 1996), was launched in July 2000. As CHAMP is in a near–circular, polar orbit (87.30° inclinations) with a precession rate of about 1.5° per day, it provides coverage of all local times and latitudes every 130 days (Liu et al., 2006). From its initial altitude at 456 km CHAMP orbit decayed to about 350 km during the first five years (Ritter et al., 2010). With 15 orbits per day, the CHAMP satellite crosses any mid–latitude band 15 times during its ascending motion and 15 times during its descending motion. CHAMP provides pole–to–pole latitudinal coverage. This takes place at different longitudes due to the rotation of the Earth. For a single day, the relative position of the sun and the satellite changes very little. Therefore, satellite measurements at the same geomagnetic latitude, although at different longitudes, are within a small range of Local Solar Time (LST). Although, the data for a single day at given geographic latitude are within a short range of LST, the corresponding geomagnetic latitudes and universal times of these data are different at different longitudes.

The zonal wind measurements used in this study are from the data derived by Doornbos et al. (2010), using an iterative algorithm. In this procedure, the modelled aerodynamic force is varied until it coincides with the observed acceleration (Ritter et al., 2010). The data in this study cover the period from 1st January 2005 to 31st December 2008. Zonal wind speeds are considered in the geomagnetic mid–latitudes, 40°N to 50°N and 40°S to 50°S. Wind speeds are then sorted for geomagnetic activity index, Ap<8. Figure 1 shows the variation of the geomagnetic activity index, Kp index, sunspot number, Ap index and the solar proxy (F10.7), from 1st January 2005 to 31st December 2008. Our period of study falls under the solar minimum of the recent solar cycle and the solar flux values can be seen to vary between 102 s.f.u and 65 s.f.u. During periods of high solar activity, peak values of the solar flux proxy can go above 250 s.f.u. The data are grouped into seasons, the June solstice (May, June, July), December solstice (November, December, January) and March equinox (February, March, April) and September equinox (August, September, October). The data in each of the seasons are binned and averaged over magnetic Local Time (LT) and geomagnetic latitudes. Figure 2 shows the number of measurements in each magnetic local time bin for each of the seasons.

3. Results

3.1. Diurnal variation: conjugate comparison

Figure 3 shows the zonal wind averaged over all seasons for the Northern and Southern hemisphere mid–latitude bands. The averaged winds blow westward at 0300 LT. The switch of

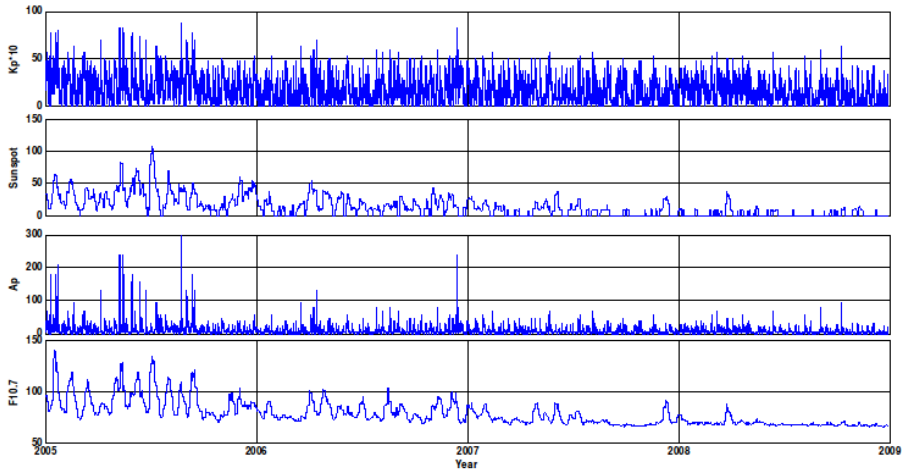

Figure 1: From top to bottom: Kp index, sunspot number, Ap index and the solar flux proxy (F10.7) from 2005 to 2008.

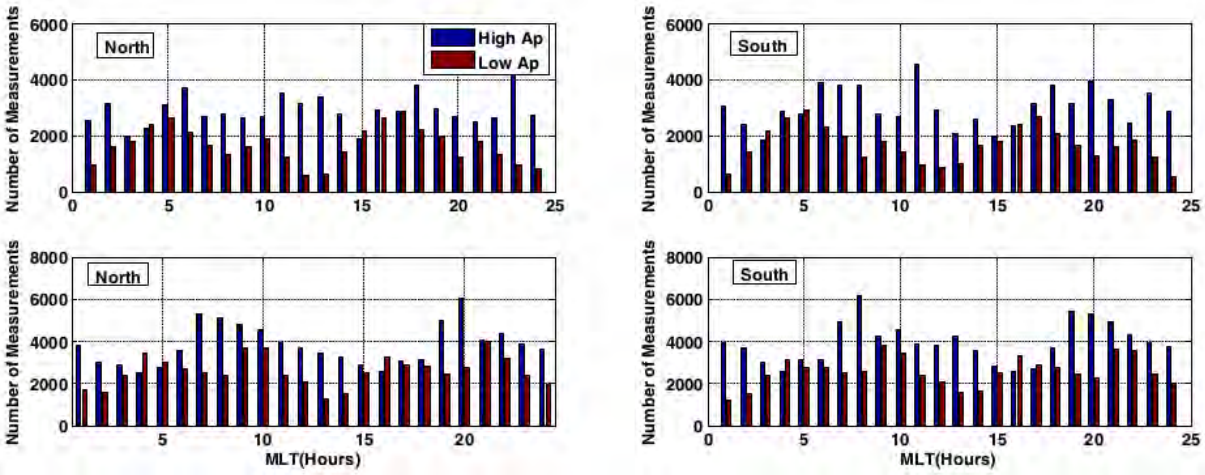

Figure 2: Number of measurements in each local time bins under various solar flux and geomagnetic conditions in the Northern and Southern hemisphere mid–latitudes. Upper panels are for high solar flux level while the lower panels are for low solar flux level in both Northern and Southern hemispheres.

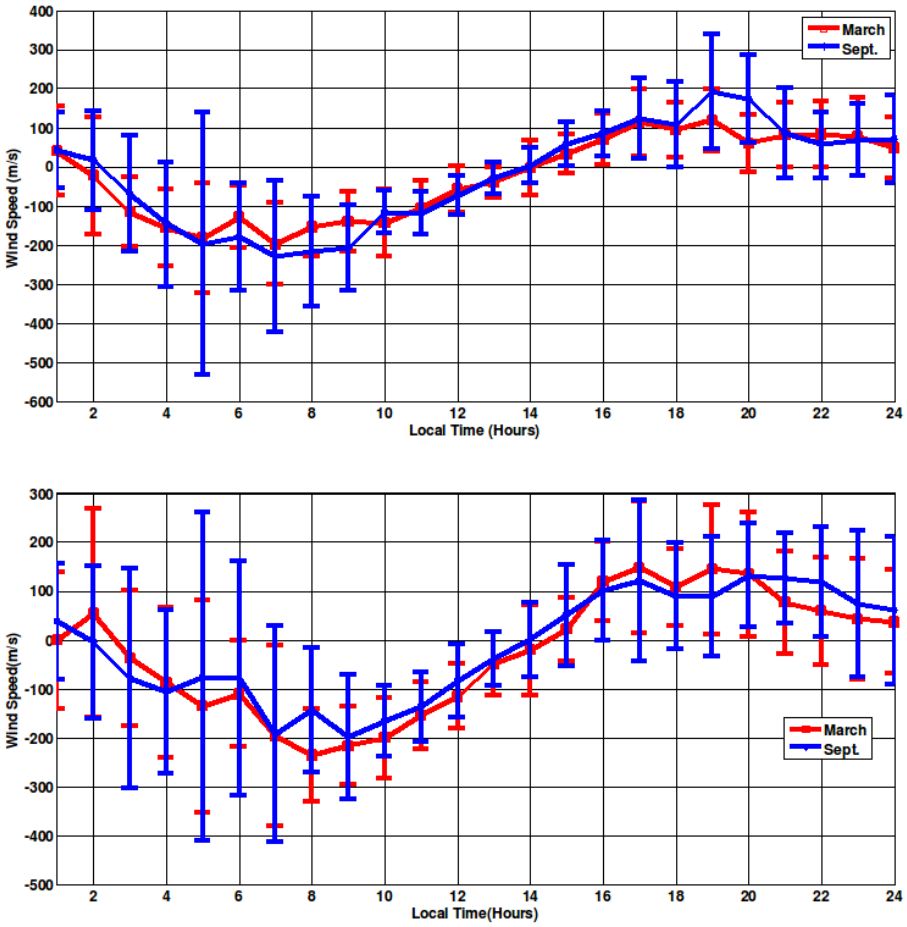

Figure 3: Average March and September winds in Northern hemisphere (upper panel) and Southern hemisphere (lower panel) during year 2005–2008.

direction from westward to eastward occurred at about 1500 LT in both hemispheres. A larger eastward wind is observed in the Southern hemisphere mid–latitude band from around 1700–2300 LT. The Southern hemisphere wind is more westward during the day from about 0400–0700 LT. Peak westward and eastward winds were observed in the Southern hemisphere mid–latitude zonal winds at 0800 and 2000 LT respectively.

3.2. Equinox seasons

Figures 4 shows the diurnal mean variation of the zonal wind speeds observed during the equinoxes. During the March and September equinoxes, the eastward transition is observed at about at about 1400 LT. The March equinox eastward to westward switch is observed at about 0100 LT for the Northern hemisphere winds while the Southern hemisphere wind switches to same in 2 hr later. The westward switch in direction is observed at 0200 LT for both hemispheres during the September equinoxes. A peak westward wind speed going above 200 m/s is observed in the Southern hemisphere during the March equinox from about 0700–1000 LT. After the eastward

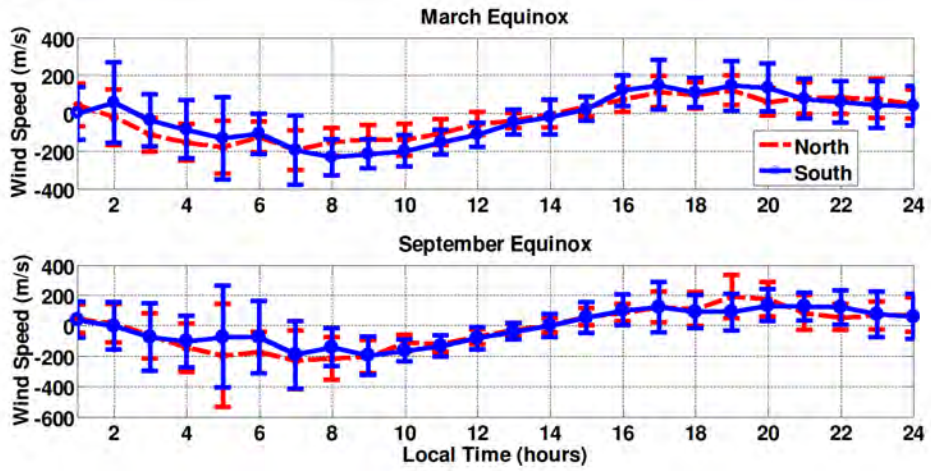

Figure 4: Average zonal wind variation during the equinoxes in the Northern (40° -50° N) and Southern (40° -50° S) hemisphere mid–latitudes.

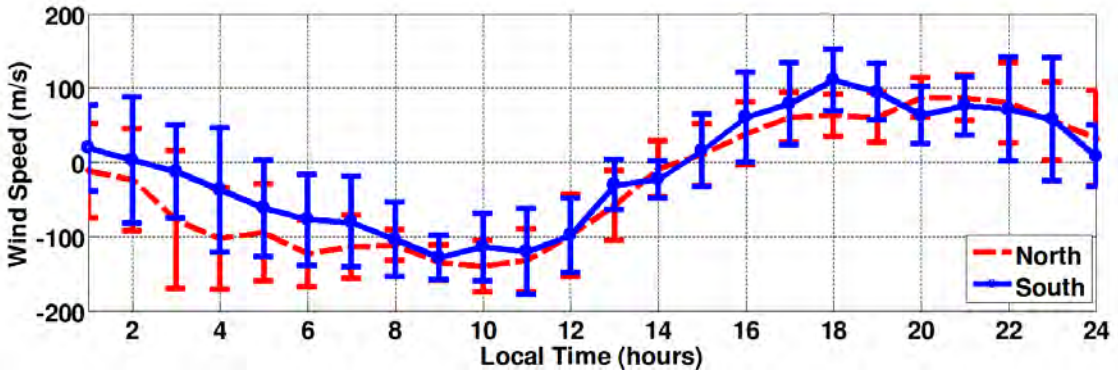

Figure 5: Zonal wind variation from 2002 to 2004 during the high solar flux at low geomagnetic activity levels for combined equinoxes.

transition, the Southern hemisphere winds show enhanced eastward speeds from 1500–2100 LT.

The September equinox winds reveal enhanced westward speeds for the Northern hemisphere winds from about 0300–0900 LT. Maximum westward speeds for Northern hemisphere winds, up to 200 m/s, are observed from about 0630–0900 LT.

comparison with averaged zonal winds for combined equinoxes, from 2002–2004 at high solar flux and low geomagnetic activity level (Figure 5), shows a similar wind pattern with a switch from westward to eastward at about 1430 LT.

3.3. Solstice seasons

Figure 6 displays the diurnal wind variation for June and December solstices. The Northern hemisphere eastward switch in wind direction during the June solstice occurs at 1400 LT while that for the Southern hemisphere is observed earlier, at 1300 LT. Enhanced eastward speeds are

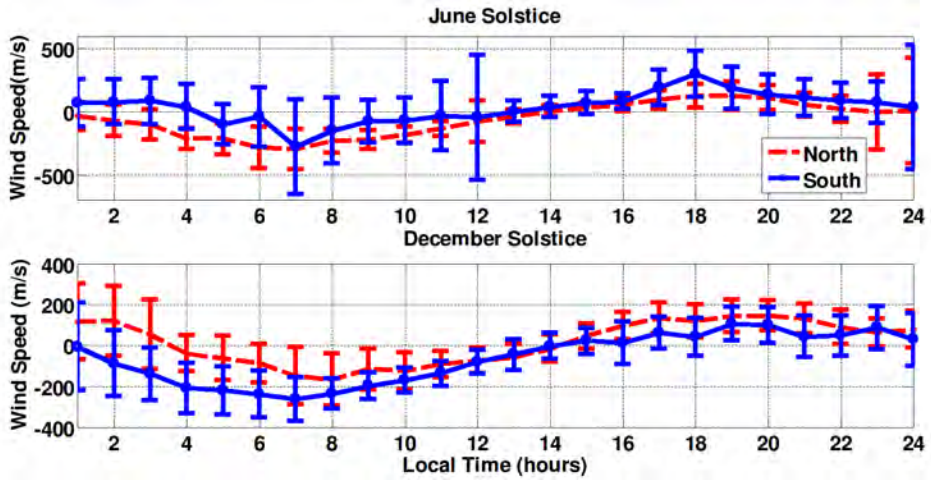

Figure 6: Same as Figure 4, but for solstices.

observed for Southern hemisphere from this time, which switch to midnight when Northern hemisphere winds switch westwards. The westward transition for Southern hemisphere is observed at about 0430 LT. Enhanced westward speeds are observed for Northern hemisphere winds from morning hours till time of eastward switch. For the Southern hemisphere winds, a maximum eastward speed going up to 300 m/s is observed at 1800 LT. During the December solstice, eastward transition is observed in both hemispheres at 1400 LT. The westward switch occurs in the Southern and Northern hemisphere winds at about 0100 LT and 0330 LT respectively.

4. Discussion and conclusion

The period of study, year 2005 to 2008, falls within the declining phase of the recent solar cycle which marks one of the lowest EUV production. In the process of applying the selection criteria for magnetic activity within this period, some bins were left with small number of measurements, especially, during the equinoxes. The mean wind values in some of these cases may not represent typical observed values. The 0800 LT and 2000 LT for September equinox mean wind values may be extreme as enough measurements were not used in averaging. The error bars in Figures 3 to 6 which correspond to the standard deviation indicate the scattering of zonal wind speed in each corresponding magnetic local time bin.

Very quiet geomagnetic conditions correspond to a ground state of the thermosphere with relatively low atomic oxygen concentration at the middle and sub–auroral latitudes (Mikhailov et al., 2007). The solar EUV radiation directly heats the mid–latitude upper thermosphere in the Northern hemisphere during the June solstice and Southern hemisphere mid–latitude during December solstice. The zonal velocities, especially, during the solstices are observed to be large after dawn. Sunrise and sunset are processes which do not occur gradually. Sun–rise in particular is an abrupt event that is followed by rapid increases in electron temperatures and densities and its onset could, thus, give rise to short–lived gravity waves (Emery, 1977). The magnitudes of the dawn and after dawn winds are different in each of the mid–latitude hemisphere during the

solstices. During the June solstice, when the sun is in the Northern hemisphere, the magnitude of mid–latitude wind at and after dawn is more than that of the Southern mid–latitude. The situation in each case is likely due to the overhead sun which initiates large zonal pressure gradients. These pressure gradients, in turn, drive large westward zonal winds at dawn.

Our results compare favourably with model results of Lei et al. (2003) at 300km over Wuhan (30.6°N, 114.4°E). Furthermore, our results generally agree with the HWM–90 (Horizontal wind model–90) predictions of Hedin et al. (1991). The HWM winds in the Southern hemisphere during summer is westward for most of the diurnal variation and eastward winds are only encountered within a short interval from about 1600–2000 LT. In the Northern hemisphere, summer wind direction is western for all day with a small eastward switch from about 1800 to 2200 LT. The eastward switches during equinoxes occur at about 1500 LT just like the CHAMP measurements. The change in wind direction for December solstice model winds is at about 1300 LT, while for CHAMP this change is observed at about 1500 LT. In all cases, nonetheless the CHAMP winds and HWM winds generally blow westward for most of the day and eastward for most of the night. The temporal discrepancies observed in the model predictions and CHAMP winds can be attributed to number of factors ranging from the data used, prevailing conditions and the difference in latitude bands.

Emery (1977) deduced the quiet–time thermospheric circulation pattern above the Millstone Hill (42.6°N, 71.5°W) with an incoherent scatter radar facility, for the years of 1970 and 1971, using measured values of ionospheric drift, temperatures and densities. The deduced zonal winds were eastwards at dusk and westwards at dawn.

In addition, our studies revealed a shift in direction from westward to eastward at 1500 LT for all the seasons. June solstice winds were significantly more westwards during the morning hours in the Northern hemisphere mid–latitude than the Southern hemisphere mid–latitude. December solstice winds are more westwards from about mid–night to morning hours in the Southern hemisphere mid–latitude. There is a hope for improvement, as 24 hour ground observations of thermospheric winds have been reported by Gerrard and Meriwether (2011), using newly developed Second–generation Optimized Fabry–Perot interferometer (SOFDI).

Acknowledgements. The authors thank Doornbos E. for making his data available for this study. We do also appreciate his advice concerning the datasets. The authors are also grateful for the availability of the geophysical parameters in OMNI database (http://omniweb.gsfc.nasa.gov.). Research is supported by South African National Space Agency (SANSA).

References

Aruliah, A., Griffin, E.M., McWhirter, I., Aylward, A.D., Ford, E.A.K., Charalambous, A., Kosch, M.J., Davis, C.J., Howells, V.S.C., 2004. First tristatic studies of meso-scale ion-neutral dynamics and energetics in the high-latitude upper atmosphere using collocated FPIs and EISCAT radar. Geophysical Research Letters 31, L03802.

Balan, N., Kawamura, S., Nakamura, T., Yamamoto, M., Fukao, S., Igarashi, K., Maruyama, T., Shiokawa, K., Otsuka, Y., Ogawa, T., Alleyne, H., Watanabe, S., Murayama, Y., 2004.

Simultaneous mesosphere/lower thermosphere and thermospheric F region observations during geomagnetic storms. Journal of Geophysical Research 109, A04308.

Bounsanto, M.J., 1991. Neutral in the thermosphere at mid latitudes over a full solar cycle: A tidal decomposition. Journal of Geophysical Research 96, 3711–3724.

Bruinsma, S., Forbes, J., 2010. Anomalous behavior of the thermosphere during solar minimum observed by CHAMP and GRACE. Journal of Geophysical Research 115, A11323.

Burns, A.G., Killeen, T.L., Deng, W., Carignan, G.R., Roble, R., 1995. Geomagnetic storm effects in the low- to mid-latitude upper thermosphere. Journal of Geophysical Research 100, 14673–14692.

Doornbos, E., Van den Ijssel, J., H., L., Forster, M., Koppenwallner, G., 2010. Neutral density and crosswind determination from arbitrarily oriented multi-axis accelerometers on satellites. Journal of Spacecraft and Rockets 47, 580–589.

Duboin, M.L., Lafeuille, M., 1992. Thermospheric dynamics above saint-Santin: statistical study of the data set. Journal of Geophysical Research 97, 8661–8671.

Emery, B.A., 1977. Seasonal wind variations in the mid- latitude thermosphere. Ph.D. thesis.

Emery, B.A., Lathuillere, C., Richards, P.G., Roble, R.G., Bounsanto, M.J., Knipp, D.J., Wilkinson, P., Sipler, D.P., Niciejewski, R., 1999. Time dependent thermospheric neutral response to the 2-11 November 1993 storm period. Journal of Atmospheric and Solar-Terrestrial Physics 61, 329–350.

Fejer, B.G., Emmert, J.T., Sipler, D.P., 2002. Climatology and storm time dependence of nighttime thermospheric neutral winds over Millstone Hill. Journal of Geophysical Research 107, 1052.

Fesen, C.G., Roble, R.G., Duboin, M.L., 1995. Simulations of seasonal and geomagnetic activity effects at Saint-Satin. Journal of Geophysical Research 100, 21397–21407.

Fuller-Rowell, T.J., Codrescu, M.V., Moffet, R.J., Quegan, S., 1994. Rsponse of thermosphere and ionosphere to geomagnetic storms . Journal of Geophysical Research 99, 3893–3914.

Fuller-Rowell, T.J., Codrescu, M.V., Rishbeth, H., Moffet, R.J., Quegan, S., 1996. On the seasonal response of the ionosphere and thermosphere to geomagnetic storms. Journal of Geophysical Research 101, 2343–2353.

Gerrard, A.J., Meriwether, J.W., 2011. Initial daytime and nighttime SOFDI observations of thermospheric winds from Fabry-Perot Doppler shift measurements of the 630-nm oI line-shape profile. Annales Geophysicae 29, 1529–1536.

Hedin, A.E., Biondi, M.A., Burnside, R.G., Hernandez, G., Johnson, R.M., 1991. Revised global model of thermospheric winds using satellite and ground –based observations. Journal of Geophysical Research 96, 7657–7688.

Kawamura, S., Otsuka, Y., Zhang, S.R., Fukao, S., Oliver, W.L., 2000. A climatology of middle and upper atmosphere radar observations of thermospheric winds. Journal of Geophysical Research 105, 12777–12788.

Kazimirovsky, E.S., Kokourov, V.D., Vergasova, G., 2006. Dynamical climatology of the upper mesosphere, lower thermosphere and ionosphere. Surveys in Geophysics 27, 211–255.

Larsen, M., Fesen, C., 2009. Accuracy issues of the existing thermospheric wind models: can we rely on them in seeking solutions to the wind driven-driven problems? Annales Geophysicae 27, 2277–2284.

Lei, J., Liu, L., Luan, X., Wan, W., 2003. Model study on neutral winds in the ionospheric F-region and comparison with the equivalent winds derived from the Wuhan ionosonde data. Terrestria, Atmospheric and Oceanic Sciences 14, 1–12.

Liu, H., Lühr, H., Watanabe, S., Kohler, W., Henize, V., Visser, P., 2006. Zonal Winds in the equatorial upper atmosphere. Journal of Geophysical Research 3, A07307.

Lühr, H., Rentz, S., Ritter, P., Liu, H., Haüsler, K., 2007. Average thermospheric wind patterns over the Polar Regions, as observed by CHAMP . Annales Geophysicae 25, 1093–1101.

Mikhailov, A.V., Depuev, V.H., Depueva, A.H., 2007. Synchronous NmF2 and NmE daytime variations as a key to the mechanism of quiet-time F2-layer disturbances. Annales Geophysicae 25, 483–493.

Moussas, X., Polygiannakis, J., Preka-Papadema, P., Exarhos, G., 2005. Solar cycles: A tutorial. Advances in Space Research 35, 725–738.

Nozawa, S., Brekke, A., 1995. Studies of the E-region neutral wind in the disturbed auroral ionosphere. Journal of Geophysical Research 100, 14717–14734.

Rees, D., 1995. Observations and modeling of ionsopheric and thermospheric disturbances during major geomagnetic storms: A review. Journal of Atmospheric and Terrestrial Physics 57, 1433–1457.

Reigber, C., Bock, R., Förste, C., Grunwaldt, L., Jakowski, N., Lühr, H., Schwintzer, P., Tilgner, C., 1996. CHAMP phase B executive summary. Technical Report.

Ritter, P., Lühr, H., Doornbos, E., 2010. Substorm related thermospheric density and wind disturbances derived from CHAMP observations . Annales Geophysicae 28, 1207–1220.

Walker, J., 1988. The mid-latitude thermosphere . Planet Space Science 36, 1–10.

Chapter 7

Concluding remark and future perspective

The response of Mesosphere and Lower Thermosphere (MLT) temperature to energetic particle precipitation over the Earth's polar regions is not uniform, due to complex phenomena within the MLT environment. Nevertheless, the modification of MLT temperatures may require an event–based study, in order to be better observed.

In this study, model calculations, ground–based and satelliteborne measurements were employed in a case study and statistical studies. The MC event case study in Chapter 3 suggests a potential cooling effect, an apparent heating effect, or no significant temperature response to MC–triggered precipitation over SANAE IV in the Southern hemisphere and at its conjugate vicinity in the Northern hemisphere. These apparent contradictory mesospheric temperature responses, demonstrate the interhemispheric complexity of the energy budget in the MLT–region. This motivated another study in Chapter 4 that looks at a plausible temperature response to SI–triggered precipitation, statistically, as a large set of data may average out the influence from some of the other energy budget parameters, such as gravity waves and tides.

The SEA approach presented in Chapter 4, showed a possible heating in the upper mesosphere ($\sim$100 km), when considering the possibility that a potential temperature response could become significant and measurable when it accumulates over time. This is not the same for the lower mesosphere (below 95 km), wherein, direct particle impact initiated cooling in

response to the SI event. Similar results were also obtained for the SI case study. With these results, it was obvious that there is need to study another Geospace event based on layer phenomena (such as PMSE) and geomagnetic activity. The SuperDARN–PMSE event described in Chapter 5, was considered and examined in relation to atmospheric features, particularly, temperature. The SuperDARN–PMSE peaks coincide with lower summer mesopause temperature and higher geomagnetic activity. The dependency of SuperDARN–PMSE occurrence on the lowering of summer mesopause temperature and equatorward winds, partly, indicates the importance of pole to pole mesospheric transport circulations in the MLT energy budget over SANAE IV.

These results encourage a future study, whereby, one could add a memory to the areas of an event triggered precipitation for evaluating a potential time–dependent MLT temperature response. In addition, a future study on variation of neutral parameters, such as neutral winds is motivated. In doing this, a reference quite–time approach would be useful, such that the observables during quiet conditions can be compared with periods of high solar activity. For instance, the diurnal variations of upper thermosphere zonal winds during the recent prolonged low solar activity may elucidate on MLT energy balance. These efforts can also be directed towards achieving a more self–consistent interpretation of how the MLT is influenced by magnetospheric processes. A good starting point is, an in–depth understanding of the thermospheric winds in mid–latitudes (see Chapter 6). Asymmetry in diurnal thermospheric zonal wind variations is evident during the equinox periods in both Southern and Northern hemispheres mid–latitudes. The differences observed in the morning winds at the conjugate mid–latitude bands during the solstices may be attributed to the solar irradiation. However, the thermospheric zonal winds in this study are longitudinally averaged and results may thus differ from single station measurements. There is hope for improvement, as 24 hour ground observations of thermospheric winds at different locations (using newly developed Second–generation Optimized Fabry–Perot interferometer (SOFDI)), can be compared with satellite observations.

Appendices

Appendix A

Dipole coordinate system

The Earth's magnetic field can be estimated by a dipole field components from high to the lowest order:

$$B_r = -2\frac{B_o}{r^3}\sin\lambda \tag{A.1}$$

$$B_\lambda = \frac{B_o}{r^3}\cos\lambda \tag{A.2}$$

with the magnitude expressed as:

$$B = \frac{B_0}{r^3}\sqrt{1+3\sin^2\lambda} \tag{A.3}$$

In this cases, r is the geocentric interspace in units of 1 R_E, and B_o in unit of nT is taken as equatorial field strength at the surface of the Earth. The general assumption is that the dipole's originated from the Earth's center point. The IGRF assimilate higher order modifications in the dipole field and offers an exact representation of the Earth's inherent field. The IGRF modification can be assumed as an eccentric dipole model which entails an offset in the position of the dipole's origin.

A magnetic field curves tangential to B can be expressed as:

$$\frac{dr}{rd\lambda} = \frac{B_r}{B_\lambda}, \tag{A.4}$$

truncating this will result to:

$$r = L\cos^2\lambda, \tag{A.5}$$

where the constant of integration L serves to label a magnetic shell. In this case, the invariant latitude of a magnetic field is given as

$$\Lambda = \arccos(\frac{1}{\sqrt{L}}), \tag{A.6}$$

and proportional to the latitude at which it traverses the surface of the Earth.

The expanse of a dipole field line in R_E unit is:

$$l(L) = \int_{-\Lambda}^{+\Lambda} L\cos\lambda\sqrt{1+3\sin^2\lambda d\lambda} \tag{A.7}$$

truncating this length of dipole field line yields:

$$l(L) = \sqrt{L-1}\sqrt{4L-3} + \frac{L}{\sqrt{3}}\arcsin h\sqrt{3(1-1/L)} \tag{A.8}$$

Appendix B

First order correction techniques

The NOAA/POES MEPED instruments are expected to measure electron flux and proton flux separately with the two different detectors. Nevertheless, various simulations and visualisation shows that the NOAA/POES electrons (>30 keV, >100 keV, and >300 keV) measurements are respectively impaired by protons of 210–2700 keV, 280–2700 keVs, and 440–2700 keV. The MEPED proton channels (p2, p3 and p4) sample only protons with energies ranging from 80–240 keV, 240–800 keV, 800–2500 keV, respectively. Regrettably, the channels can not absolutely bracket the range of contaminating protons. Thus, the correction requires more task than just subtraction. For instance, an electron with energy >30 keV is impaired by more than 210 keV proton energy while the p2 channel starts measuring from 80 keV proton energy. Similarly, only few fragments of the p3 energy will contribute to the electron contamination in the >100 and >300 keV energy channels. So, energy spectral can be assumed since it is not known.

Assuming that the proton energy spectrum takes the form of piecewise series exponential functions, the total counts within a single band can be defined as:

$$C = \int_{E1}^{E2} J(E, \Omega, A, t) dE d\Omega dA dt \tag{B.1}$$

here the particle energy is E, Ω represents solid angle, the detector area of the silicon is A, t is taken as time, the differential flux $J(E, \Omega, A, t)$ is in unit of $cm^{-2}s^{-1}sr^{-1}keV^{-1}$

and at the interval of integration, C is taken as number of counts measured detected by the telescopes.

It can also be assumed that the impinging flux neither differs with the angle of incidence nor time so that one can have:

$$C = G \int_{E1}^{E2} J(E) dE \tag{B.2}$$

where the MEPED geometric factor G is taking as .01 $cm^{-2}s^{-1}sr^{-1}$.

Again, assuming an exponential flux decrease with energy then:

$$C = G \int_{E1}^{E2} J_0(E) \exp(-E/E_0) dE \tag{B.3}$$

The approximate area of the rectangle with the height $J(E)$ as well as width ΔE can be obtained as:

$$C = G \int_{E1}^{E2} J_0(E) \exp(-E/E_0) dE = G J_0 \exp \frac{-\tilde{E}}{E_0} \Delta E = G J \tilde{E} \Delta E \tag{B.4}$$

By employing the approximation in B.4, the counts within the instrument energy channels can be converted to differential flux using:

$$J(\tilde{E}) = \frac{C}{G \Delta E} \tag{B.5}$$

So that the quantities $\tilde{E}$ and ΔE can be linked by:

$$\Delta E = \exp(\frac{\tilde{E}}{E_0}) \int_{E1}^{E2} \exp(\frac{-E}{E_0}) dE \tag{B.6}$$

Appendix C

Monte Carlo calculation of electron trajectory

Referable to equation of motion at collision, electron transfers during free flights can be estimated. Assuming there is motion of electrons in the magnetic field B, the motion can be expressed as:

$$\frac{d^2x}{dt^2} = \omega\frac{d^2y}{dt}, \frac{d^2y}{dt^2} = -\omega\frac{dx}{dt}, \frac{d^2z}{dt^2} = 0, \tag{C.1}$$

where ω is the gyrofrequency expressed as:

$$\omega = \frac{eB}{mc}\sqrt{1 - \frac{v^2}{c^2}}. \tag{C.2}$$

Starting with the initial time of the free flight ($t = 0$), the electron velocity, v will be:

$$\frac{dx}{dt} = vsin\theta cos\phi, \frac{dy}{dt} = vsin\theta sin\phi, \frac{dz}{dt} = vcos\theta. \tag{C.3}$$

By truncating equations in Equation C.1, it becomes:

$$x(t) = x_B + \frac{v}{\omega}sin\theta sin(\omega t - \phi)y(t) = y_B + \frac{v}{\omega}sin\theta cos(\omega t - \phi)z(t) = z(0) + vtcos\theta, \tag{C.4}$$

where x_B and y_B represent the magnetic field line coordinates where the electrons are believed

to spiral:

$$x_B = x(0) + \frac{v}{\omega} sin\theta sin\phi y_B = y(0) + \frac{v}{\omega} sin\theta cos\phi. \tag{C.5}$$

Also, the distance between collisions is obtained. Here, all the electron characteristics preceding the $n'th$ collision is indicated by the subscript n. The tendency for $n+1'st$ collision to happen is denoted by E_{n+1} and $E_{n+1} + dE$ which is expressed as:

$$\exp(-\int_{E_{n+1}}^{E_n} \frac{\mu(E')}{L(E')} dE) \frac{\mu(E_{n+1})}{L(E_{n+1})} dE, \tag{C.6}$$

where μ is the scattering coefficient and obtained as:

$$\mu(E) = \frac{\pi N_a \exp 4}{\rho^2 v^2} \sum_i \omega_i \frac{Z_i(Z_i+1)}{A_i} \frac{1}{\eta i(\eta i+1)}, \tag{C.7}$$

where Z is the nuclear charge, the effect of screening in terms of η parameter is formulated as:

$$\eta = \eta_c \frac{1.70 \times 10^{-5} Z^{2/3}}{\tau(\tau+2)}, \tag{C.8}$$

here kinetic energy τ is in units of the electron rest mass, and $\eta_c = 1.13 + 3.76[\frac{Z}{137(v/c)}]^2$; the average electron energy loss per unit pathlength is $L(E)$ given as:

$$L(E) = \frac{0.1536}{\beta^2} (\Sigma_i W_i \frac{Z_i}{A_i}) log[\frac{\tau(\tau+2)}{2(I/mc^2)^2}] + 1 - \beta^2 + [\tau^2/8 - (2\tau+1)log2]/(\tau+1)^2, \tag{C.9}$$

where E as earlier noted is the electron energy; mc^2 as rest mass; c and v are the velocities of light and electron respectively; Ai and wi are the atomic weight and the fraction by medium weight of the ith constituent respectively; the average excitation in the required energy medium is I; also the N_a is Avogadro's number and can be taken as:

$$\frac{\pi N_a \exp 4}{\rho^2 v^2} = 0.150[\frac{\tau+1}{\tau(\tau+2)}]^2. \tag{C.10}$$

In this case, the mean free path length lm can be obtained as: $lm = 1/\mu(E)$. Therefore, the

average number of collisions taking this path, q can be evaluated using continuous–slowing–down approximation hence:

$$q = \int_{E_{n+1}}^{E_n} \frac{\mu(E)}{L(E)} dE \tag{C.11}$$

which has a function e^q. Sampling the value of E_{n+t} will require an exponential distribution:

$$q = -log\zeta, \tag{C.12}$$

where ζ is the evenly distributed (between 0 and 1) random number. Knowing this, one can solve for E_{n+1} as a function of E_n and q. Using interpolation techniques this can be achieved (see Chapter 3 of this thesis).

Therefore, in the computation of the energy deposited, about $(E0 - Ec)/E0$ can be properly terminated using the Green–Peterson formula which is given as:

$$L(E) = 1440 \frac{Z^*}{A} [\Sigma_j (\frac{E}{c_j})^{d_j}]^{-1}, \tag{C.13}$$

where Z^* is the effective number of atoms, the parameters (numerical) $c_j's$ and $d_j's$ are with values for N_2 and O_2 and can be obtained from MSIS-E-90 model.

During the computation, the energy deposition at different altitudes for each of the electron trajectory was taken:

$$s_{mb} = \frac{z_m(h_b) - z_{m.n}}{Cos\theta_n}; \tag{C.14}$$

where,

$$z_m(h_b) = \int_h^{h_o} D(h_b')dh'$$

is taken as the atmospheric depth with $D(h_b')$ taken as the density, the electrons are made to pass through the scoring boundary h_b within the collisions from $n'th$ to $n + 1'$ st, and $Z_m(h_b)$ is the thickness of the mass at various heights. The interspace, s_m, advanced by the electrons within the boundary b is expressed as:

$$s_m = \int_{E_{n+1}}^{E_n} \frac{dE}{L(E)} = r_o(E_n) - r_o(E_{n+1)} \tag{C.15}$$

This can be obtained by using interpolation (see Chapter 3) of the atmospheric mean range, r_o relative to observed electron energy E, with stopping power L within the $n'th$ point of collision to the required boundary being s_{mb}.